Three-Dimensional Configuration and Evolution of Coronal Mass Ejections

Von der Fakultät für Physik und Geowissenschaften

der Technischen Universität Carolo-Wilhelmina

zu Braunschweig

zur Erlangung des Grades einer

Doktorin der Naturwissenschaften

(Dr.rer.nat.)

genehmigte

D i s s e r t a t i o n

von María Hebe Cremades Fernández

aus Mendoza / Argentinien

Bibliografische Information Der Deutschen Bibliothek
Die Deutsche Bibliothek verzeichnet diese Publikation in der Deutschen Nationalbibliografie; detaillierte bibliografische Daten sind im Internet über http://dnb.ddb.de abrufbar.

1. Referentin oder Referent: Prof. Dr. Karl-Heinz Glaßmeier
2. Referentin oder Referent: Prof. Dr. Rainer Schwenn
eingereicht am: 24.02.2005
mündliche Prüfung (Disputation) am: 10.05.2005

ISBN 3-936586-40-3

Copernicus GmbH, Katlenburg-Lindau
Druck: Schaltungdienst Lange, Berlin

Printed in Germany

Vorveröffentlichungen der Dissertation

Teilergebnisse aus dieser Arbeit wurden mit Genehmigung der Gemeinsamen Naturwissenschaftlichen Fakultät, vertreten durch die Mentorin oder den Mentor/die Betreuerin oder den Betreuer der Arbeit, in folgenden Beiträgen vorab veröffentlicht:

Publikationen

Cremades, H. and Bothmer, V., On the Three-Dimensional Configuration of Coronal Mass Ejections, A&A, 422, 307-322, 2004.

Tripathi, D., Bothmer, V., and Cremades, H., The Basic Characteristics of EUV Post-Eruptive Arcades and their Role as Tracers of Coronal Mass Ejection Source Regions, A&A, 422, 337-349, 2004.

Cremades, H. and Bothmer, V., Geometrical Properties of Coronal Mass Ejections, in Proc. IAU Symp. 226 on Coronal and Stellar Mass Ejections, eds. Dere, K. P., Wang, J., and Yan, Y., 48-54, 2005.

Gopalswamy, N. et al., The pre-CME Sun, Report of Working Group E, in Space Science Series of ISSI, in press.

Cremades, H., Bothmer, V., and Tripathi, D., Properties of Structured Coronal Mass Ejections in Solar Cycle 23, Adv. Space Res., in press.

Tagungsbeiträge

Cremades, H., V. Bothmer, and D. Tripathi: 3D Magnetic Field Configuration & Evolution of CMEs (Oral). Seminar at the Astrophysics and Space Sciences Section, JPL, Pasadena, CA, USA, 12 March 2003.

Cremades, H., V. Bothmer, D. Tripathi, and K. -H. Glassmeier: 3D Magnetic Field Configuration & Evolution of CMEs (Oral). EGS-AGU-EUG Joint Assembly, Nice, France, 7-11 April 2003.

Cremades, H., V. Bothmer, and K. -H. Glassmeier: 3D Magnetic Field Configuration & Evolution of CMEs (Oral). Seminar of the Institut für Geophysik und Meteorologie, TU Braunschweig, 28 October 2003.

Cremades, H., V. Bothmer, and D. Tripathi: On the Three-Dimensional Configuration of Coronal Mass Ejections (Poster). 1st EGU General Assembly, Nice, France, 25-30 April 2004.

Cremades, H., V. Bothmer, and D. Tripathi: Properties of Structured Coronal Mass Ejections in Solar Cycle 23 (Oral). 35th COSPAR Scientific Assembly, Paris, France, 18-25 July 2004.

Cremades, H., V. Bothmer, and D. Tripathi: Geometric Properties of Coronal Mass Ejections (Oral). IAU Symposium 226 on Stellar and Coronal Mass Ejections, Beijing, China, 13-17 September 2004.

Who loves the Sun,
Who cares that it makes plants grow,
Who cares that it is shining?
Who cares what it does, since you broke my heart?

The Velvet Underground

To my family

Abstract

Coronal mass ejections (CMEs) are a direct consequence of the dynamic nature of the Sun. They represent fundamental powerful processes in which energy is transferred from the Sun into interplanetary space, including geospace. Their origin, three-dimensional structure, and internal magnetic field configuration are to date not well understood. The unprecedented data provided by the Solar and Heliospheric Observatory (SOHO) allow for the first time the resolution of fine structures within CMEs, which can help to deduce their three-dimensional configuration.

From a detailed investigation of the full set of SOHO/LASCO (Large Angle Spectroscopic Coronagraph) observations from 1996 to the end of 2002, a set of "structured CMEs" has been identified, i.e. events which exhibit white-light fine structures, likely indicative of their internal magnetic field configuration and possible 3D structure. Their source regions in the low corona and photosphere have been inferred by means of complementary analyses of data from the EUV Imaging Telescope (EIT) and Michelson Doppler Imager (MDI) onboard SOHO, and ground-based Hα measurements. From the characteristic pattern of the CMEs' source regions in both solar hemispheres, a generic scheme of three-dimensional configurations is deduced. According to the scheme, the projected white-light topology of a CME depends primarily on the heliographic position and orientation of the source region's underlying neutral line that separates opposite magnetic polarities. The cylindrical geometry found in the structured CMEs implies that they are organized along an axial direction.

Furthermore, the typical dimensions of structured events exhibiting extreme projections (viewed along their axis or perpendicular to it) were investigated. These events originated from limb and near-limb regions. The measured dimensions indicate that these CMEs would be better approximated by elliptic cones, rather than by the classical cone of circular cross section. The dimensions of halo CMEs originating near Sun center are expected to agree with those obtained for the structured events. In order to understand the CME topology better, an elliptical cone model was developed as an improvement to an existing circular cone model, in an effort to fit and reproduce a set of halo CMEs from LASCO.

Contents

List of Figures

List of Tables

Introduction

The solar corona is the outermost component of the solar atmosphere. It is a highly rarefied ionized gas with extremely low densities, less than one billionth of the Earth's atmosphere. Its luminous intensity is 100 million times less than that of the photosphere. The dim corona is only observable by blocking the photospheric light, in the way that the Moon does during total eclipses of the Sun. But such events occur only every couple of years, often in remote places, and they last only for a few minutes, impeding a systematic observation of the solar atmosphere. It was the French astronomer Bernard Lyot who was able for the first time to produce an "artificial" solar eclipse, via an instrument called "coronagraph" (Lyot 1939). A coronagraph captures the photospheric light scattered by free electrons and dust particles in the Sun's corona. Since the spatial distribution of coronal electrons is shaped by coronal magnetic fields, coronagraph observations display the configuration of the magnetic field structures. Although it might have seemed obvious from the first observations that the corona is static or only slowly changing, indeed we know today that it is highly dynamic. The discovery of coronal transients dates back to the early 1970's, much later than the first sighting of a solar flare in 1859 by R. Carrington. It was possible only when coronagraphs were put in space, thus avoiding the brightness of the daylight sky. These transients are characterized by the appearance of discrete white light features in the field of view of the coronagraph, and can be followed by their outward motion across the coronagraph's field of view (see Figure I.1). It was not until 1984 that such transients were scientifically defined and termed Coronal Mass Ejections (CMEs; Hundhausen et al. 1984).

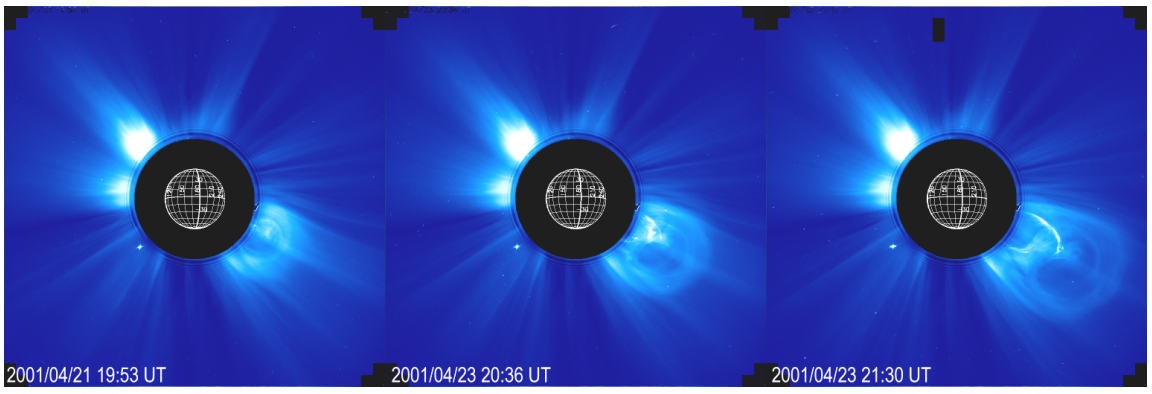

Figure I.1. Three snapshots of a coronal transient, commonly referred to as a Coronal Mass Ejection (CME). Located in the SW quadrant (solar north is up), the transient was captured by the LASCO/C2 coronagraph on board the SOHO spacecraft on April 23, 2001.

Knowledge concerning CMEs is derived mainly from coronagraph observations made from space: the coronagraphs onboard the Seventh Orbiting Solar Observatory (OSO 7; Tousey & Koomen 1974) and Skylab (e.g., Gosling et al. 1974; *http://www.hao.ucar.edu/public/-research/mlso/Skylab/skylab_homepage.html*). After these, white-light coronal data were

retrieved by the Solwind coronagraph on the P78-1 spacecraft during 1979-1985 (Sheeley et al. 1980; *http://lasco-www.nrl.navy.mil/solwind.html*) and by the Coronagraph/Polarimeter aboard the Solar Maximum Mission during 1980 and 1984-1989 (SMM; MacQueen et al. 1980; *http://www.hao.ucar.edu/public/research/svosa/smm/smmcp_cme.html*). At the present time and since 1996, unprecedented images of CMEs are provided by the Large Angle Spectroscopic COronagraphs (LASCO; Brueckner et al. 1995; *http://star.mpae.gwdg.de/*) on the Solar and Heliospheric Observatory (SOHO; Fleck et al. 1995; *http://sohowww.nascom.nasa.gov/*). Additional coronagraphic images are provided by the ground-based Mark-IV K-coronameter (Mk4; *http://mlso.hao.ucar.edu/mk4.html*) at the Mauna Loa Solar Observatory in Hawaii and by the Mirror Coronagraph for Argentina (MICA; Stenborg et al. 1999; *http://star.mpae.gwdg.de-/mica/mica_home.htm*). However, ground-based observations of the dim corona are limited, mainly because of the sky's brightness during daytime and the varying radiation transmission of the Earth's atmosphere.

CMEs carry billions of tons of gas into interplanetary space, as well as magnetic fields which can interact with the Earth's outer magnetic field (and that of other solar system objects). In general, when CME speeds considerably exceed that of the solar wind, they drive interplanetary shock waves which in turn may accelerate energetic particles up to MeV energies (e.g., Bothmer 1999). The apparent angular spans of CMEs encompass values from just a few degrees up to 360°. In the latter case the occulter of the coronagraph is completely surrounded by the CME (see Figure I.2), which under these circumstances is termed halo CME (Howard et al. 1982).

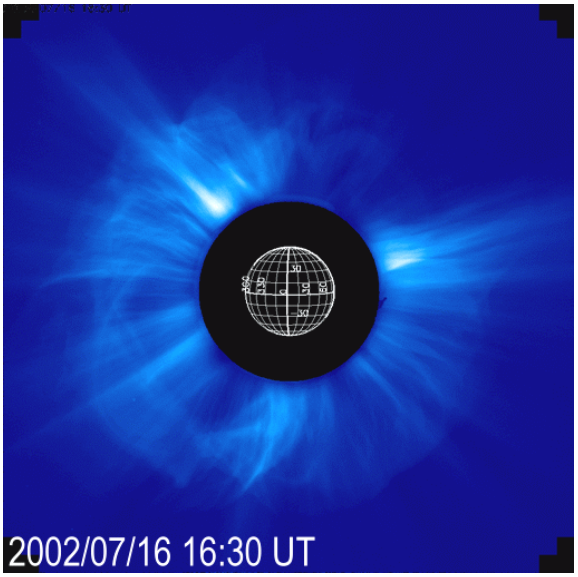

Figure I.2. The halo CME on July 16, 2002, as observed by the LASCO/C2 coronagraph.

In spite of the technological achievements accomplished in the past few decades, the information on CMEs provided by a coronagraph is constrained to a particular view projected onto the plane of the sky. The reason for this constrain is that the brightness measured by a coronagraph is essentially proportional to the density of electrons integrated along the line of sight, determined by the three-dimensional structure of the imaged coronal features. The two-dimensional nature of coronagraphic images, as well as the current restriction to observations from a single viewpoint limit our present knowledge about the three-dimensional configuration and geometry of CMEs. From the astrophysics point of view, the comprehension of the phenomena and their related processes that take place at the Sun can be applied to other stars with similar characteristics. It is well established that CMEs produce on Earth not just stunning aurorae but also threatening

effects, as for instance telecommunication and satellite damages (e.g., Tsurutani et al. 2005). Moreover, highly energetic particles produced at the shocks driven by fast CMEs may affect electronic equipment and life forms situated outside the shielding magnetosphere (e.g., Reitz 1999; Dyer 2002). Hence, from a practical point of view, it is crucial to understand which CMEs may reach the Earth, and what will be the space weather consequences based on their physical properties.

The problem of the CMEs' three-dimensional configuration has been addressed ever since the discovery of CMEs (see e.g., review by Schwenn 1986). One of the very first attempts to infer the three-dimensional configuration of CMEs was that of Trottet & MacQueen (1980), based on the close association found between CMEs and eruptive prominences/disappearing filaments (Munro et al. 1979). Their study suggested that Skylab CMEs were essentially planar loops. On the contrary, Crifo et al. (1983) concluded that polarization measurements indicated a three-dimensional, bubble-shaped structure rather than a loop. Following the same line of study, Fisher & Munro (1984) developed a three-dimensional model of polarized brightness and compared it successfully to a CME observed by the Mk III K-coronameter. Webb (1988) carried out a similar research to that of Trottet & MacQueen (1980), but in this occasion with SMM CMEs. He found no systematic filament orientations for loop-like CMEs and concluded that CMEs are indeed three-dimensional entities. MacQueen (1993) provided subsequent evidence on the three-dimensional nature of loop-like Skylab CMEs, via a model representing the electron density distribution of the coronal structure.

To date, the three-dimensional structure of CMEs and details on their configuration remain unknown (see references above). This doctoral thesis has been developed in preparation for the NASA STEREO (Solar TErrestrial RElations Observatory; see Appendix) Mission. The study is based on the exceptional data recorded by the high resolution instruments onboard the SOHO Mission. The images constitute a unique dataset, in which for the first time fine structures can be resolved within individual CMEs, enabling a systematic study. The doctoral thesis aims at finding answers to the following questions:

- What is the overall three-dimensional configuration of CMEs? Do they resemble a bubble-like shape with symmetry of rotation, or an arcade of loops?
- How are the source regions of CMEs characterized? Is it possible to trace them back from coronagraph observations into the low corona and photospheric regimes? Which is their connection with neutral lines?
- What is the relationship between CME features observed in white light and solar surface structures viewed in various wavelengths? Which are the determining factors for the dimensions and proportions of CMEs? Is the magnetic configuration of the subsequent CMEs related to the underlying photospheric structures prior to the eruption, such that space weather forecasting would be facilitated?
- How do CMEs evolve in the near-Sun low corona? What does this information reveal about the later evolution in the heliosphere? How can their expansion be characterized? What are the physical processes that determine their early evolution?

Basic information on the Sun and fundamentals on the solar corona are introduced in Chapter 1. The instruments and the data provided by SOHO are described in Chapter 2, together with the methods used to analyze the data. In Chapter 3, a set of structured CMEs seen by

SOHO/LASCO, comprised of events which exhibit white-light fine structure, is introduced and analyzed. The question whether this fine structure is indicative of their internal magnetic field configuration and possible 3D structure is addressed in the same chapter. An approach based on the characterization of the associated source regions magnetic field configuration is undertaken, in order to relate it with the projected white light topology of the corresponding CMEs. In this way, a scheme of 3D configuration is deduced, followed by the calculation of typical widths of structured CMEs exhibiting extreme cases of projection. Chapter 4 presents the elliptical cone model that was developed as an improvement to a circular cone model (presented by Zhao et al. 2002), in an effort to test the results obtained for the structured CMEs. Finally, the summary of the main results of this work and future perspectives are presented.

Chapter 1

Sun's essentials – The solar atmosphere

1.1 Introduction

The Sun, our nearest star, is the vigorous source of energy that maintains life on Earth. Its warmth and light are essential for the water cycle and photosynthesis, the most important processes involved in our existence. Ancient cultures such as the Egyptian, Babylonian, Greek, Hindu and native-Americans venerated the Sun as a divinity. Various antique buildings that survived the pass of time demonstrate today not only the Sun's role in religious matters but also that the Sun has always been object of intense study. The amazement experienced during total solar eclipses certainly increased its mystery and fascination. Most of the records of early eclipse observations were found in western Asia, and are believed to date back in time approximately to 700 BC. Records of sunspot observations existed long before the invention of the telescope. The oldest record found was registered in China, in 165 BC.

After failed attempts to obtain the distance to the Sun (including that of Aristarchus, which yielded a value of 19 times the distance to the moon), accuracy in triangulation methods allowed the determination of the actual mean value of 1 astronomical unit (AU) equal to 1.496×10^{11} m. The solar mass, $M_{\odot}=1.989 \times 10^{30}$ kg and the solar radius, $R_{\odot}=6.955 \times 10^{8}$ m are calculated on the basis of the Sun's mean distance. The solar luminosity $L_{\odot}$ is defined as the total electromagnetic radiation (photons) per unit time, and is directly related to the Sun's mean distance and the solar constant. The solar constant is given by the total solar energy over all wavelengths, per unit time and unit area (also termed flux or irradiance) at 1 AU, measured outside the Earth's atmosphere. Its actual value of 1366 Wm^{-2} yields an $L_{\odot}=3.845 \times 10^{26}$ W. This quantity gives the effective temperature of the solar disk, $T_{eff_{\odot}}=5780$ K, when introduced in Stefan-Boltzmann's law:

$$L_{\Theta} = 4 \cdot p \cdot s \cdot R_{\Theta}^{\ 2} \cdot T_{eff\,\Theta}^{\ 4}$$

Since the Sun formed around 4.6 billion years ago, it has been in constant evolution. At the present time it is a middle-aged star, enjoying the stability of the main sequence. Predominant elements are hydrogen and helium (respectively 92.1% and 7.8% by number of atoms). The production of energy takes place at the Sun's core, where nuclear fusion of hydrogen leads to the formation of helium nuclei. In about 5 billion years from now, the Sun's core will finally run out of hydrogen and step into the next phase of its evolution, becoming a red giant. The life cycle of a star develops at enormous time scales, difficult to imagine due to our much shorter conception of time. Though when observing the Sun at time scales comparable to our perception, variability is noticed as well. It is evident in the case of the solar activity cycle, with an average period of 11 years. The number and latitude of sunspots varies along the cycle, increasing and appearing at lower latitudes as the peak of maximum activity approaches. During each activity cycle the

global magnetic field polarity of the Sun reverses, which accounts for a total duration of the solar magnetic field cycle of 22 years (Hale cycle). At the smaller time scales of hours to minutes coronal mass ejections may be observed, while at the even smaller time scales of minutes to seconds violent flares may occur.

Especially relevant for this work is the solar atmosphere, which is described in the next sections layer by layer from the innermost photosphere to the outermost corona, followed by a short review on the effects of solar wind on Earth, showing the importance of CMEs as determinant factors of space weather.

1.2 The spotted photosphere

The photosphere is the layer of the Sun that is easiest to observe, though it is the lowest level of the solar atmosphere. It is very thin and dense in comparison to the other atmospheric levels. While its density is 10000 smaller than the Earth's atmosphere, the photosphere is so remarkably opaque that it appears to us as a solid body. When observing the Sun's disk, the edges appear darker than the central region. This effect is dubbed limb darkening (evident in the later introduced Figure 1.2.a).

The photosphere radiates most of the energy released by the Sun, involving wavelengths that range from about 200 nm (ultraviolet) to some few μm (infrared), thus covering visible wavelengths. The spectral flux, i.e. the distribution of the energy in function of wavelength resembles that of a blackbody at the photosphere's T_{eff}=5777 K. For a blackbody, the amount of radiation over all wavelengths increases with the fourth power of temperature and its maximum shifts to shorter wavelengths as the temperature increases. When observed with higher resolution, the solar spectrum presents dark absorption lines, termed Fraunhofer lines. Several series of absorption lines have been identified, being the strongest ones the hydrogen and the Lyman series. Especially useful in this thesis were images taken in the Hα line (656.3 nm[*]). A magnetic phenomenon related to Fraunhofer lines is the Zeeman splitting of lines. An electron orbiting the nucleus of an atom generates an electric current, which in turn generates a magnetic field. When the latter one interacts with an externally applied magnetic field, it produces an addition or subtraction from the energy that is normally carried by the photons that form the spectral line. The presence of magnetic fields at the Sun was proved by Hale in 1908, based on the splitting of lines that he noticed in sunspots. The Zeeman effect allowed as well the invention of the magnetograph, which measures magnetic fluxes based on the circular (opposite) polarization of the two displaced components. Magnetograms have revealed the existence of magnetic flux all over the Sun, intricately distributed generally in pairs of opposite magnetic polarity (see Figure 1.1). These are joined by magnetic loops that extend farther up from the photosphere, and which form a complicated network termed magnetic carpet.

[*] The units Å and nm are used intermittently throughout this work, according to the general terminology employed for each spectral line.

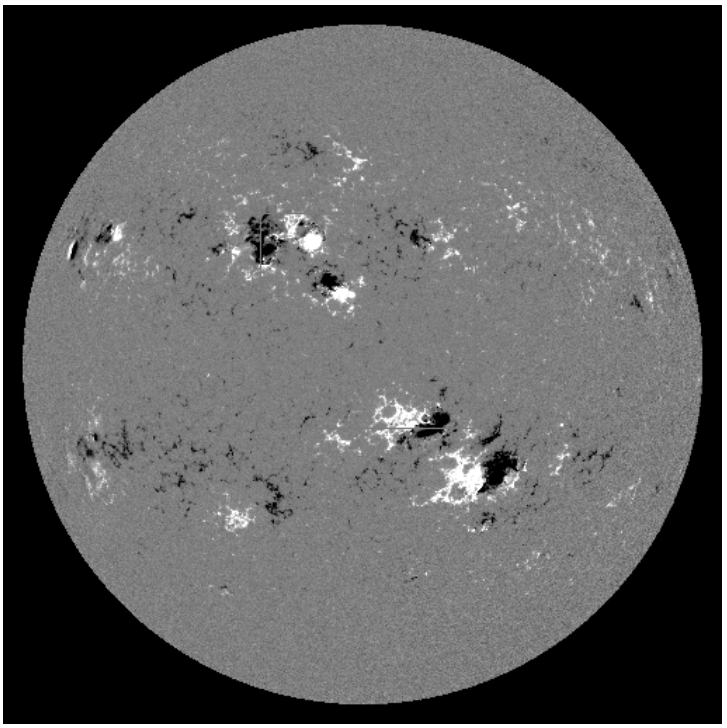

Figure 1.1. Photospheric magnetic field structure on May 20, 2000, as detected by the MDI instrument onboard SOHO. White areas denote positive magnetic polarities, i.e. field lines going out of the Sun, while black areas correspond to negative polarities, i.e. field lines sinking on the Sun's surface.

The solar photosphere is basically dominated by three different features: sunspots, faculae and granules, described below.

Sunspots

Dark spots on the Sun's surface were discovered long before the invention of the telescope, contrary to Aristotle's beliefs that regarded the Sun as an immaculate body. Due to their dark umbra and their large size of tens of thousand km, they are certainly the most prominent features of the solar photosphere. Sunspots appear dark because of their lower temperature in comparison with their surroundings, as shown in Figure 1.2.b. At the sunspot's centre, the umbra, the temperature is about 4000 K. The umbra is surrounded by a brighter filamentary structure called penumbra, where plasma outflows take place along the fibrils. This outward flow is called Evershed effect (Evershed 1909). Another interesting effect is that discovered by Alexander Wilson, observable when a sunspot is near the limb. When this happens, the sunspot seems depressed with respect to the surrounding photosphere, probably as an outcome of the lower temperature and hence lower opacity in the umbra (Wilson 1965). With the help of the Zeeman effect (Zeeman 1897), it was found that the magnetic field strength in sunspots may reach ~3000 G. The magnetism is higher in the umbra, where magnetic field lines converge. Sunspots tend to occur in pairs of opposite magnetic polarity, sometimes forming complex groups. Generally, the leading spot of the pair (the one closer to the equator) is of the same polarity as the Sun's global dipole magnetic field polarity in that same hemisphere. The magnetic field snapshot presented in Figure 1.1 corroborates this phenomenon, called Hale's polarity law. The leading spot has the highest field strength, while the following spots of opposite polarity have weaker fields. Magnetic field lines connecting opposite polarities rise above the photosphere in form of loops. While sunspots with their strong fields are directly related to active regions, there are other magnetic areas related with remnants of former sunspots. These are located at higher latitudes

and their associated magnetic field lines are so spread that they can cover wide areas on the visible solar disk.

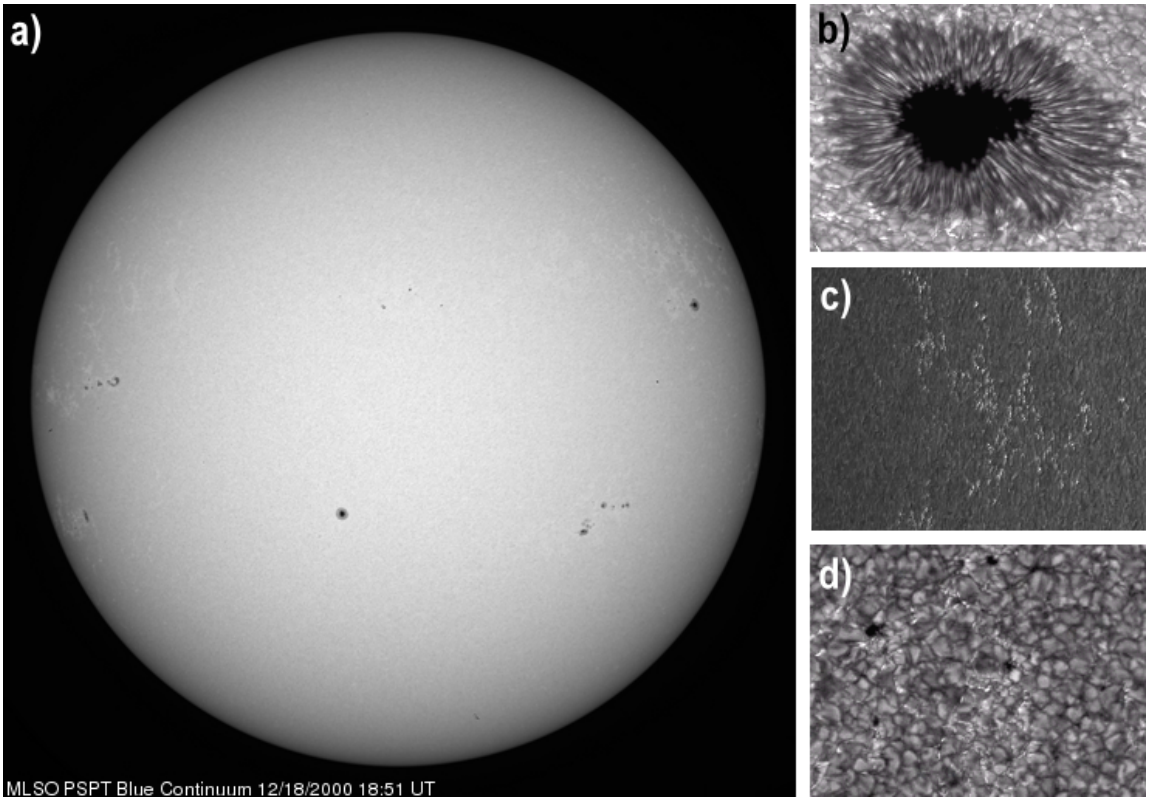

Figure 1.2. The solar photosphere and its main features. a) Full disk image of the Sun in visible wavelengths, recorded on December 18, 2000 by the PSPT (Precision Solar Photometric Telescope) at the Mauna Loa Solar Observatory (*http://mlso.hao.ucar.edu/cgi-bin/mlso_homepage.cgi*). b), c), and d) where captured by the DOT (Dutch Open Telescope) at the Roque de los Muchachos Observatory (*http://dot.astro.uu.nl/*), and correspond to b) a sunspot, c) faculae, and d) granulation.

The behaviour of sunspots allowed for many remarkable findings. In the early XVII century, Galileo watched sunspots with his telescope as they travelled from east to west across the Sun's disk. He attributed this fact correctly to the rotation of the Sun, and derived its period of 'one lunar month'. The inclined paths followed by sunspots gave hints about the tilt of the Sun's axis. Furthermore, it was noticed that they were confined to two bands centred at around 20° of latitude in both hemispheres. In 1843, a German pharmacist called Heinrich Schwabe recognized the eleven-year sunspot cycle in his own records of sunspots numbers. Two decades later, Richard Carrington discovered the Sun's differential rotation, when he realized that sunspot rotation periods depended on their latitude. Spots near the solar equator had a period of ~27 days as observed from Earth (synodic period; longer by about 2 days than the true, sidereal period) and those sunspots at higher latitudes had periods of ~29 days. Carrington also noticed how sunspots migrate to lower latitudes as the solar activity cycle evolves from one minimum to the next. Figure 1.3 shows this fact in what is known as 'the butterfly diagram'.

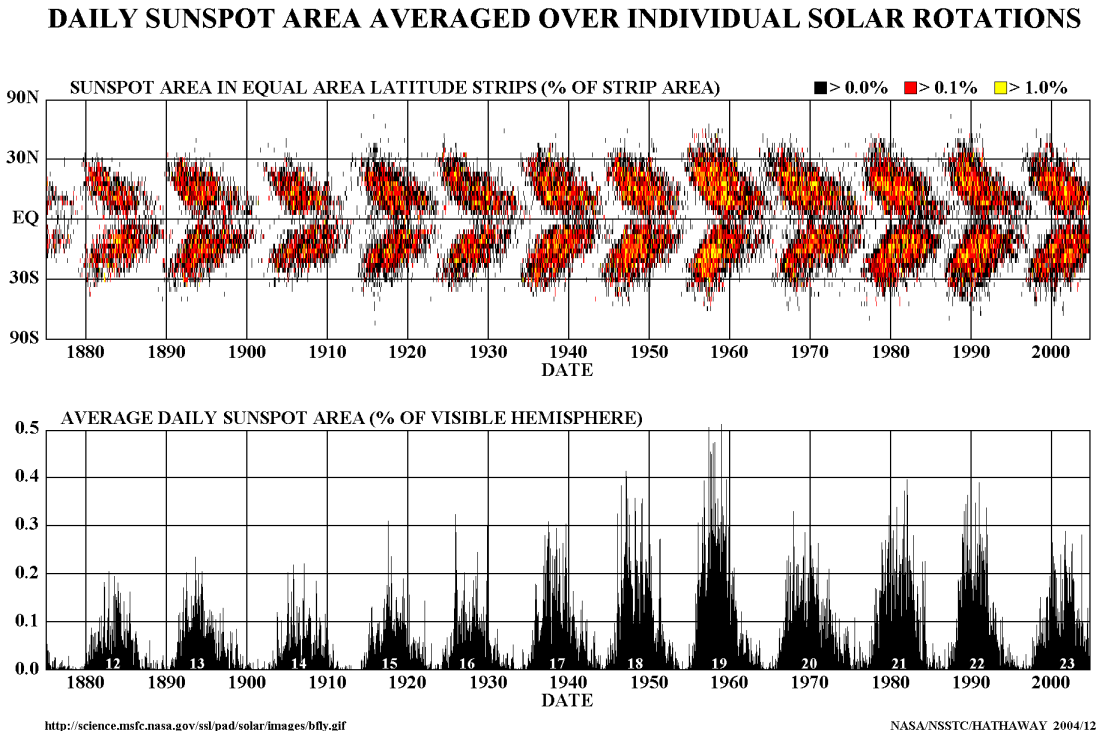

Figure 1.3. Sunspot measurements starting in 1874 with data compiled by the Royal Observatory of Greenwich. Top: butterfly diagram. It indicates the latitudinal location of sunspots, which migrate towards lower latitudes during each 11-year cycle. Bottom: sunspot areas over the course of 12 solar cycles of 11 years. Courtesy of D. Hathaway, NASA/NSSTC.

Faculae

The white-light photosphere presents as well bright regions known as faculae, from the Latin 'little torches' (see Figure 1.2.c). They only shine when located near the solar limb, as can be confirmed from Figure 1.2.a. Closely associated with the chromospheric network (see next section), they appear bright because of being about 300 K hotter than their surroundings. Faculae are associated with strong magnetic fields as well, but in this case the field lines come together in smaller sets. They can be found all over the photosphere, but specially around sunspots, with magnetic fields of 100-300 G. In times of maximum solar activity sunspot-faculae are brighter, producing a small increment in the total brightness of the Sun.

Granules

Higher resolution images of the solar photosphere exhibit a characteristic pattern of 'small' grains which are in constant motion, emerging, fragmenting, merging and decaying. Pictured in Figure 1.2.d, these features are known as granules, and have average sizes of roughly 1100 km. These polygonal shapes are all over the photosphere, except in locations of sunspots, and therefore configure what is historically known as 'quiet Sun'. The stretching of granules near sunspots is associated with strong horizontal magnetic fields. The bright granules are separated by the intergranular lanes, whose darker colour indicates their lower temperature. Granules are apparently the upper part of convection cells, which carry upward hot gas at speeds of ~1 km s^{-1}.

Once the energy is released, the gas cools and falls inward through the intergranular lanes. Typical granule lifetimes range from 10 to 20 minutes.
Supergranules are larger-scale convection cells of about 35000 km, which extend deeper and have lifetimes of approximately a day. They are best observed in Doppler shift measurements. The transport of magnetic fields by the flowing plasma in supergranules towards the edges of the cells is associated with the chromospheric network.

1.3 The jagged chromosphere

Immediately above the photosphere sits the chromosphere, observable during totality in eclipses as a reddish irregular rim around the occulting moon. This attribute determined its name, which derives from the Greek word chromos (colour). Its temperature rises from the minimum photospheric temperature up to around 20000 K (see Figure 1.4). This fact suggests the existence of a non-radiative mechanism which accounts for the heating of the chromosphere. It is believed that shock waves, generated by sound waves from the interior, are responsible for heating in the lower chromosphere. Higher up heating is attributed to Alfvén waves, produced by displacement of magnetic field lines.

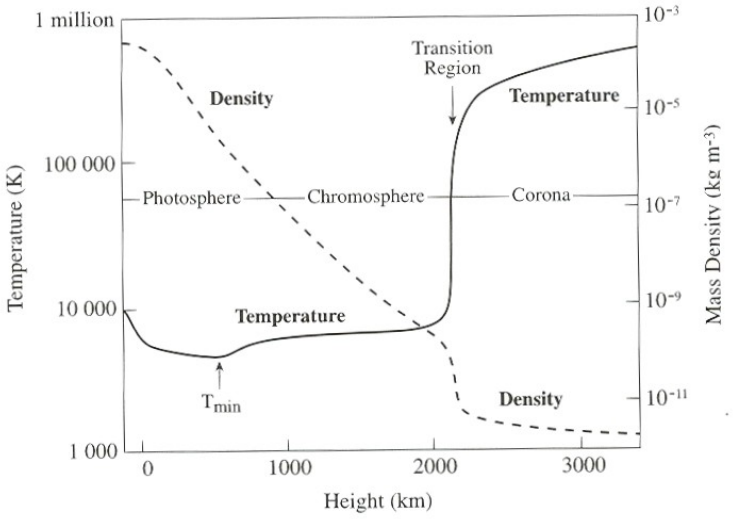

Figure 1.4. Temperature and density profiles of the solar corona. Adapted from K. Lang (2001).

The relatively thin chromosphere has such a low density that it does not create absorption lines. Rather, during a total eclipse the spectrum shows intense emission lines at exactly the same positions where many absorption lines were located in the photospheric spectrum, with some exceptions. The strongest lines are those of hydrogen alpha (Hα) and ionized calcium (Ca II) H and K lines. The Hα emission line, at 656.3 nm, is responsible for the reddish colour of the chromosphere. This line is photoelectrically controlled, i.e. its intensity depends on the ability of the photospheric photons to generate Hα photons via the excitation of hydrogen atoms. Therefore, it does not provide hints about the chromospheric temperature. However, there are other lines that give temperature information. Such emission lines are those of Ca II H and K, at 393.4 and 396.8 nm respectively. The mechanisms that give rise to the creation of these lines are fundamentally collisional, thus providing information about the local temperature. Because the photosphere shines so strongly, the only way to observe the chromosphere is to isolate its emission at a particular wavelength. This is achieved by means of an instrument called spectroheliograph, invented by Hale in 1892, which records the solar disk at a certain

wavelength. *Diverse features are observable depending on its tuning frequency, which are described next.*

Chromospheric Network

The meshed pattern known as chromospheric network shows up more clearly in the Ca II K lines, which indicate the location of intense magnetic fields. The ultraviolet line of Ca II K (centred at 393.4 nm) is due to singly ionized calcium and presents broad wings. By tuning the spectroheliograph along these wings, it is possible to produce images at different parts of the line profile, and hence at different heights. For instance, the blue wing of Ca II K, at 0.03 nm from the line centre (K1) corresponds to the temperature minimum between photosphere and chromosphere (see Figure 1.5). Images at 0.015 nm from the line centre (K2) relate to the low chromosphere, at about 1500 km altitude. The centre of the Ca II K line (K3) is associated to the high chromosphere. The bright areas associated with strong magnetic field coincide with the location of sunspots and with the supergranule convection cells. The magnetic network outlines the boundaries of supergranules, since flows in supergranulation cells induce magnetic field lines to their outer edges (see the 1st and 2nd panels of Figure 1.8, measured at wavelengths of 124.9 and 125.0 nm respectively). It is believed that these concentrated field lines spread out at higher latitudes to form the silhouette of a canopy.

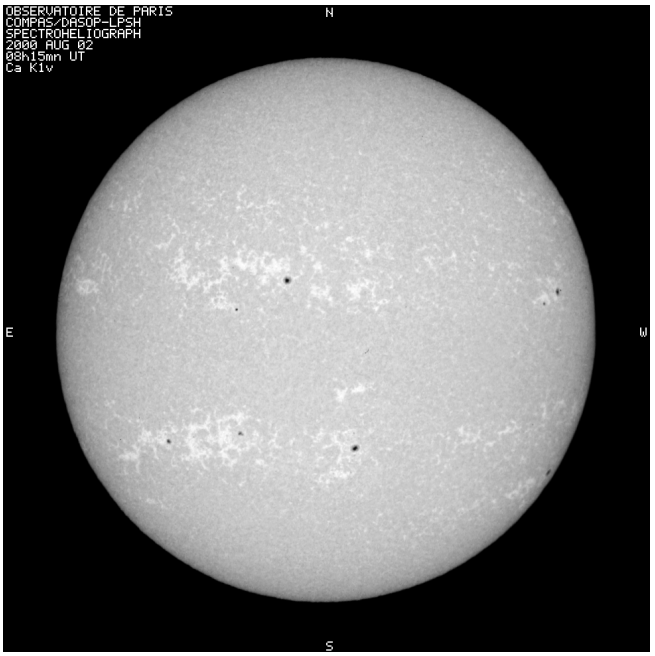

Figure 1.5. Full disk image of the Sun in the line of Ca II K1v, taken on August 2, 2000 by the spectroheliograph at the Meudon Observatory (*http://bass2000.-obspm.fr*).

Dark spots and plage

The close relationship between chromospheric features and photospheric magnetic fields is present as well in the Hα line. Dark regions are present in the locations of sunspots, while bright plage is detectable as bright patches around these dark regions. Plages, indicating the existence of concentrated fields, are directly associated with the shining photospheric faculae. A snapshot of the Sun in Hα is shown in Figure 1.6, where a dark spot and its surrounding plage have been zoomed out in b).

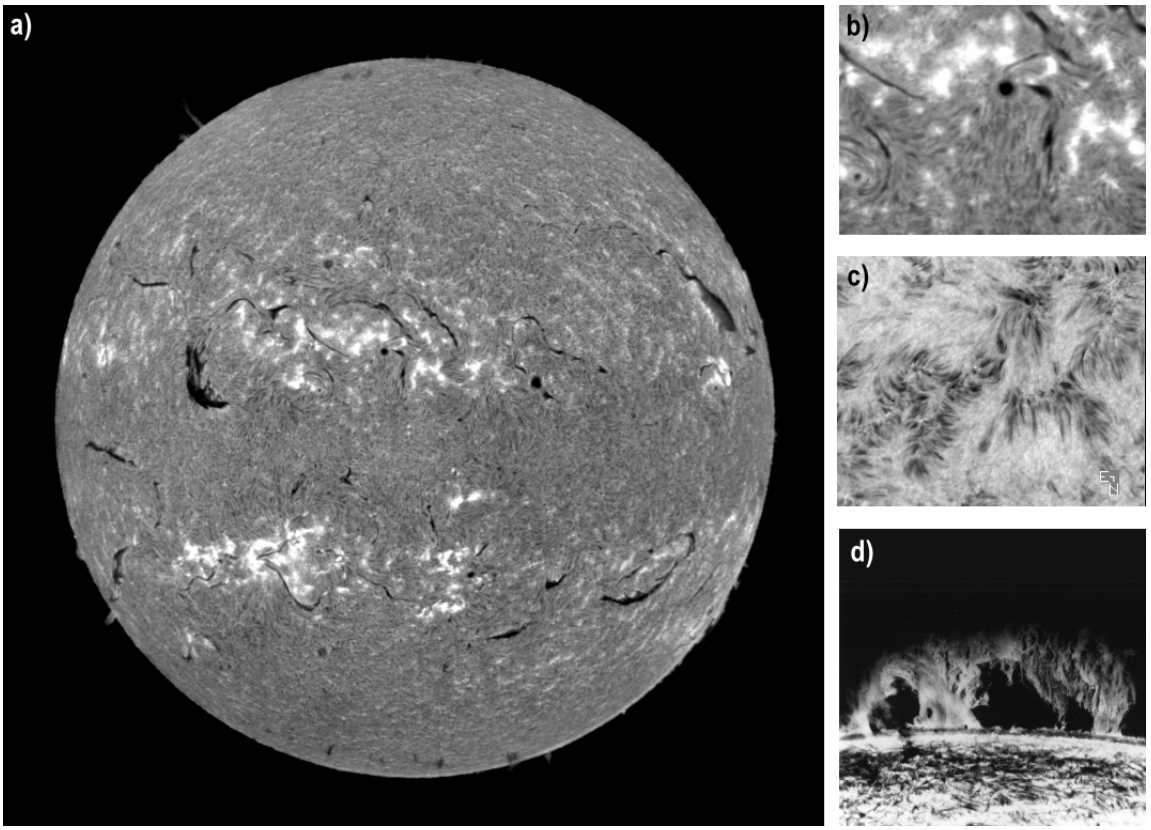

Figure 1.6. The Sun in Hα wavelengths. a), b) and c) were recorded by the 20-cm refractor telescope at the Big Bear Solar Observatory (*ftp://ftp.bbso.njit.edu*). a) Full disk image on August 2, 2000. b) A dark region and its surrounding plage. c) Spicules. d) A quiescent prominence photographed at the edge of the Sun in 1970 (credits: BBSO/NJIT).

Spicules

The irregular character of the chromosphere is mainly due to spicules, grass-like features visible in Figure 1.6.c. At a given time, there are approximately 500 thousand of them distributed all over the Sun, overlapping the chromospheric network. Spicules can be as long as 15000 km and around 2000 km thick (see also the 3rd and 4th panels of Figure 1.8, recorded at wavelengths of 123.8 and 62.9 nm respectively). Their typical lifetimes range between 1 and 10 minutes, and they rise with speeds of about 25 km s^{-1}. Doppler-shift measurements reveal the high dynamism of spicules, which may rotate and oscillate during their existence, until they expire either by fading or descending. Although surrounded by much hotter plasma from the corona, their temperatures are maintained to chromospheric levels.

Filaments and Prominences

Long, dark structures on the solar disk seen at Hα wavelengths are given the name of filaments. They are very dense, rather cool features with temperatures of about 10000 K, immersed in a hot corona of 2 million K. Filaments are optically thick, and are seen in absorption on the solar disk as dark lineal features. Figure 1.6.a displays an Hα image of the Sun, with filaments preferentially located at two latitudinal bands. Filaments are supported above the solar surface by magnetic field loops, along neutral lines that separate regions of opposite polarities. When observed on the solar limb (not from top but from the side), filaments are seen in emission, and

are particularly called prominences. Prominences appear as bright loops against the dark background, in contrast with filaments which are seen dark due to the bright background Sun. A quiescent prominence at the limb is shown in Figure 1.6.d. All the mass contained in a prominence is held up by strong magnetic fields up to 50000 km above the photosphere, opposing the downward gravity force.

Prominences can be basically classified in two categories: active and quiescent. Active prominences are related with active and sunspot regions, subtending lengths of the same scale or smaller. They are highly dynamic and have hence very short lifetimes, which finish with violent eruptions, usually accompanied by flares. Conversely, quiescent prominences are associated with decaying, weak bipolar magnetic regions. Typical lengths are of the order of 100000 km, but they can reach up to 600000 km. These structures may last even several months in a quiescent state until they readily erupt, ascending with velocities of some few hundred km s^{-1}. The eruption of a prominence on the limb is observed on the disk as a sudden disappearance of a filament, because the blue-shifted filament is out of the narrow band tuned by the spectroheliograph. After such an event, also called disparition brusque, two bright bands often form along both sides of the former filament location. These bands seen in Hα are known as two-ribbon flares, and have counterparts in other wavelengths (e.g., in the Fe XII line at 195 Å).

According to their location, two groups of prominences can be distinguished: those which move with sunspots towards the equator as the solar cycle evolves, and those which migrate towards higher latitudes. The latter ones appear after the peak of maximum solar activity and may form a polar crown that may extend almost all around the Sun (McIntosh 2003).

In all, the chromosphere exhibits striking dynamic processes, which include beautiful prominence eruptions, sudden filament disappearances and flare activity.

1.4 The grand corona

Higher up in the solar atmosphere glows the magnificent but dim corona. Its brightness is just about one millionth than that of the solar photosphere. It is so tenuous, that the only means of observing it is to block the intense glare of the solar disk. Since prehistoric times, the amazing fact that the Sun and the Moon have almost equal apparent sizes as seen from Earth, has allowed the observation of the solar corona. When the Moon is aligned with the Earth in a manner that it obstructs the solar surface, the marvel of a total solar eclipse occurs. The oldest liable record of an eclipse sighting dates from 763 BC. It was found in Babylonia and was related with a partial eclipse, i.e. only a portion of the solar disk was covered by the Moon. Chinese and Indians have reported eclipses as well in similar epochs. Sporadic records with posterior dates have been found, but recurrent eclipse observations began in the mid XIX century together with photographic records. In 1930 Bernard Lyot invented the coronagraph, an instrument that occults the solar disk and thus allows, independently of eclipse occurrence, for routine coronal observations at high altitudes.

White-light coronagraphs record the three main components of the white-light spectrum: K-, F-, and E-corona. The polarized K-corona is caused by Thomson scattering of photospheric light by free electrons in the solar corona. Its spectrum is continuum (K stands for the German kontinuierlich), without the Fraunhofer absorption lines present in the case of the photospheric spectrum. The electrons in the approximately two million K gas move so fast that the Fraunhofer lines are very broadened by Doppler shifts, and the lines are no longer discernable. The emission

of the K-corona dominates up to a height of about 2 solar radii, where the density is around 10^{-12} kg m^{-3}. Since the amount of light scattered in the K-corona is proportional to the number of electrons, the calculus of the electronic density is straightforward, in a good approximation. However, the density derived from the polarized coronal brightness is a measure of the quantity of electrons piled-up along the line of sight, and not at a particular distance from the observer. The unpolarized F-corona dominates from 2.5 solar radii on, and is due to sunlight diffracted by dust particles floating in space. Since the motions of these dust grains are slow, Doppler shifts are negligible and this emission does show the Fraunhofer lines. The E-corona is made up of spectral line emission due to highly ionized elements, primarily hydrogen and helium, but also minor atoms such as carbon, nitrogen and oxygen.

In the solar corona, the thermal pressure is commonly lower than the magnetic pressure of loops (e.g., Foukal 1975). The ratio of these two quantities is given by a parameter called plasma-β, which in the case of the corona is usually considerably less than unity. Due to the governing strong magnetism, electrons are confined within coronal loops, and therefore aligned with and shaped by the magnetic field structure. This implies that the coronal plasma is 'frozen' and obliged to flow along magnetic lines of force, and not across them. Conversely, in the case of the photosphere the thermal pressure is higher than the magnetic pressure, where the gas transports the field and eventually modifies the overlying coronal structure. Due to the photospheric magnetic field arrangement, the corona above it is highly structured and inhomogeneous. Its constituting magnetic field lines may be classified in two categories: closed and open field lines. Closed field lines are regarded as those which connect back to the solar surface. They constitute bright and dense loops which confine hot plasma, mostly found in active regions. Higher up in the corona, field lines may open up and lead to a flow of slow solar wind (Parker 1958), of ~400 km s^{-1}. Open field lines extending to interplanetary space, constitute the supply of a fast solar wind of ~800 km s^{-1}. For theoretical reasons these field lines must close back somewhere, but they do it so far in space that they can be considered as opened (e.g., Bird & Edenhofer 1990). Open field lines are found predominantly in polar regions, in the so-called coronal holes.

It took seven decades to deduce the existence of a million-degree corona, after the discovery of a very strong green line in the coronal spectrum, during an eclipse in 1869. This emission line, located at a wavelength of 530.3 nm, could not be attributed to any known terrestrial element at that time. Therefore it was assumed that a new element had been detected, which was named 'coronium' (e.g., Claridge 1937). Later on, new lines were observed and new elements were proposed, though it became clear that such elements could not fit into the periodic table of elements. The enigma was solved in 1939 and 1942 by W. Grotrian and B. Edlén respectively (see Edlén 1942). They found that those elements were in fact known in Earth, but were in an improbable 'forbidden' state of high ionization. For instance, the supposed 'coronium' resulted to be related with iron 13 times ionized. This could only occur at high temperatures of about a million K. Very low densities are additionally required, which prevent electron collisions of destroying the formed ions. Low coronal densities of 10^{15} electrons per cubic meter satisfy this condition. However, coronal heating poses an essential problem in solar physics. The high coronal temperature seems to violate the second law of thermodynamics, since it is expected that the temperature decays further out from the photosphere (T = 5780 K). It actually happens, until a minimum of about 4400 K below the chromosphere (see Figure 1.4). After that, the decrease in density is compensated by an increase in temperature, keeping the gas pressure spatially

constant. The most abrupt temperature increase takes place in a thin layer between chromosphere and corona, the transition region.

New hints on the processes involved in coronal heating arise from observations in the extreme-ultraviolet (EUV) and soft X-rays regimes, where the corona emits most of its energy. Since mainly optical and radio wavelengths survive the filtering of the Earth's atmosphere, all other wavelengths must be measured from space. Space borne telescopes allowed such observations, signifying a major advance in coronal studies. They have covered from the shortest-wavelength gamma-rays, X-rays, EUV and reaching the ultraviolet. The gamma-ray radiation has wavelengths in the range 10^{-4} to 10^{-2} nm (energies of 100 keV to 10 MeV), and is emitted when particles in flares are accelerated to high energies. Hard X-rays are emitted at wavelengths of 0.01 to 0.1 nm (10 to 100 keV), and are associated with electron bremsstrahlung from nonthermal electrons that cross the transition region and chromosphere. Soft X-rays at 0.1 - 10 nm (0.1 to 10 keV) are due to free-free emission of electrons scattered by highly ionized ions, and are found in active regions ($T \approx 1.5 – 10$ MK) and in flare loops ($T \approx 10 – 40$ MK). Finally, EUV wavelengths range from 10 to 100 nm (temperatures of 0.15 to 1.5 MK). They are produced by free-free emission of electrons scattered by ions at lower temperatures than soft X-rays, from Fe IX (blue-coloured images in Figure 1.7) to Fe XV (yellow-coloured images in Figure 1.7). Different ions are formed at different temperatures, and therefore their emitted spectral lines are directly related with the bulk temperature of the plasma. Since temperature varies with height, a certain line might also be regarded as a measure of the different layers of the solar atmosphere.

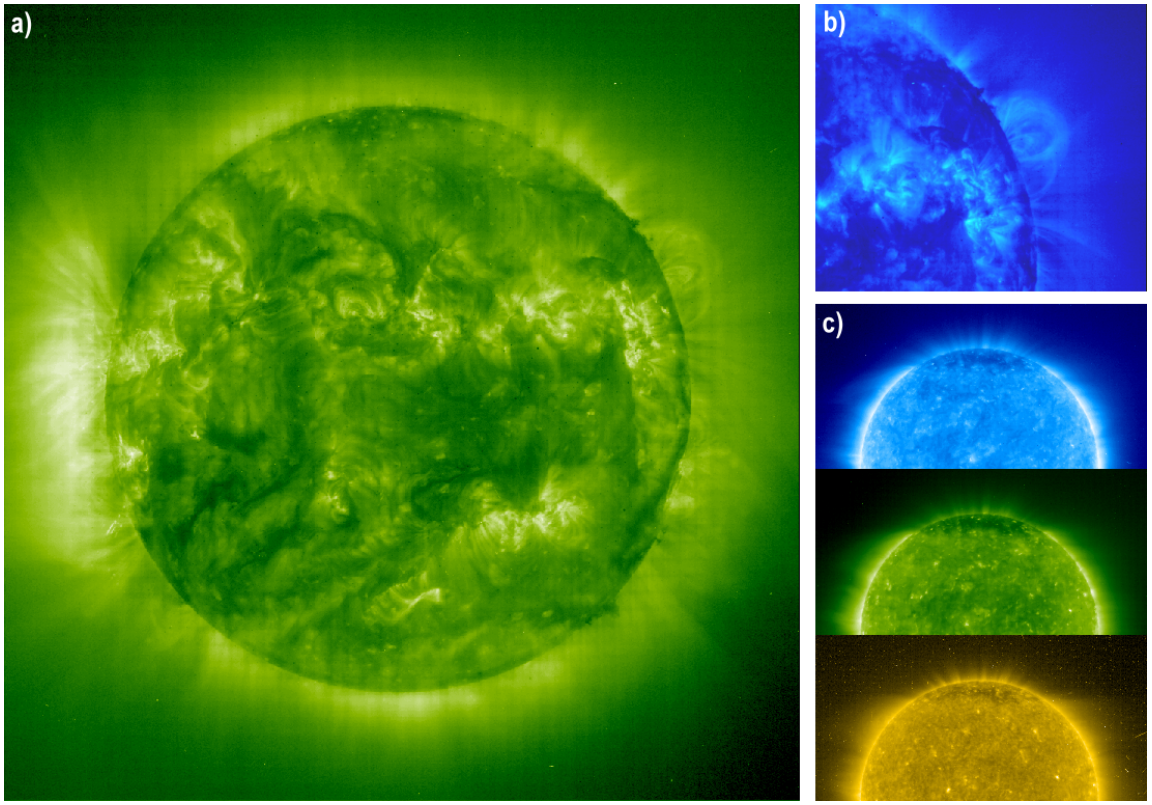

Figure 1.7. The low corona, as captured by the EIT instrument onboard SOHO. a) Full disk image of the low corona in the EIT 195 Å line (Fe XII), on December 18, 2000. b) EIT loops on the same day, but detected in the line of 171 Å (Fe IX). c) Coronal holes and plumes imaged on May 26, 1996, from top to bottom: EIT 171 Å, 195 Å and 284 Å (FeXV).

The Transition Region and Coronal Explorer (TRACE; Wolfson et al. 1997) is a NASA mission that images the corona in the EUV and UV regimes, with pass-bands located at 173 Å (Fe IX), 195 Å (Fe XII), 284 Å (Fe XV), 1216 Å (H I Ly-α), 1550 Å (C IV), 1600 Å (CI, Fe II) and 1700 & 5000 Å (continuum). Its exceptional angular and temporal resolution has revealed a highly inhomogeneous corona characterized by plenty of dynamics. TRACE has also demonstrated that our previous view of the corona as built up of stratified layers seems not to be proper.
A whole variety of coronal features is evident from images recorded by space-borne telescopes at diverse wavelengths. They include not only coronal loops but also streamers, coronal mass ejections, coronal holes and plumes.

Coronal loops

Images at the optically thin soft X-rays and EUV emissions have revealed a wealth of loops in the low corona and transition region, particularly located above sunspots and active regions. The feet of these loops are anchored in regions of opposite magnetic polarities, and hence they constitute areas of closed magnetic field lines. The hot coronal plasma is constrained to flow along these highly magnetized loops. The cooler ones are visible in EUV (as in Figure 1.7.b) and the hotter ones in soft X-rays. The amount and brightness of the loops varies along the solar cycle, since they are directly associated with sunspots and active regions (see, for comparison, Figure 1.7 a, captured near solar maximum, and Figure 1.7 c, recorded in solar minimum). Some loops may last even for weeks, but most of them reveal dynamics on shorter time scales. The latter is the case of post-flare or post-eruptive loops, which shine from minutes to hours, presumably after magnetic reconnection processes in the course of eruptions (Kopp & Pneuman 1976; Webb & Hundhausen 1987). When overlying extended bipolar regions, the loops line up to form an arcade, with their footpoints coinciding with the location of an Hα two-ribbon flare (Asai et al. 2004).

Coronal holes

Coronal holes are dominated by open magnetic field lines, with one end anchored in the solar surface and the other extending in interplanetary space. Coronal holes are most of the time present at the solar poles, especially during minimum solar activity, when they reach maximum areas (about 15% of the solar surface, according to NSO/KP data, see Subsection 2.3.3). Smaller ones may be found at lower latitudes, usually during the declining phase of the solar cycle, and are related with the Sun's magnetic field reversal (Webb et al. 1984, Bilenko 2002). They efficiently allow heated plasma to flow outward in what is called the fast solar wind. Therefore, coronal holes contain just small amounts of hot material and hence they appear as dark features in EUV (as in Figure 1.7.c and Figure 1.8, last two panels on the bottom) and X-ray images. On the contrary, the near-infrared line of neutral helium (at 10830 Å) reveals coronal holes as bright features. This line, a good indicator of coronal holes, forms in the chromosphere and transition region.

Polar Plumes

Polar plumes are thin and faint linear coronal features, which extend radially outward from the solar poles (e.g., Lamy et al. 1997). They are also associated with open magnetic field lines, and

thus they can be found at the locations of the polar coronal holes. Examples of polar plumes are displayed in Figure 1.7.c and Figure 1.8 (5th and 6th panels, measured at wavelengths of 62.4 and 124.2 nm respectively). Mostly visible in solar minimum, they seem to delineate the dipolar magnetic field component of the Sun, with values of about 10 G. This is suggested by the location of the plumes' footpoints, which coincide with small-scale magnetic areas on the photosphere. The process involved in the formation of the polar plumes is related with the fast solar wind streams, in a similar manner as the slow solar wind flows outwards from the top of streamers (Wang 1994).

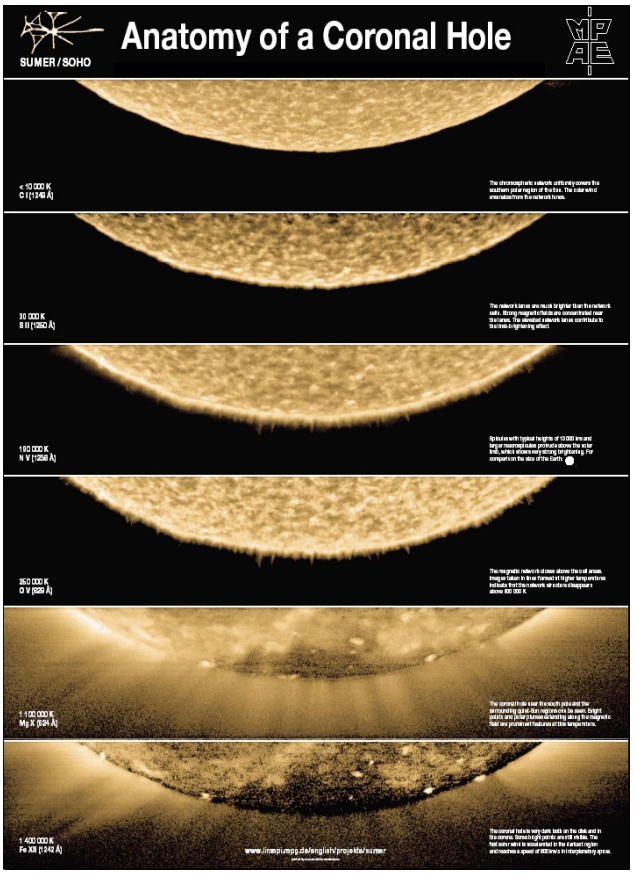

Figure 1.8. A coronal hole on the southern pole of the Sun, imaged at several UV spectral lines by the SUMER (Solar Ultraviolet Measurements of Emitted Radiation) instrument onboard SOHO (*http://www.mps.mpg.de/projects-/soho/sumer/*). The various temperatures at which the lines are formed increase from top to bottom: 10 000 K, 30 000 K, 190 000 K, 250 000 K, 1.1MK and 1.4 MK. Image courtesy SOHO/SUMER consortium.

Streamers

Coronal streamers are visible in white light as large spiked structures that extend radially to several solar radii, as visible in Figure 1.9 and Figure 1.10. They are termed helmet streamers if a cavity is detectable at their base, usually located above active regions and prominences. Such helmet streamers are evident in Figure 1.10.a. and b., in the west and east limbs respectively. The cavity is comprised of loops anchored in the photosphere, which confine dense plasma (e.g., Koutchmy & Livshits 1992). Magnetic field lines connecting areas of opposite polarities are involved in the lifting of prominences (or filaments) above the solar surface. While the lower part of a helmet streamer corresponds to areas of closed magnetic fields, the stretched stalk further above is associated with leaking of plasma that constitutes the slow solar wind (e.g., Pneuman 1969; Schwenn 1990). This occurs at heights where the magnetic pressure fails to confine plasma, related with a plasma-β higher than unity.

The distribution of streamers is decisive in shaping the corona, and as many other solar features it varies along the solar cycle. Near minimum solar activity, streamers are confined to equatorial

latitudes (see Figure 1.9 and Figure 1.10.a.). In this manner, streamers form all around the Sun at equatorial latitudes, giving rise to an equatorial current sheet delimited by regions of opposite polarities, and which resembles a 'ballerina skirt'. Even though at heights above 2 solar radii only one streamer belt is observed at equatorial latitudes, near the Sun two streamer belts can be discerned, which sit at about ±30° latitude (see LASCO/C1 image in Figure 1.9). On the other hand, at times of maximum solar activity, streamers are found all around the solar disk, even at polar latitudes, as evident in Figure 1.10.b.

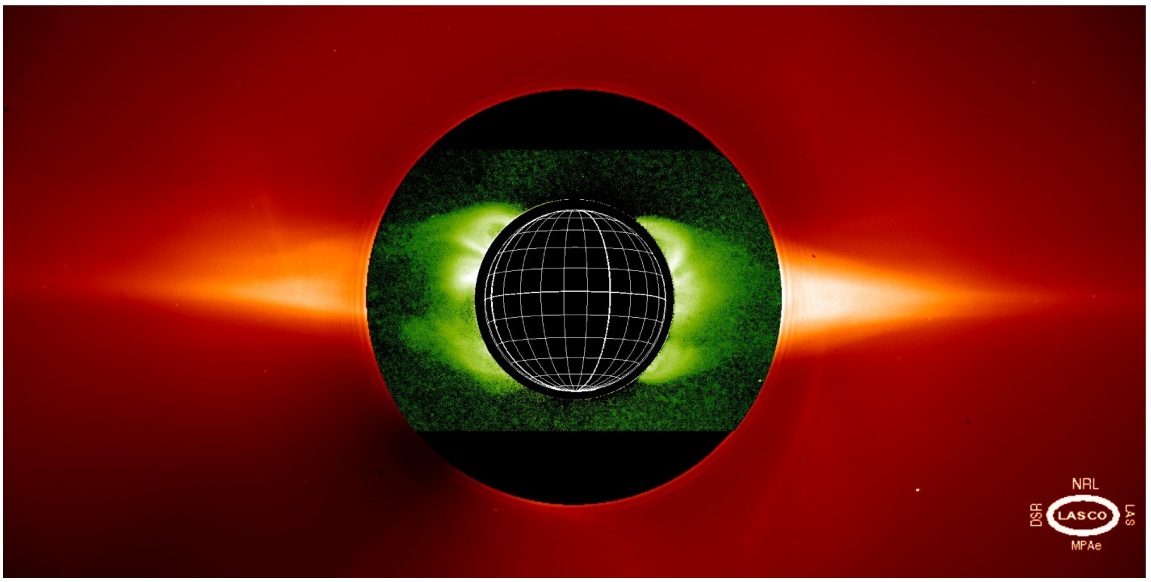

Figure 1.9. The solar corona on February 1, 1996, in a composite image of LASCO/C1 (in green) and LASCO/C2 (in orange). Courtesy of SOHO/LASCO Consortium.

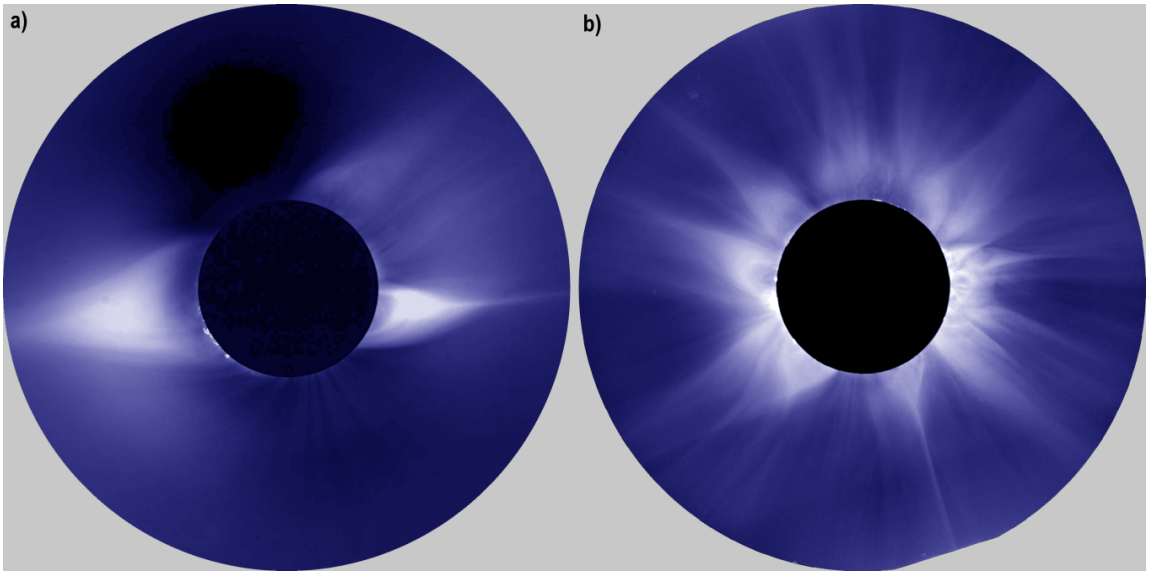

Figure 1.10. Ground-based observations of the solar corona taken during total eclipses. a) The corona in solar minimum, as photographed by the High Altitude Observatory (HAO) team in Putre, Chile, on November 3, 1994. b) The corona in solar maximum, photographed by the HAO and Rhodes College teams from Palem, India, on February 16, 1980.

X-ray structures

Besides coronal loops, soft X-ray measurements show a variety of structures. They include soft X-ray jets, X-ray bright points, cusps, and sigmoids, shown in Figure 1.11. Soft X-ray jets take place when heated plasma streams along an open field line (e.g., Shibata et al. 1992, Aschwanden 2004). X-ray bright points are distributed all over the Sun and last only for some hours (e.g., Golub et al. 1974). They are specifically associated with ephemeral regions, which are small-scale bipolar regions not related with sunspots. Cusps look as loops stretched on the top, in a triangular fashion. They are associated with X-type reconnection processes, and are observable if plasma is promptly supplied to the cusp, prior to the relaxation of the cusp into a 'normal' dipolar loop. Sigmoids are S-shaped features that suggest the existence of non-potential magnetic fields with excess energy, and have been interpreted as precursors of coronal mass ejections (CMEs) (e.g., Canfield et al. 1999; Sterling et al. 2000).

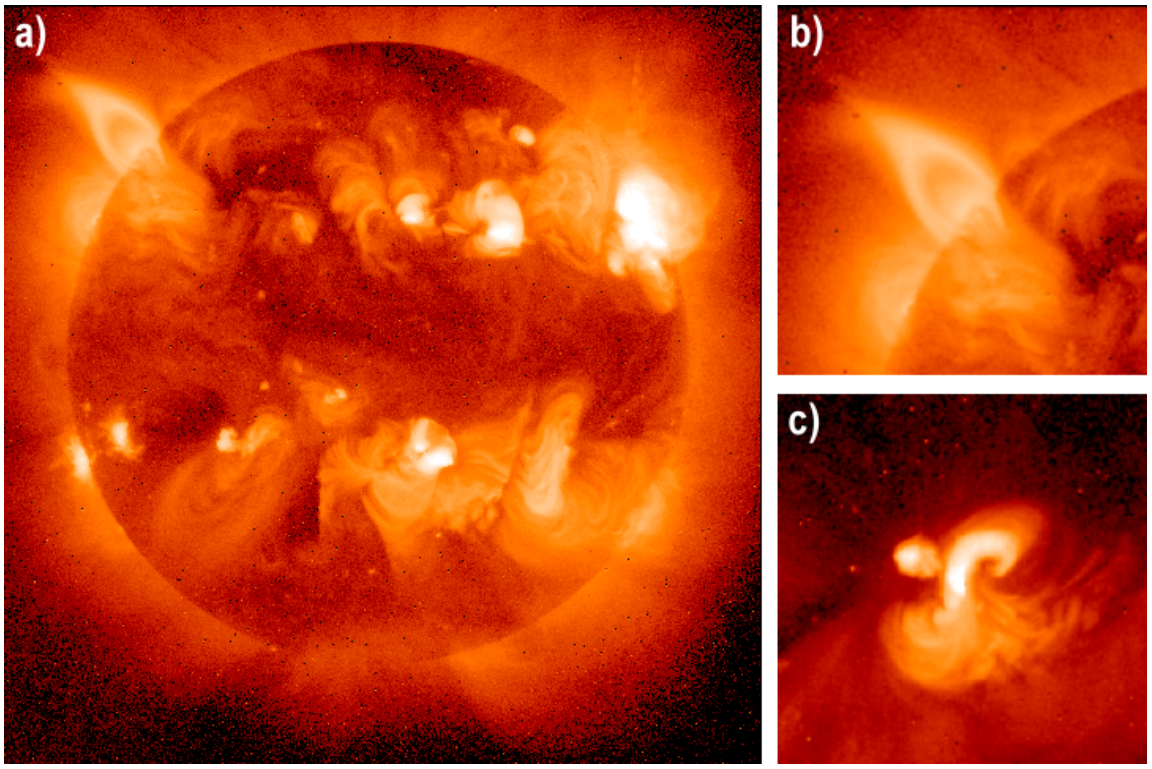

Figure 1.11. The Sun in X-rays, as captured by the SXT instrument onboard the Yohkoh spacecraft. a) Full disk image on March 18, 1999. b) A cusp formed after a CME eruption on the same day. c) A sigmoid just before a CME eruption on June 8, 1998.

Coronal mass ejections

Coronal mass ejections (or CME for short) are enormous eruptions of plasma ejected from the Sun into interplanetary space, over the course of minutes to hours (see Figure I.1). They are best observed by means of coronagraphs, whose working principle is based on the Thomson scattering process. The discovery of CMEs is attributed to the coronagraphs aboard the Orbiting Solar Observatory – 7 (OSO-7; 1971-1974) in 1973, and Skylab (1973-1974), which observed about a dozen and ~100 CMEs respectively (Koomen et al. 1974; Hildner et al. 1976). The Solwind coronagraph on the P-78 spacecraft (1979-1985) recorded more than 1500 CMEs

(*http://lasco-www.nrl.navy.mil/solwind_transient.list*, Sheeley et al. 1986). The subsequent Solar Maximum Mission (SMM; 1980, 1984-1989) detected ~1350 CMEs using the High Altitude Observatory's Coronagraph/Polarimeter (Burkepile & St. Cyr 1993). The still in operation Large Angle Spectroscopic Coronagraph (LASCO; 1996-present) onboard the SOlar and Heliospheric Observatory (SOHO) has recorded ~7000 CMEs within the period 1996-2002 (Yashiro et al. 2004). The rate of occurrence of CMEs changes along the solar cycle, with an average value of ~1 event per day during solar minimum and ~4 events during solar maximum (based on the number of SOHO CMEs per year; Yashiro et al. 2004).

The excess brightness that CMEs represent corresponds in average to masses on the order of $5x10^{12}$ to $5x10^{13}$ kg (Howard et al. 1985; Vourlidas et al. 2002). Considering the mentioned rate of occurrence, then the average mass loss rate due to CMEs results to be of about 10^{8} kg s^{-1} (i.e. 10% of the mass loss rate due to the solar wind; see next section). The speeds of CMEs are fairly constant above some few solar radii, while most of the acceleration takes place within the first couple of solar radii (St. Cyr et al. 1999). Average speeds are of the order of 400 km s^{-1} (Hundhausen et al. 1994; Yashiro et al. 2004), although they may exceed 2000 km s^{-1}. Since CMEs may travel radially outwards from the Sun in any direction, the observed speed corresponds usually to a component projected on the plane of the sky. According to their kinematical behaviour, CMEs were classified in two categories: gradually accelerating ones, related to prominence eruptions; and fast ones, related to flares (MacQueen & Fisher 1983). However, the mentioned association is arguable, and other explanations have been proposed (e.g., Low & Zhang 2002). CMEs with speeds higher than 400 km s^{-1} are usually associated with shocks, if immersed in slow solar wind. As CMEs travel across the coronagraph's field of view, they carry an average kinetic energy of 10^{23} to 10^{24} J (Vourlidas et al. 2002). Energies of similar order are attributed to flares as well, which are likely related to CMEs by the same magnetic release process, though in many cases there is no correlation (Gosling 1993; Hudson et al. 1995). Conversely, it has been proven that CMEs are closely related to eruptive prominences/disappearing filaments (Munro et al. 1979; Feynman & Hundhausen 1994).

The angular spans of CMEs may extend from just a few degrees in the case of narrow CMEs, up to 360° for "halo" CMEs that completely surround the occulter of the coronagraph. In all, average angular widths of CMEs as measured by different missions range from 24° to 72° (Howard et al. 1985, 1986; Hundhausen 1993; St. Cyr et al. 1999, 2000; Yashiro et al. 2004). Their locations vary as well and follow the streamer distribution: in solar minimum CMEs are mostly confined to equatorial latitudes, while in solar maximum their latitudinal distribution is spread, covering all latitudes. This behaviour with respect to the solar cycle has also been observed in other datasets (Howard et al. 1985, 1986; Hundhausen 1993; St. Cyr et al. 1999, 2000; Yashiro et al. 2004). A more detailed description of the CME angular widths is given in Subsection 3.3.2, while further aspects regarding CME position angle may be found in Subsections 3.3.2 and 3.5.3).

A high percentage of CMEs shows a pronounced three-part structure. These events appear as having a bright leading edge, a dark void and a bright core (Illing & Hundhausen 1985; Howard et al. 1985), as displayed in Figure 1.12. The bright curvilinear leading edge indicates the association with magnetically closed regions, and must not be confused with the shock (which if present, should form ahead of the leading edge; see Schwenn 1996). It has been suggested that the void owes its existence to the presence of a magnetic flux rope, which can be observed as circular features at the void's boundary (e.g., Dere et al. 1999; Hundhausen 1999; Wood et al.

1999). The bright core is usually comprised of cool prominence material, and in a number of cases seems to be suspended under the dark cavity. A structure such as a flux rope is a plausible entity capable of holding up prominences. In some CMEs detected by SOHO/LASCO, the flux rope structure believed to support the prominence material seems to be directly visible. That is the case of the spectacular CME that originated near the SW limb on June 2, 1998 in association with a large prominence eruption (Plunkett et al. 2000; Srivastava et al. 2000). The event, displayed in Figure 1.13, exhibits helical field lines, indicative of a magnetic flux rope structure, which seem to overlie the trailing prominence material (other examples may be found in, e.g., Wood et al. 1999). Events like this are rare because CME cavities are depleted regions, difficult to image in an optically thin medium like the solar corona. They have often been misinterpreted as concave outward moving structures after magnetic disconnections, as pointed out by Dere et al. (1999).

The possible initiation mechanisms of CMEs are still a matter of discussion. Linker et al. (2003) have sorted the variety of models that try to explain the CME origins into three classes, according to their energy source: energy driven models, thermal blast models, and energy storage models. The firsts assume a sufficiently fast injection of magnetic energy (of about 10^{25} J) in order to trigger the eruption (e.g., Heyvaerts 1974; Chen 1989). The thermal blast models suppose a rapid release of thermal energy, conferred by a solar flare (e.g., Dryer 1982; Wu 1982). Due to observational contradictions regarding the photospheric magnetic field and the small number of large flares, the last two models seem currently improbable. Energy storage models suppose that the energy needed to set the CME in motion is gradually stored in the magnetic field, e.g. by shearing and twisting it. Among these, the flux cancellation (van Ballegooijen & Martens 1989), the breakout (Antiochos et al. 1999) and the normal/inverse prominence configuration (Low & Zhang 2002) models are the most plausible ones. In the flux cancellation model, a flux rope is formed as a consequence of converging flows at a neutral line. In the breakout model, the flux rope forms as a consequence of a specific reconnection process, which requires a quadrupolar configuration. Finally, the Low and Zhang model supposes the pre-existence of a flux rope that supports a prominence in two different configurations.

The three-dimensional configuration of CMEs has been a major puzzle since their discovery, due to the two-dimensional nature of coronagraphic images. Based on the association between CMEs and prominence eruptions found by Munro et al. (1979), Trottet & MacQueen (1980) attempted to correlate the magnetic field structure of loop-like CMEs with the orientation of Hα filaments. Subsequently, CMEs were initially suggested to consist merely of planar loops. In contrast, later studies based on various approaches agreed that CMEs are certainly three-dimensional objects (Crifo et al. 1983, Fisher & Munro 1984, Webb 1988, MacQueen 1993). However, the precise three-dimensional configuration of CMEs as magnetic entities is still under debate. In this respect, further improvements have been carried out in the course of this work (see e.g., Section 3.6)

If a CME propagates in the direction of the Sun-Earth line, it will appear as a halo that surrounds the coronagraph's occulter (as already pointed out in Figure I.2). Furthermore, if it originates in the visible solar disk, the resulting event will likely hit the Earth. Primarily those events, commonly referred to as front-sided, in contrast with back-sided ones, constitute a menace for the Earth's magnetosphere and space environment. Particularly, CMEs associated with magnetic field components anti-parallel to that of the Earth's dipole field trigger intense geomagnetic storms (e.g., Webb 2002), directly visible as beautiful aurorae, and occasionally telecommunication outages, power blackouts and damage to satellites (e.g., Dyer 2002).

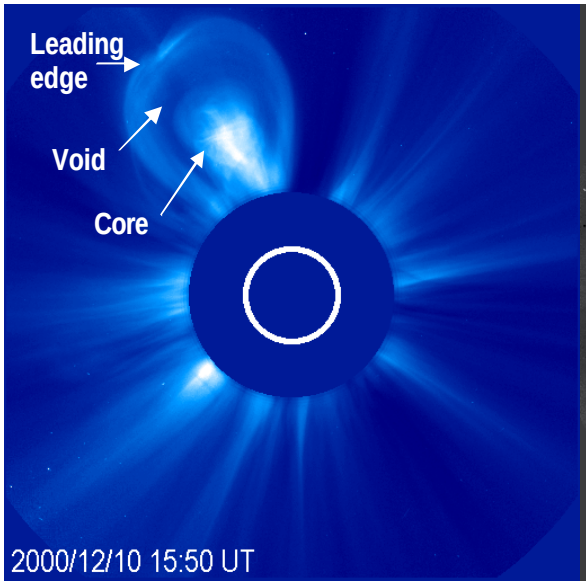

Figure 1.12. A three-part structure CME showing the characteristic bright leading edge, dark void, and bright core. This event was observed by the LASCO/C2 coronagraph on December 10, 2000.

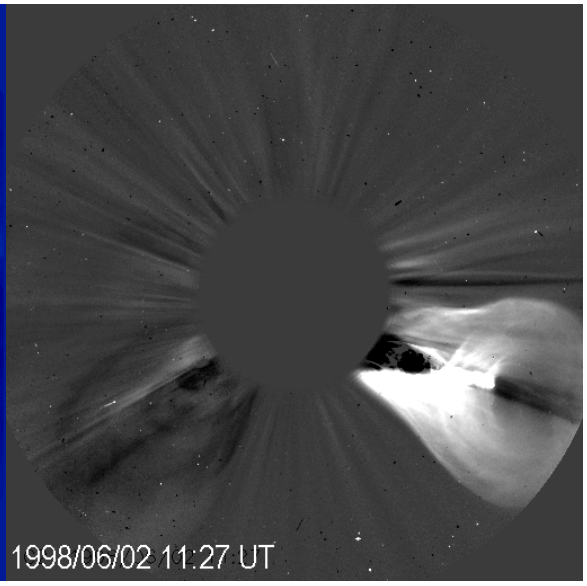

Figure 1.13. A differential image of the CME observed by LASCO/C2 on April 23, 2001. The subtracted pre-event image had been recorded at 8:32 UT on the same day. Circular features outlining the void suggest the presence of a magnetic flux rope.

1.5 The solar wind and its impact on Earth

Interplanetary space is not empty, but filled with a complex flow of charged particles emanating from the solar corona called the solar wind, in which the planets and solar system objects are continuously submerged. Because of the elevated temperatures in the corona, the thermal speeds of the particles are so high that not even the enormous solar gravity can hold them. The expanding solar wind carries with it about 10^9 kg of solar mass per second. This number seems small, when compared with the mass loss rate produced by the Sun's radiation process that reaches $5x10^9$ kg s^{-1}, but large when contrasted with the average mass loss rate due to CMEs of 10^8 kg s^{-1}.

The two main components of the solar wind are: a uniform flow of fast solar wind with an average speed of 800 km s^{-1}, and a flow of highly fluctuating slow solar wind with average speed about half of that value (see review by Schwenn 1990). The solar wind latitudinal distribution varies drastically with the solar cycle (Woch et al. 1997; McComas et al. 2003). At solar cycle minimum, the fast streams (originating from the polar coronal holes with opposite magnetic polarities in both hemispheres) are separated at equatorial latitudes by the heliospheric current sheet. The slow solar wind likely originates from the top of coronal streamers, in an intermittent fashion. Conversely, at times of solar maximum the reduction of the polar coronal holes and the redistribution of fields all over the Sun causes streams of different properties all over the Sun.

The magnetic field of the Sun, embedded in the solar wind, extends far into interplanetary space. Due to the Sun's rotation, the interplanetary magnetic field (IMF) gets winded up with the shape of an Archimedean spiral near the ecliptic plane.

Inhomogeneities in the wind flow are mainly caused by interplanetary CMEs (ICMEs) and corotating interaction regions (CIRs). The latter ones correspond to regions where high speed-solar wind streams catch up slow streams.

The basic configuration of the Earth's magnetic field resembles that of a magnetic dipole. Under the effect of the solar wind on the Earth's magnetosphere, the dayside field lines become compressed. At the same time, the nightside field lines are distorted into an extended cylinder, the magnetotail (Figure 1.14; see Treumann & Baumjohann 1997). The solar wind is deflected around the Earth's magnetosphere, and a bow shock is formed on the dayside, separating both solar wind and Earth's magnetic fields. This protecting shell shields life on Earth from hazardous energetic charged particles from space.

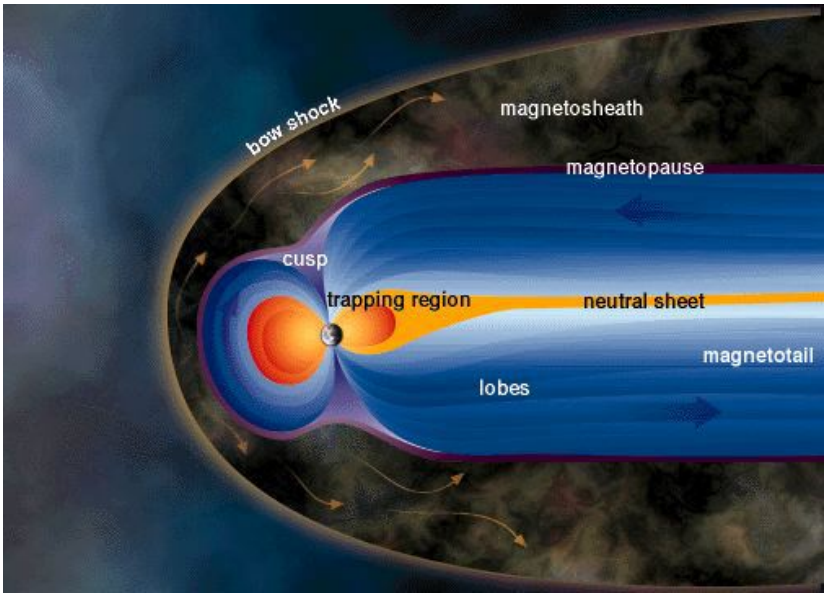

Figure 1.14. Basic structure of the Earth's magnetosphere. Credit: Windows to the Universe (*www.windows.ucar.edu*)

Southward-directed interplanetary magnetic fields carried by the solar wind couple with the northward pointing dipolar magnetic field of the Earth (Russel & McPherron 1973; Tsurutani et al. 1988, 1992; Bothmer & Schwenn 1995). In this case, geomagnetic substorms and storms can occur. During a magnetic substorm, solar wind field lines are conveyed towards the night side into the Earth's magnetotail, where lines of opposite directions reconnect (Treumann & Baumjohann 1997). As excess energy is stored in the tail, an increase of the neutral sheet current is evident. After a storage period, the magnetic tension causes a break down and the energy gained by the plasma sheet is accelerated towards the Earth and away from it, following magnetic field lines (storage and release concept; see Figure 1.15). Electrons and ions move under the effect of field gradients and magnetic curvature, enhancing the ring current, which flows from midnight to dusk. In return, the ring current produces a magnetic field that opposes to the dipolar one of the Earth. The whole process begins with a sudden jump in the magnetic field, followed by a main phase characterized by reconnection of fields and concluding with a recovery phase in which ring current particles are dissipated (Daglis et al. 1999). For an intense magnetic storm to take place, it is required that the external southward field has a value greater than 10 nT, for a sufficiently long period of at least 3 hours (Gonzalez & Tsurutani 1987). During a magnetic storm, the conductivity in polar regions is increased due to precipitation of charged particles, allowing a flow of currents that excite atoms of mainly oxygen and nitrogen. It is in their de-excitation that they glow and produce the beautiful aurorae.

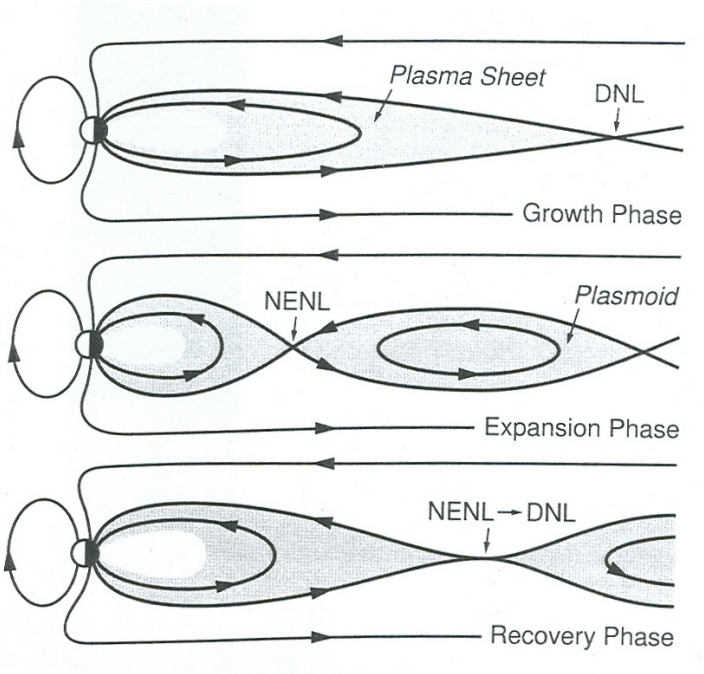

Figure 1.15. Three phases of a substorm as sketched by Treumann & Baumjohann (1997). NENL stands for near-Earth neutral line, while DNL denotes the distant neutral line.

Suggested reading

Aschwanden, M. J. 2004, Physics of the Solar Corona, Springer Verlag & Praxis Publishing, UK

Harra, L. K., Mason, K. O. 2004, Space Science, Imperial College Press, UK

Lang, K. R. 2001, The Sun, Cambridge University Press, UK

Phillips, K. J. H. 1992, Guide to the Sun, Cambridge University Press, UK

Stix, M. 1989, The Sun – An Introduction, Springer Verlag, Germany

Treuman, R. A., Baumjohann, W. 1997, Advanced Space Plasma Physics, Imperial College Press, UK

Chapter 2 Instrumentation and Data

2.1 Introduction

The unprecedented observations provided by instruments on the SOHO spacecraft served as a starting point for this study. Observations of white-light CMEs made by the Large Angle Spectroscopic Coronagraph (LASCO) onboard SOHO were essential to improve the present knowledge regarding the 3D structure of CMEs. Data from the Extreme-Ultraviolet Imaging Telescope (EIT) aboard SOHO provide high cadence observations of dynamic processes in the low corona, and were used to investigate the CMEs' source regions. Measurements made by SOHO's Michelson Doppler Imager (MDI) were used to locate the photospheric source regions of CMEs and to investigate their field structure. Ground-based observations from the Observatory of Meudon and the Big Bear Solar Observatory gave information on the structure and location of Hα filaments. Additionally, He 10830 Å* data from the National Solar Observatory/Kitt Peak provided information about the spatial distribution and size of coronal holes.

The second part of this chapter (Section 2.4) consists of the various data formats and processing methods applied to them. These are introduced, according to the type of analysis carried out, before entering into the data analyses addressed in the following chapters. The processing of LASCO C2 data was especially crucial, since high-quality images are required in order to analyze the fine structure within CMEs. For the identification of the CME source regions, we have employed data provided by the EIT and MDI instruments onboard SOHO, in combination with Hα images from the Meudon and Big Bear observatories. Halo CMEs were mainly identified and analyzed on the basis of LASCO C3 images, with few exceptions of events fitted in LASCO C2 data.

2.2 The SOHO Mission

The Solar and Heliospheric Observatory (SOHO) is a joint effort between the European Space Agency (ESA) and the National Aeronautics and Space Administration (NASA), in the context of the Solar Terrestrial Science Program (STSP) and the International Solar Terrestrial Physics program (ISTP; Fleck et al. 1995). This space mission was first proposed as a comprehensive high-resolution spectroscopic investigation of the upper solar atmosphere, in November 1982. In early 1983 it was also proposed to include helioseismology instruments in the payload (Malinovsky-Arduini & Froehlich 1984). The phase A study was followed by the calling for "Proposals for Investigations", in March 1987. One year later, the composition of the payload

* The units Å and nm are used intermittently throughout this work, according to the general terminology employed for each spectral line.

was announced. On December 1989 started the industrial definition phase (Phase B), followed by the industrial development phase (Phase C/D) in 1991. The structural model (SM) and the engineering model (EM) programs were finished in 1993 and 1994 respectively. The flight models (FM) of the instruments were assembled, integrated and validated (AIV) in the flight model spacecraft between late 1993 and mid 1995, which was shipped from Toulouse, France, to Kennedy Space Center in August 1995, for the launch campaign. ESA was responsible for the development of the spacecraft, while NASA was responsible for the launch and for the operations. The spacecraft was launched on December 2, 1995 and placed in a halo orbit around the Sun-Earth L1 Lagrangian point, allowing for the first time a continuous monitoring of our star, 24 hours a day. The positioning trajectory of the spacecraft after launch and the halo orbit it follows are sketched in Figure 2.1.

The main scientific goal of the mission is to understand better the structure and dynamics of the solar interior by means of helioseismology, the physical processes that form and heat the Sun´s corona, and the solar wind and its origin. The payload of the SOHO spacecraft comprises 12 instruments that complement each other in an exceptional way to investigate the Sun at various depths and heights, and its impact on the interplanetary medium. The experiments can be classified in three categories depending on their application: the helioseismology instruments GOLF (Global Oscillations at Low Frequencies), VIRGO (Variability of Solar Irradiance and Gravity Oscillations) and MDI/SOI (Michelson Doppler Imager/Solar Oscillations Investigation); the solar atmosphere remote sensing instruments SUMER (Solar Ultraviolet Measurements of Emitted Radiation), CDS (Coronal Diagnostic Spectrometer), EIT (Extreme ultraviolet Imaging Telescope), UVCS (Ultraviolet Coronagraph Spectrometer), LASCO (Large Angle and Spectroscopic Coronagraph), and SWAN (Solar Wind Anisotropies); and the solar wind 'in situ' instruments CELIAS (Charge, Element, and Isotope Analysis System), COSTEP (Comprehensive Suprathermal and Energetic Particle Analyzer) and ERNE (Energetic and Relativistic Nuclei and Electron experiment). The simultaneous and continuous operation of these instruments is what allows the achievement of the SOHO's mission objectives.

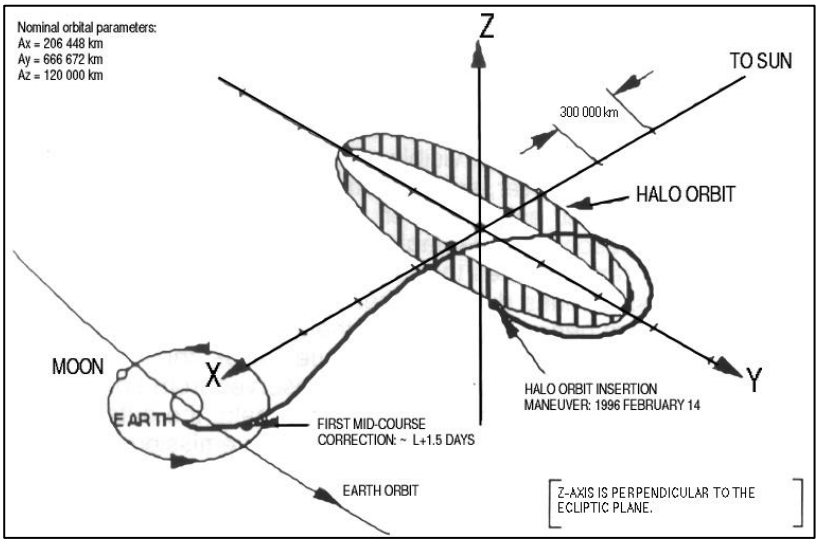

Figure 2.1. Scheme of the SOHO transfer and halo orbits. Courtesy of SOHO (ESA and NASA, *http://sohowww.nascom.-nasa.gov/*)

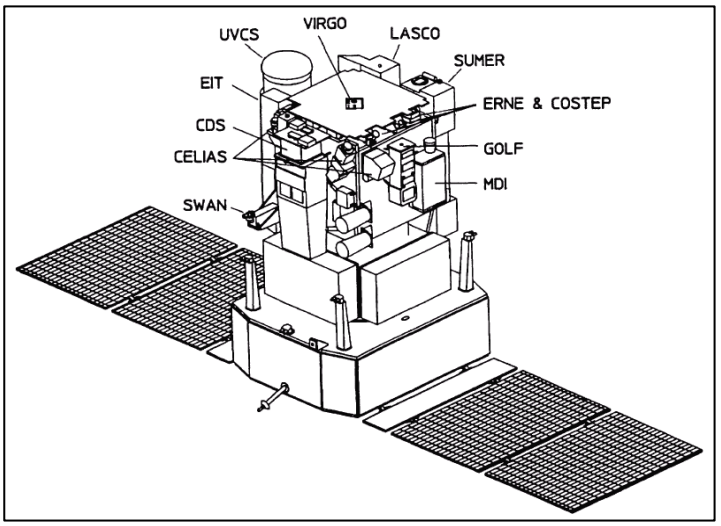

Figure 2.2. Schematic of the SOHO spacecraft and its payload. Adapted from Domingo et al. (1995).

The SOHO satellite is composed of two main elements, the Service Module (SVM) and the Payload Module (PM), which together weigh 1850 kg. The solar panels produce ~1400 W of power, out of which the payload consumes between 440 and 625 W. The continuous scientific data rate in normal mode is 40 kbits/s, while the telemetry rate ranges from 1.4 kbits/s (low) to 245.8 kbits/s (high). The telemetry is received by NASA's Deep Space Network (DSN), with stations in Canberra, Madrid and Goldstone. The Experiment Operations Facility (EOF) at NASA's Goddard Space Flight Center (GSFC) receives the telemetry data and takes care of the planning, coordination and operation of the spacecraft and payload. The science and data analysis take place at the Experiment Analysis Facility (EAF) at GSFC. The SOHO Data System provides access, visualization and analysis tools for the solar data electronically available. The standard format of SOHO data is Flexible Image Transport System (FITS).
Although planned for a lifetime of 2 years and equipped with enough consumables for 6 years, the SOHO spacecraft has degraded less than expected. Due to the enormous success of the mission it has been twice extended. Currently, it is scheduled to remain in service at least until 2007, so that SOHO would cover an entire 11-year solar cycle. Further information may be found at *http://www.esa.int/sci_mediacentre/soho_factsheet.html* and in Domingo et al. (1995).

2.2.1 LASCO Coronagraphs

The Large Angle Spectroscopic Coronagraph (LASCO) consists of a set of three coronagraphs that complement each other to observe the solar corona at different distances from the Sun (Brueckner et al. 1995). C1 is the coronagraph that observes the innermost corona, with a field of view (FOV) of 1.1 to 3 $R_{\odot}$. The basic structure of the C1 coronagraph resembles that of a Lyot coronagraph, illustrated in Figure 2.3. The light that crosses the aperture A0 is focused by the objective lens O1 in the field lens O2, in such a way that the image of the Sun coincides with the occulter D1 (a highly reflecting cone). The diffraction pattern created in A0 is projected by O2 on the Lyot stop A1, thus eliminating the stray light caused by aperture diffraction. The Lyot spot D2 blocks the spurious image caused by multiple interreflections in O1. Thanks to the presence of the Lyot stop and the Lyot spot, an internally occulted coronagraph eliminates most of the stray light. The coronal image will be finally projected on the focal plane F via the lens O3. In C1, a tunable Fabry-Perot interferometer allows the selection of 5 spectral regions with a

resolution of 0.07 nm, by means of a broadband blocking filter 5 nm wide. The measured spectral lines are Fe XIV (530.3 nm), Fe X (637.4 nm), Ca XV (564.9 nm), Na I (589.0 nm), and Hα (656.2 nm) (Brueckner et al. 1995; Howard et al. 1997). After the loss of contact with SOHO in June 24, 1998 and all the recovery activities that ended in November 5, 1998 (Vandenbussche 1999), the Fabry-Perot interferometer of LASCO/C1 was unfortunately damaged.

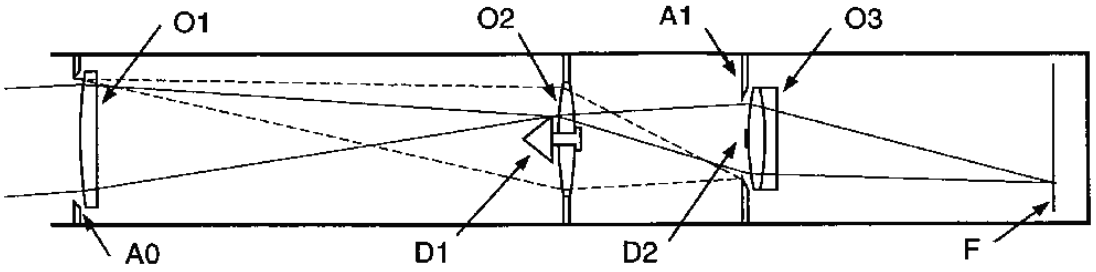

Figure 2.3. Optical components and light paths in a Lyot coronagraph like LASCO/C1. The letter *O* stands for objective lens, *A* for stop, *D* for occulter and *F* for focal plane. Solid lines represent light paths from the coronal image, dashed lines from stray light. Adapted from Brueckner et al. (1995).

The remaining coronagraphs C2 and C3 are both externally occulted and measure broadband (100 nm passband) visible photospheric light that is scattered by the free electrons in the solar corona. The major disadvantage of externally occulted coronagraphs is the poor spatial resolution near the edges of the occulter, i.e. in the inner part of the FOV, due to vignetting (the external occulter obscures partially the aperture). Additionally, the external FOV is limited by the effective aperture of the objective lens. On the other hand, the great advantage of the external occulter is that it reduces radically the levels of stray scattered light, needed to image the extremely dim corona at larger distances from the Sun.

A sketch showing the principle of such externally occulted coronagraphs is displayed in Figure 2.4, illustrating the paths of the coronal image (top) and of the stray light (bottom). At the entrance aperture A1, the light from the solar disk is suppressed by means of the external occulter D1. The objective lens O1 focuses the light in the field lens O2 and the internal occulter D2, passing through the field stop which determines the external field of view. D2 eliminates residual diffracted light from the external occulter. The coronal image is collimated by O2 against the Lyot stop A3, which cuts off diffracted light originated in A1. The remaining coronal light falls on the relay lens O3, which pictures it onto the focal plane F, where a CCD camera captures the image. Alternative colour and linear polarizing filters may be additionally selected before the capturing stage. The fields of view of C2 and C3 extend from 1.7 to 6 $R_\odot$ and from 3.7 to 32 $R_\odot$ respectively (although limited by the CCD to 30 $R_\odot$ at the equator and poles). The three LASCO cameras record their images in identical way using CCDs of 1024×1024 pixels, and achieving pixel to pixel resolutions of 11.2, 22.4 and 112 arc sec for C1, C2 and C3 correspondingly.

Altogether the LASCO package offers significant improvements with respect to previous instruments of its kind: the increased field of view, the extremely low stray light level of the externally occulted coronagraphs, the sensitivity provided by the combination of great dynamic range of the CCDs (Charged Coupled Device) and the low system noise of the cameras (Howard et al. 1997), and the long series of almost uninterrupted observations through several years. Further details about the LASCO experiment can be found in Brueckner et al. 1995.

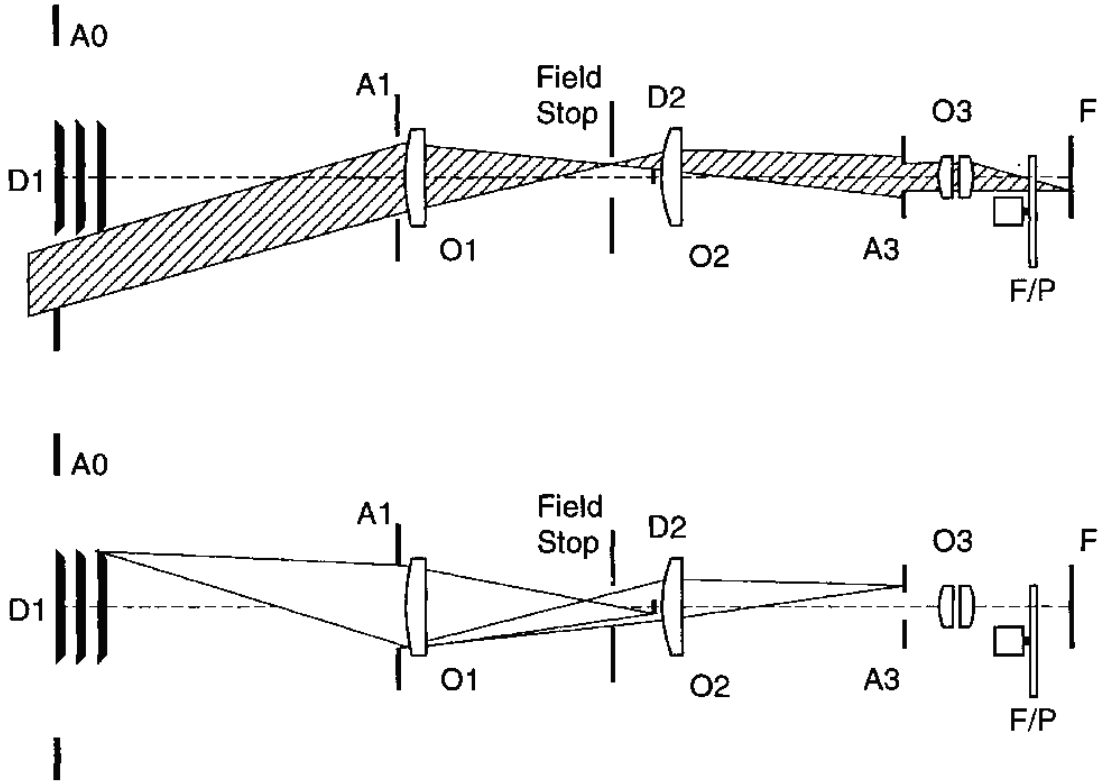

Figure 2.4. Main optical components and light paths of an externally occulted coronagraph as LASCO/C2 and C3. The letter O stands for lens, A for stop, D for occulter, F for focal plane, and F/P for the wheel with colour and linear polarizing filters. Top: light paths from the coronal image. Bottom: stray light paths. Adapted from Brueckner et al. (1995).

2.2.2 EIT

The Extreme-Ultraviolet Imaging Telescope (EIT) observes the solar corona and transition region, on the solar disk and up to a distance of 1.5 $R_{\odot}$. It consists of a modified Ritchey-Chretien telescope that uses the technique of EUV normal incidence multilayer coatings to isolate the emissions from narrow frequency ranges (Delaboudinière et al. 1995). Both of the telescope mirrors, primary and secondary, are divided into 4 quadrants, whose coatings are tuned to different wavelength bands. A schematic view of the EIT instrument is displayed in Figure 2.5, showing its principal elements. After the main door, the sunlight crosses a heat-rejection filter at the entrance aperture. The image selected via the rotating mask is focused on a special CCD for EUV wavelengths, cooled down to -80°C by a cold finger attached to a radiator. In between, a filter wheel allows the selection between an open position, long-wavelength blocking filters, or opaque aluminium filters that block the upper and lower third of the solar image. The vacuum vessel assures cleanliness and acoustical stillness.

The four multilayer coatings present at the rotating mask are related with narrow characteristic temperature regimes of the solar corona: He II **303.7** Å (8 x 10^4 K) and Si XI 303.3 Å (1 MK), Fe IX **171** Å and Fe X 174.5 Å (1.1 MK), Fe XII 192.3, 193.5 and **195.1** Å (1.5 MK), and Fe XV **284.1** Å (2 MK)* (Thompson et al. 1998). A rotating mask selects the quadrant to be illuminated by the Sun, whose produced image is focused on a CCD camera of 1024×1024 pixels, equivalent

* The boldface values correspond to the dominant emission lines.

to 44.2×44.2 arc min. The pixel size is 2.59 arc sec, with what the spatial resolution is of almost 5 arc sec.

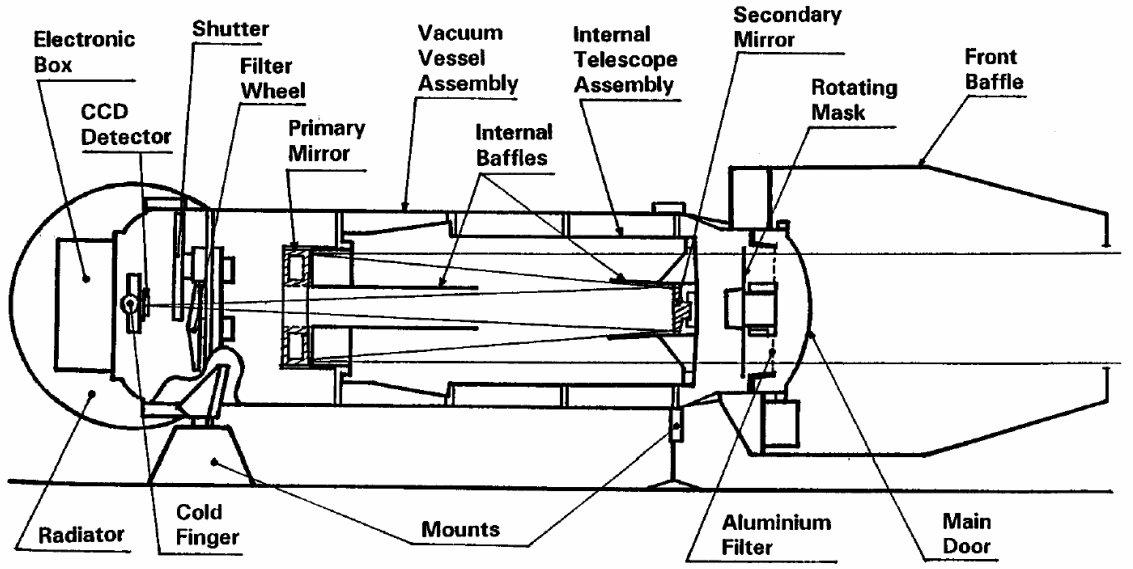

Figure 2.5. Schematic view of the EIT instrument and its main components. Adapted from Delaboudinière et al. (1995).

The images obtained in the position of the He II coatings are aimed to observe the chromospheric and transition region network structure. The bright network elements are seen right through closed loop structures, and coronal holes are marked by a reduction of elements. Prominences and eruptive prominences are best observed in this channel. The Fe IX and X lines intend to examine the boundary between corona and transition region, as well as structures inside coronal holes. These images are less structured than the subsequently described. Images in the Fe XII line display mostly the closed field regions of the quiet corona, i.e. all but the hottest active region loops are visible in this wavelength. Because of its bright contrast, high sensitivity to quiet Sun structures and cadence, this is the channel most utilized in this work to follow the evolution of the source regions associated with the analyzed CMEs. Fe XV images show hot loops characteristic of active regions (Moses et al. 1997). Absorption of coronal emission is also noticed in the three coronal channels in the locations of prominences and macrospicules. The mechanism of this absorption is probably photoionization of He I and/or He II (Dere et al. 1999).

2.2.3 MDI

The Michelson Doppler Imager (MDI) is the instrument of the Solar Oscillations Investigation (SOI) to investigate the solar interior by measuring the photospheric manifestations of solar oscillations (Scherrer et al. 1995). It provides high resolution images of the line of sight velocity, line intensity, continuum intensity, longitudinal magnetic field components and limb position, by means of sampling the Ni I 676.8 nm line with a wide-field tunable Michelson interferometer. The basic layout of the MDI instrument is shown in Figure 2.6. The green section corresponds to the telescope, filter wheels and the image stabilization system. The polarization analyzer wheel converts the polarized light into vertically polarized light. The ISS directs this component through the instrument, while an orthogonal component is sent to the bi-cell limb sensors. The blue elements correspond to the lasting optics and the filters, and are housed in a controlled oven.

The tuning waveplates are rotated to adjust the Michelson interferometers. Red parts represent the beam distributing system and the CCD camera. The CCD is 1024×1024 pixels large, which derives in a pixel size of 2 arc sec in full disk mode and 0.65 arc sec in high-resolution mode. These two spatial resolutions are selected using the shutter. Further information on the MDI experiment can be found in Scherrer et al. (1995).

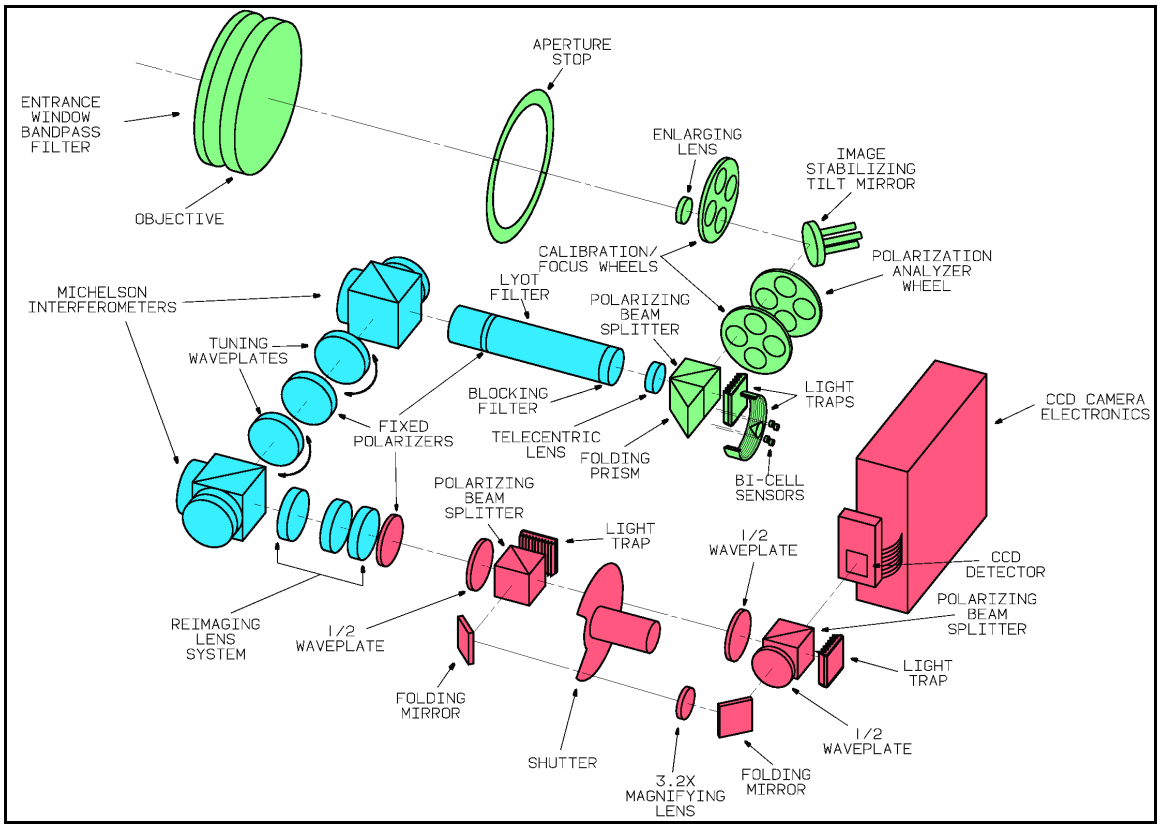

Figure 2.6. Main optical components and light paths of the MDI instrument. Adapted from *http://soi.stanford.edu/*, courtesy of the SOHO/MDI Consortium (ESA and NASA).

2.3 Ground-based instruments

2.3.1 Meudon Spectroheliograph

The spectroheliograph at the Meudon Observatory records images of the solar photosphere (blue wing of the CaII K 393.4 nm line or K1v) and chromosphere (centre of the CaII K 393.4 nm line or K3, and Hα 656.3 nm). The size of the image is approximately 1024×1024 pixels, with a pixel size of 2 arc sec. A set of images in each wavelength, plus an extra long exposure in the K3 line for prominence studies, are normally produced per day. These daily sets recorded since the year 1996 are available at the BASS 2000 database at *http://bass2000.obspm.fr*, in fits and gif format. The spectroheliograph is part of the Global High Resolution Hα Network (*http://www.bbso.njit.edu/Research/Halpha/*), whose databases were occasionally consulted as well.

2.3.2 Big Bear 20-cm Refractor

To ensure better temporal coverage in the Hα line, images captured by the 20-cm refractor telescope at the Big Bear Solar Observatory (*www.bbso.njit.edu*) were also analyzed. The observatory is located in the middle of Big Bear Lake to reduce the image distortion that occurs when the Sun heats the ground and produces convection in the air just above the ground. The 20 cm refractor monitors the full Sun with a pixel to pixel resolution of 2" and a cadence of about 1 image per minute. The full disk images are recorded by a 2048×2048 CCD camera and later enhanced through image processing techniques. The full disk telescope is also part of the global Hα network, together with the observatories of Meudon, Kanzelhöhe, Catania, Yunnan and Huairou *http://www.bbso.njit.edu/Research/Halpha/.*

2.3.3 NSO/KP Spectromagnetograph

The Spectromagnetograph on the vacuum telescope at the National Solar Observatory/Kitt Peak (*www.noao.edu/kpno*) provides photospheric magnetograms in the line of Fe I (868.8 nm) and cromospheric spectroheliograms in the line of He I (10830 Å). This ground based facility observed for the last time on 21st September 2003, and is now being replaced by the new vector spectromagnetograph, part of the facilities of SOLIS (acronym for Synoptic Optical Long-term Investigations of the Sun). The spectromagnetograph on the vacuum telescope observed the full disk magnetic field, as well as coronal holes directly on the solar disk (Jones et al. 1992). Coronal holes and their boundaries are identifiable as bright areas due to reduced chromospheric absorption in the line of 10830 Å. The synoptic rotation maps of coronal holes employed in this work were assembled from daily full disk spectroheliograms at 10830 Å in conjunction with the related magnetogram, since another distinctive characteristic of coronal holes is the unipolarity of magnetic fields within the area of the coronal holes (Harvey & Recely 2002).

2.4 Data formats and processing

2.4.1 Structured CMEs

Because of the cadence and spatial resolution of LASCO C2, fine details in white light CMEs could be resolved. The identified set of structured CMEs (see Table 1) is based on the systematic investigation of daily C2 half-resolution (512×512 pix) MPEG movie files, available at *http://star.mpae.gwdg.de/daily_mpg*. If the inspection of a single movie takes ~5 minutes, the total investigation time of the whole dataset amounts ~213 hours (365 × 7 = 2555 daily MPEG movies).

FITS full resolution (1024×1024 pix) images were processed and analyzed only for those events for which an associated source region could be identified. FITS stands for Flexible Image Transport System and is employed as a standard format for SOHO data exchange. The first portion of the file consists of a header, with relevant information regarding the image properties. The employed files consist of FITS level 0.5, available through the LASCO online database at *http://lasco-www.nrl.navy.mil/cgi-bin/lwdb/lasco/images/form.* Level 0.5 images arise after the raw data have been separated from the telemetry stream and after they are oriented in such a way that the solar north is at the top of the image. They are in units of digital numbers (DN) or counts. Further processing as been applied to the level 0.5 FITS images, with aid of the LASCO

Image Display program V3.0, written in IDL (Interactive Data Language) by B. Podlipnik. These actions consisted of:

- Camera bias correction: necessary to correct the effect of the polarization current, which increases with time.
- Exposure time normalization: the counts in each pixel of the CCD are normalized by dividing them by the exposure time. The latter is taken from the image header.
- Background subtraction: After the subtraction of background models, most of the static K-corona, F-corona and stray light is removed. The background models are generated by taking the minimum of daily median images every 4 weeks, and are available at *http://lasco-www.nrl.navy.mil/retrieve/monthly*.
- Cosmic rays removal: present due to the interaction of cosmic rays with the CCD, cosmic rays were partially removed by means of a median filter technique.
- Layout enhancements: application of an occulter mask, use of blue colour palette, and insertion of the solar grid and date & time.

After the additional processing, the images were saved in GIF* format, which uses a non-lossy algorithm of compression. A typical processed LASCO C2 image is presented in Figure 2.7 a.
A very used technique was that of running difference images, in which each frame has the previous frame subtracted from it. Normally they are presented in grey-scale. It is very useful to perceive changes within a sequence of images, i.e. areas where the density has increase appear bright, while areas in which the density has diminished appear dark. A variation of the running difference technique is the simple subtraction of the same single image (for instance, previous to the event to be analyzed) to all the subsequent frames of the sequence. An example of a LASCO C2 differential image is presented in Figure 2.7 b.

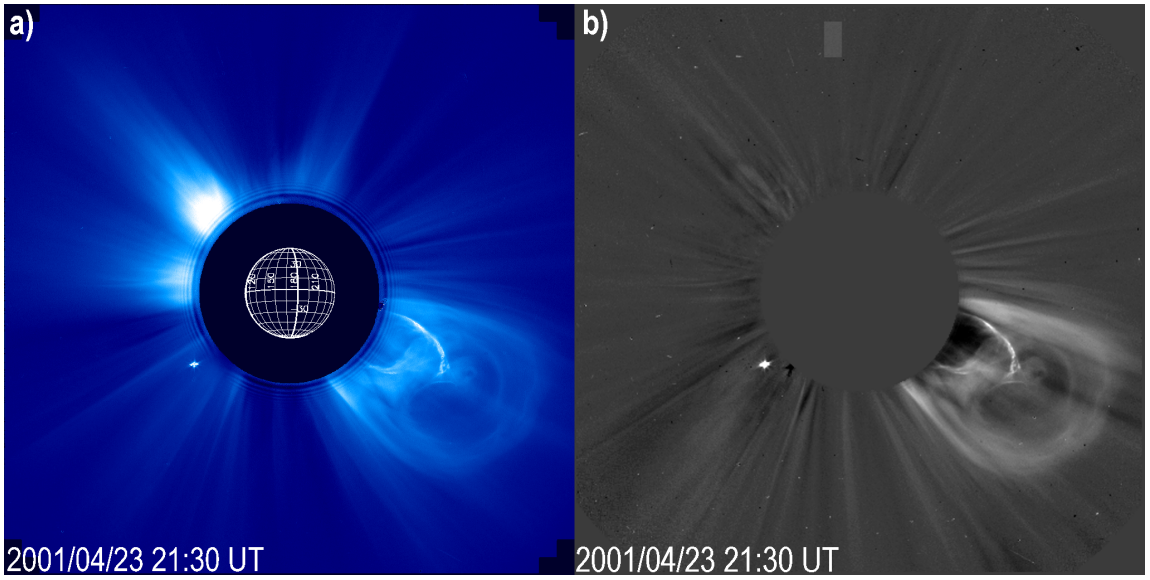

Figure 2.7. a) A LASCO C2 level 0.5 image after additional processing. b) A LASCO C2 differential image, from which a pre-event image at 18:11 UT has been subtracted.

Main information regarding the studied CME events has been obtained from the Preliminary CME Lists at *http://lasco-www.nrl.navy.mil/cmelist.html* and from the CME Catalogues developed by C. St. Cyr (Jan 1996-June 1998; *ftp://lasco6.nascom.nasa.gov/pub/lasco/status/-*

* GIF (Graphic Interchange Format) is specially appropriate for imageswith shadings of the same colour.

Version2_CME_Lists/) and by S. Yashiro (Jan 1996-Dec 2002; *http://cdaw.gsfc.nasa.gov/-CME_list/*). Major data gaps occurred during the periods Jun/25/1998-Oct/14/1998 and Dec/21/1998-Feb/02/1999.

Because of the few CME events selected during the period of operation of C1, they were not taken into account for statistical purposes. C1 data were of important help to observe CME deflections studied in Subsection 3.5.4. In these cases, movies in MVI format (addressed in the next Subsection) were consulted.

2.4.2 Source regions of the Structured CMEs

In order to identify the source regions associated with the selected structured CMEs (see Subsection 3.2), images of the low corona captured by the EIT instrument were inspected. For further analyses of the properties of the identified source regions, Hα and MDI data were consulted.

The examination of EIT 195 Å images was carried out on the basis of movies in MVI format, available at the FTP site of NRL (Naval Research Lab). A single MVI file contains all the information necessary to display the time-lapsed movie. It has been written in IDL and is intended to be played by an IDL procedure. The file consists of three areas, a file header, a series of image headers, and then the byte scaled image arrays. All of the images have the same dimensions of 512×512 pix, i.e. they have been compressed to half of the resolution. Although the frames in MVI movies are half of the original size, the quality is notable when compared with MPEG movies. By means of an IDL procedure, the MVI file can be played as a running difference movie, based on the same concept introduced in the previous section. The desired frames can be saved in various image formats, e.g., PNG, TIFF and FTS. Figure 2.8 presents snapshots of the same erupting prominence. While a) consists of an absolute EIT 195 Å image, b) is a running difference image, resulting from the subtraction between the original image and the previous frame (captured 12 minutes earlier). There, the increased contrast of the rising prominence on the northwest limb becomes evident.

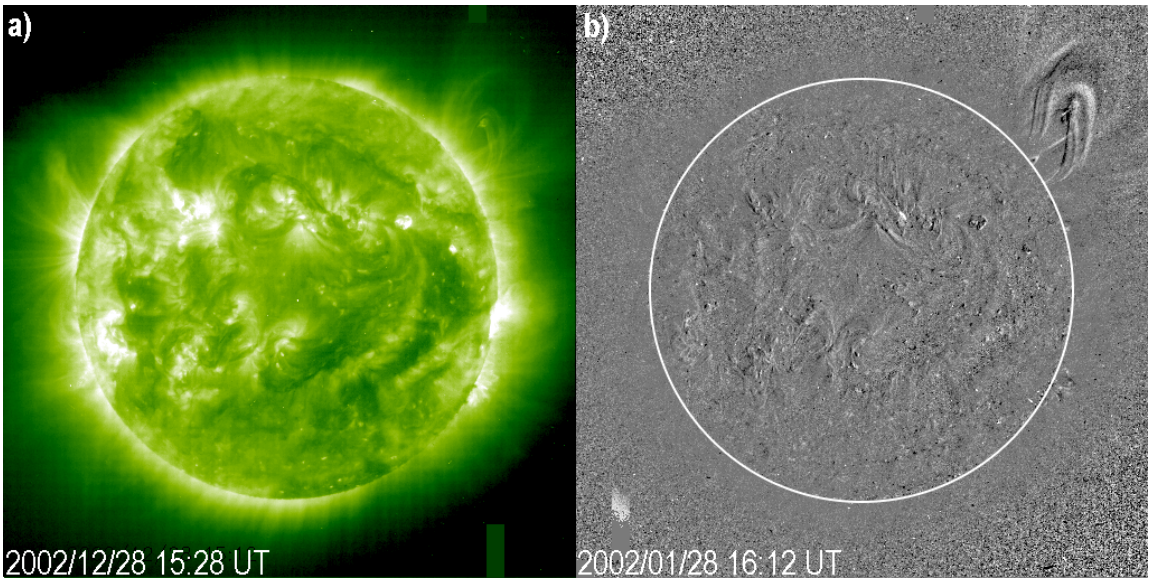

Figure 2.8. Frames taken from an MVI movie, showing a prominence eruption associated with a structured CME. a) Absolute image. b) running difference image, captured 44 minutes later.

Associations of CMEs with disappearing filaments and prominence eruptions involved the investigation of Hα and CaII K (K3) images respectively. The observatory from Meudon provides both types of images, with a size of 1024×1024 pix. Images in the Hα line at higher resolution (2048×2048 pix) are achieved by The Big Bear Solar Observatory. The data employed from Meudon Observatory was in GIF format, while those from Big Bear were in JPEG and FITS.

The heliographic locations of the source regions where determined with the aid of the IDL procedure IMAGE_TOOL. The procedure opens and displays FITS files, allowing the user to find the coordinates of the required features by clicking on them. Afterwards, the coordinates were transformed to the Carrington system, in order to trace back the source region features to MDI synoptic charts of the photospheric magnetic field. MDI synoptic charts are magnetic maps of the Sun for a full solar rotation, built by putting side by side vertical bands from daily full-disk MDI magnetograms. The vertical bands are generally extracted from heliographic longitudes of 0°, ±30° and ±60°. The size of the MDI synoptic charts in their GIF version is of 1000×410 pix.

The most relevant images that describe each event where put together, for each structured CME with identified source region. This facilitated enormously the posterior analyses and comparisons between events. The event on February 26, 2000 is displayed in Figure 2.9 as an example.

2.4.3 Halo CMEs

To study the geometrical properties of halo CMEs (see Chapter 4), LASCO/C3 data were particularly important. Since even the most obvious halos appear quite faint in LASCO images, the running difference technique has been especially useful. The selection of halo events from the NRL halo database at *ftp://ares.nrl.navy.mil/pub/lasco/halo* (see Section 4.3) was carried out in a first approximation on daily MPEGs. For the selected halo CMEs, the movies in MVI format were played as a running difference sequence. The frames of these MVIs were saved in FITS format. (with a size of 512×512 pix). The determination of the coordinates of the 5 points required for the fitting of the ellipse (see Subsection 4.2.2; see Figure 4.5) was carried out with help of the IMAGE_TOOL procedure. These determined coordinates were measured in terms of position angle and solar radii.

The identification of the source regions associated with the halo CMEs, as well as the determination of their coordinates, has been performed through the same method as for the structured CMEs.

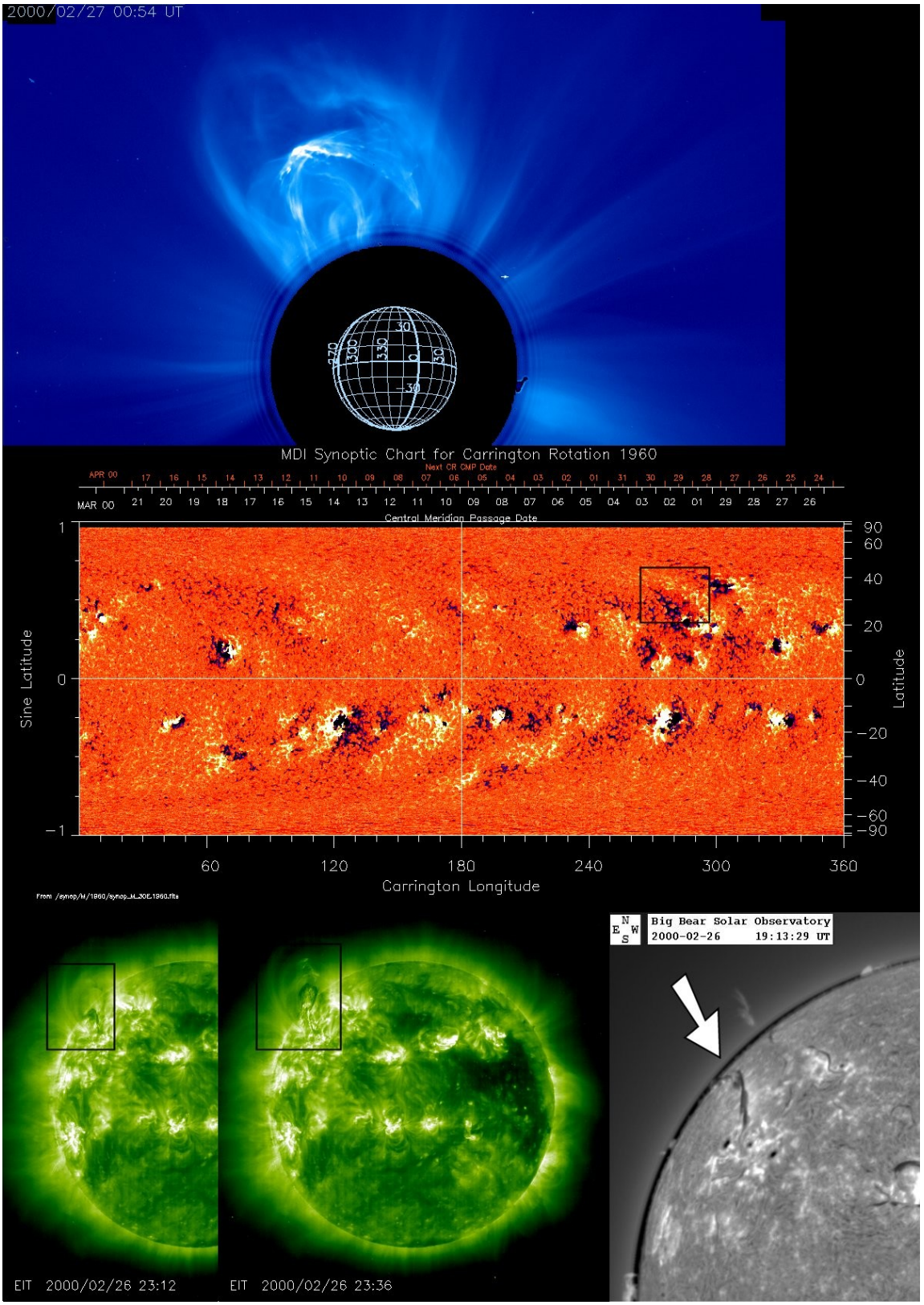

Figure 2.9. An example of a composite image of the event on February 26, 2000. Top: LASCO C2 image of the CME, here cropped to make good use of space. Centre: MDI Synoptic Chart, where the magnetic counterpart of the associated source region is enclosed in the square. Bottom: Left: Associated source region in the low corona, captured by EIT 195 Å. Right: Big Bear Hα image of the NE quadrant, showing the associated filament prior to its eruption.

Chapter 3 Analysis of structured CMEs

3.1 Introduction

From a survey of SOHO/LASCO C2 observations taken from 1996 until the end of 2002, a set of 276 structured CMEs was compiled, in order to infer observational properties that help to resolve their origin, magnetic nature, and three-dimensional configuration. The selection process was carried out based on the definition of structured CME introduced in Section 3.2. Out of the 276 selected structured events, their low coronal and underlying photospheric source regions could be identified through the analysis of SOHO/EIT and MDI as well as ground-based Hα data. Several basic properties of the structured CMEs and their source regions are examined, and analyzed during the present solar cycle. This chapter is founded on the results published in Cremades & Bothmer (2004) and Cremades et al. (2005). It concludes with the deduction of a basic scheme that describes the 3D configuration of structured CMEs as organized along an axial direction, in a cylindrical fashion.

3.2 Selection of events

The unprecedented coronal images provided by the LASCO coronagraphs onboard SOHO serve as the starting point for this work, due to their high cadence and improved spatial resolution. LASCO observations of CMEs taken since SOHO's launch (e.g., Howard et al. 1997; St. Cyr et al. 2000; Gopalswamy et al. 2003) constitute a unique dataset to study whether the white-light observations reveal the magnetic structure of CMEs, and might be used to infer their 3D nature. With this purpose in mind, a subset of "structured" CMEs has been selected for analysis, which exhibited discernable white-light features, expected to be suggestive of their internal magnetic field configuration and possible 3D structure.

We define a "structured" CME event as *an outward moving white-light feature in the field of view of LASCO/C2, that reveals inherent fine structure discernable from the ambient corona, and which develops in the field of view of C2 as part of the entire white-light feature during its outward motion.* Based on this definition, structured CMEs were identified from the full LASCO/C2 dataset within the period January 1996 to December 2002. The June 1998 CME described in Plunkett et al. (2000) and in Srivastava et al. (2000) can be considered as an archetype event (see Figure 1.13), while halo and narrow CMEs (see, e.g., Yashiro et al. 2003) as well as faint ones typically represent counterexamples of structured CMEs. Figure 3.1 shows two examples of structured CMEs identified in the LASCO dataset in comparison with a CME that is lacking clearly discernable internal white-light structure.

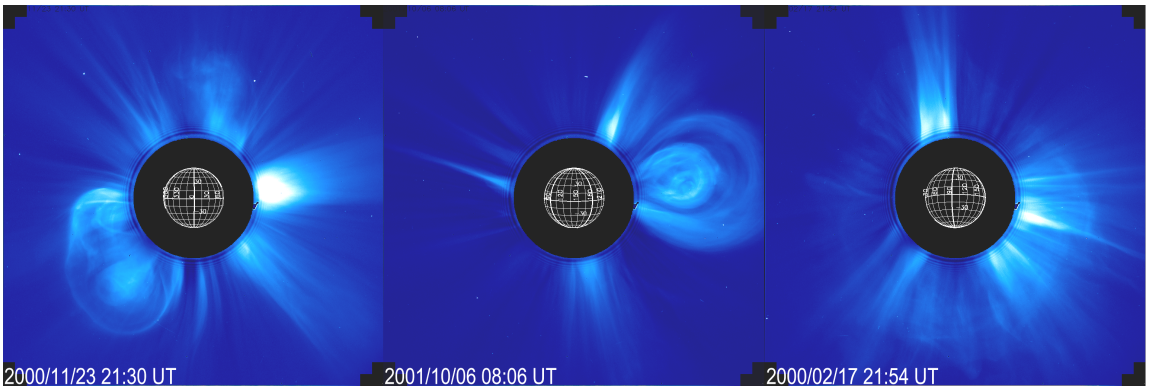

Figure 3.1. Two structured CME events (left and centre) and an unstructured one, in this case a halo CME, as observed by the LASCO C2 coronagraph.

The search of structured CME events was carried out on the basis of daily C2 half-resolution (512×512 pix) MPEG movie files, available at *http://star.mpae.gwdg.de/daily_mpg/*. Altogether, 276 structured events were selected and compiled in an extensive spreadsheet table. Table 1 presents only the 124 cases for which relevant information about the source regions could be deduced[*], and which are of major importance for this study. This subset of events has been carefully analyzed in FITS full resolution images (see Subsection 2.4.1).

Table 1. Main properties of the Structured CME events selected during the period Jan. 1996 – Dec 2002 (columns 1 to 5), and those of their identified source regions (SRs; columns 6 to 12). Columns 13 and 14 arise from associations between CMEs and SRs.

CME					SR								
Date	Time in C2 (UT)	AW (deg)	Central PA (deg)	Speed (km/s)	Carrington Coordinates (deg)				Tilt γ from vertical (deg)	Length (deg)	Central PA (deg)	Deflect. from source δ (deg)	NL-CME agreem.*
					Θ_1	Φ_{C1}	Θ_2	Φ_{C2}					
(1)	(2)	(3)	(4)	(5)	(6)	(7)	(8)	(9)	(10)	(11)	(12)	(13)	(14)
1996 Nov 05[a]	02:35	49	271	108	-15	241	-13	239	-50	2.3	249	22.0	y
1996 Nov 28[a]	16:50	43	267	984	1	242	6	241	5	4.8	274	6.8	y
1997 Feb 07	00:30	121	247	[c]718	-25	335	-47	320	34	25.5	223	24.4	y
1997 Feb 23[a]	02:55	75	88	905	31	349	37	342	47	9.0	57	31.8	y
1997 Mar 09	04:30	66	75	[c]650	4	208	11	206	17	7.1	74	0.9	nc
1997 Apr 30	04:50	64	83	286	4	215	17	214	3	13.2	78	4.6	y
1997 May 05	06:30	41	85	[c]771	23	143	17	141	-19	5.5	69	15.8	nc
1997 Sep 09[a]	20:06	88	278	726	18	116	33	98	49	22.5	307	29.2	y
1997 Sep 20[a]	10:20	76	269	777	-16	302	-33	286	44	22.0	246	22.3	y
1997 Oct 12[b]	06:26	54	255	779	-25	349	-32	340	52	10.6	240	14.6	y
1997 Oct 16[b]	22:29	81	261	631	-25	287	-35	278	43	12.8	239	22.7	y
1997 Nov 14	10:14	78	77	1042	21	111	17	107	-39	5.7	71	5.2	nc
1997 Nov 18	08:27	49	280	444	21	240	37	213	59	28.4	300	20.0	y
1997 Dec 06	10:27	144	323	[c]567	39	295	42	276	81	14.7	333	9.7	y
1998 Feb 04[a]	17:02	84	287	[c]463	43	305	48	261	84	30.8	317	30.7	y
1998 Feb 23	02:55	59	254	[c]676	-29	30	-22	29	-9	6.7	245	8.8	nc
1998 Feb 24	07:28	38	91	[c]583	29	202	19	200	-10	10.0	66	25.3	nc
1998 Mar 23[a]	09:33	68	265	[c]636	-19	34	-27	24	50	12.6	246	19.0	cs
1998 Apr 14	05:26	56	76	[c]1179	16	290	28	283	33	13.2	66	9.7	y
1998 Apr 20[a,b]	10:07	125	264	1863	-22	31	-59	9	31	40.7	228	35.6	y
1998 Apr 23[a]	05:27	113	98	1618	-21	140	-15	137	-24	6.8	110	11.7	y
1998 May 06	08:29	87	293	1099	-20	141	-13	141	-1	6.8	254	38.9	cs
1998 May 09[a]	03:35	134	264	2331	-22	139	-14	138	-5	7.4	251	12.8	nc
1998 May 19	10:27	80	293	801	12	308	28	300	27	17.7	298	4.3	y
1998 May 27	13:45	92	267	878	16	212	22	205	50	8.5	292	25.5	nc

[*] A full version of Table 1 may be obtained at *ftp://ftp.linmpi.mpg.de/outgoing/cremades* or by request to the authors.

CME					SR								
Date	Time in C2 (UT)	AW (deg)	Central PA (deg)	Speed (km/s)	Carrington Coordinates (deg)				Tilt γ from vertical (deg)	Length (deg)	Central PA (deg)	Deflect. from source δ (deg)	NL-CME agreem.*
					Θ_1	Φ_{C1}	Θ_2	Φ_{C2}					
(1)	(2)	(3)	(4)	(5)	(6)	(7)	(8)	(9)	(10)	(11)	(12)	(13)	(14)
1998 Jun 02[a]	08:08	55	242	[c]1278	-49	198	-60	161	73	24.0	213	29.3	
1998 Jun 13	02:27	90	263	[c]678	-21	350	-29	345	35	10.0	240	22.1	nc
1998 Nov 28	06:54	102	60	[c]876	18	185	20	182	56	3.3	65	-5.3	y
1999 Mar 17	07:26	68	70	[c]600	28	158	36	149	47	11.3	57	13.0	y
1999 Mar 18	03:54	65	63	375	28	158	36	149	47	11.3	55	8.5	y
1999 Apr 22[a]	02:30	66	241	461	-16	220	-23	219	9	7.1	250	-8.4	nc
1999 May 30	11:06	84	284	[c]694	-13	34	-19	30	34	7.1	252	32.3	y
1999 Jun 02[a,b]	21:26	106	298	874	22	32	37	17	44	19.5	300	2.6	y
1999 Jun 04[a]	09:26	52	270	697	-13	34	-19	30	34	7.1	251	19.2	y
1999 Jun 10[a]	14:50	69	77	412	25	96	36	85	45	14.3	60	17.6	y
1999 Jun 11[a]	11:26	103	63	1569	32	77	45	75	8	12.4	51	12.3	y
1999 Jun 16[a]	04:54	77	60	979	27	20	37	5	56	16.9	57	2.2	y
1999 Jul 03	19:54	101	305	536	13	296	18	294	20	5.3	287	-18.5	nc
1999 Jul 25[b]	13:31	100	313	1389	35	35	43	29	40	9.1	309	-4.0	y
1999 Aug 25	11:06	43	111	[c]497	-33	182	-37	180	23	4.4	126	14.7	y
1999 Oct 13	09:50	50	12	[c]696	41	324	47	303	74	16.2	24	-12.2	y
2000 Feb 13[b]	22:06	89	227	[c]1079	-30	215	-41	205	44	13.4	233	-5.6	y
2000 Feb 26	23:54	79	14	668	24	289	37	254	70	32.6	54	-39.4	y
2000 Mar 02	13:54	77	231	835	-18	332	-25	330	20	7.4	249	-17.4	y
2000 Mar 05	16:54	55	345	846	39	270	37	256	-80	11.7	333	-11.7	y
2000 Mar 21	09:06	60	322	[c]452	33	104	44	72	71	27.1	315	-6.5	y
2000 Apr 05[b]	00:06	47	217	898	-25	276	-33	267	47	10.9	242	-25.0	nc
2000 Apr 08[b]	15:54	75	235	709	-16	233	-24	228	34	9.6	251	-16.0	y
2000 Apr 23[a]	12:54	119	280	1187	10	77	25	71	24	16.3	288	7.3	nc
2000 May 11	23:50	69	168	716	-33	44	-55	-3	65	39.3	146	-22.3	y
2000 May 15	08:50	84	59	1549	20	301	26	298	23	6.4	67	-8.6	nc
2000 Jun 02	20:30	115	77	[c]934	22	80	17	80	0	4.9	67	9.6	nc
2000 Jun 25	07:54	55	268	1617	12	265	17	253	67	12.6	286	17.7	y
2000 Jun 27	10:54	104	336	811	40	249	42	228	85	15.9	314	-22.0	y
2000 Jul 10	20:26	66	16	354	43	287	49	266	73	15.8	44	-27.2	y
2000 Jul 10	21:50	71	89	1352	17	306	17	299	-88	7.3	72	16.9	y
2000 Jul 17	08:54	120	94	[c]1060	3	240	6	231	74	9.2	89	5.2	y
2000 Aug 02[a]	17:54	88	42	[c]876	37	330	53	310	53	20.7	45	-2.6	y
2000 Aug 03[b]	08:30	78	301	896	16	120	31	106	44	19.9	293	-8.5	y
2000 Aug 28[a]	00:54	86	63	542	25	346	40	315	64	30.4	54	9.0	y
2000 Sep 04	06:06	117	318	849	12	381	34	374	18	22.9	299	-18.9	y
2000 Sep 12	11:54	181	204	1550	-13	251	-24	234	56	19.1	197	6.7	y
2000 Sep 27	20:50	77	181	571	-23	17	-37	13	15	14.9	157	-23.0	y
2000 Oct 16[a]	07:27	115	281	1336	4	257	2	254	-52	3.2	275	-6.1	nc
2000 Oct 26	16:50	91	118	359	-33	305	-25	302	-21	8.4	122	4.4	y
2000 Nov 01	16:26	137	127	801	-15	257	-16	245	85	11.6	117	-10.1	y
2000 Nov 02	16:26	105	306	[c]902	27	361	26	342	-88	17.0	297	-9.6	y
2000 Nov 04	01:50	67	228	763	-28	350	-36	313	79	32.1	235	-6.9	y
2000 Nov 08[b]	23:06	126	293	1345	19	251	25	249	25	6.2	295	1.5	y
2000 Nov 17	06:30	56	185	[c]796	-50	156	-50	117	90	24.8	211	-25.2	nc
2000 Nov 23	20:30	97	127	1198	-26	298	-38	295	12	12.5	126	-1.2	y
2000 Nov 26[b]	06:30	126	275	[c]1049	19	51	25	48	24	6.9	292	17.5	y
2000 Dec 10	03:26	53	24	655	44	118	52	54	83	42.6	33	-8.5	y
2001 Jan 07	04:06	64	304	[c]815	17	225	27	188	76	35.5	295	-8.5	y
2001 Jan 26	01:54	65	302	648	14	331	35	310	44	28.7	297	-5.2	y
2001 Jan 26	16:06	98	57	[c]996	20	186	31	173	50	16.7	59	-1.9	y
2001 Feb 02	19:54	85	62	845	17	97	22	93	38	6.9	61	0.8	y
2001 Feb 20	15:05	70	51	569	18	186	25	177	51	11.0	69	-18.2	y
2001 Feb 26[b]	18:50	86	242	[c]547	-23	278	-40	260	47	22.8	239	3.2	y
2001 Apr 01[a]	11:26	98	105	1475	-20	360	-27	357	20	8.3	116	10.8	y
2001 Apr 03	03:26	95	109	1613	-18	360	-26	357	20	8.3	111	2.3	y
2001 Apr 09	00:06	74	131	[c]1040	-24	360	-27	356	52	5.2	159	27.2	y
2001 Apr 15	14:06	94	271	1199	-25	360	-20	358	-29	5.1	248	22.9	y
2001 Apr 23[b]	19:09	69	236	[c]515	-30	249	-36	232	71	15.5	236	-0.3	y

CME					SR								
Date	Time in C2 (UT)	AW (deg)	Central PA (deg)	Speed (km/s)	Carrington Coordinates (deg)				Tilt γ from vertical (deg)	Length (deg)	Central PA (deg)	Deflect. from source δ (deg)	NL-CME agreem.*
(1)	(2)	(3)	(4)	(5)	Θ_1 (6)	Φ_{C1} (7)	Θ_2 (8)	Φ_{C2} (9)	(10)	(11)	(12)	(13)	(14)
2001 May 15[a]	18:52	68	56	1280	15	152	34	129	51	29.0	65	-9.5	y
2001 May 25	17:26	59	93	930	-7	36	-21	22	45	19.6	104	11.2	nc
2001 Jun 26[a]	12:30	83	107	997	-8	317	-17	316	5	8.5	102	-5.1	y
2001 Jul 12[b]	00:06	110	231	736	-28	272	-43	259	41	18.3	230	0.4	y
2001 Jul 23[a]	11:08	68	291	515	5	142	7	142	0	1.9	276	-15.1	y
2001 Aug 09[a]	20:30	67	118	909	-10	89	-30	65	50	29.7	110	-8.8	y
2001 Aug 19	06:06	74	285	556	27	134	28	126	79	7.3	297	11.6	y
2001 Aug 21[b]	12:06	104	231	623	-19	80	-25	68	64	12.7	237	-5.6	y
2001 Aug 24	09:26	61	121	[c]474	-21	290	-15	287	-27	7.1	114	-7.1	cs
2001 Sep 21	08:54	63	117	[c]988	-15	276	-22	272	28	7.7	113	-4.2	cs
2001 Sep 28	10:30	91	195	[c]740	-15	277	-22	270	45	9.9	226	-31.0	nc
2001 Oct 01	05:30	106	237	[c]1957	-19	292	-21	282	77	9.3	248	-11.1	y
2001 Oct 06	05:54	66	276	[c]814	13	229	11	228	-31	2.7	282	5.3	cs
2001 Oct 29	11:50	72	296	[c]731	14	285	34	262	49	29.0	294	-2.0	y
2001 Nov 01	14:30	90	127	1053	-18	80	-22	80	9	4.3	111	-15.9	y
2001 Dec 02[a]	22:06	92	263	[c]835	-8	193	-11	193	7	2.5	261	2.5	cs
2001 Dec 14[a]	09:06	107	72	1506	2	219	9	214	38	8.2	85	-13.0	nc
2001 Dec 20	00:30	69	114	[c]952	-17	208	-26	195	57	15.5	122	7.9	y
2001 Dec 28[a]	20:06	108	115	[c]2239	-17	20	-28	16	25	11.2	114	-0.9	y
2002 Jan 04	09:30	90	46	[c]708	19	338	32	314	62	25.5	62	-15.7	y
2002 Jan 24[a]	03:54	94	99	536	-20	20	-28	11	49	11.3	119	20.2	nc
2002 Feb 12	15:30	115	67	448	10	206	13	202	52	4.9	63	4.2	nc
2002 Feb 28[a,b]	00:30	97	252	541	-17	143	-28	136	34	12.2	246	6.1	y
2002 Mar 02	15:06	60	112	1131	-13	290	-35	257	56	36.9	114	2.6	y
2002 Mar 13	23:54	59	117	489	-19	143	-25	135	56	9.5	111	-5.5	cs
2002 Mar 18	02:54	166	256	989	-16	180	-2	177	-12	14.3	262	-6.4	y
2002 Apr 18[b]	16:06	69	254	804	-10	190	-21	185	24	12.0	255	-0.3	y
2002 Apr 21[b]	01:27	117	273	2460	-13	154	-28	132	56	25.5	250	22.2	y
2002 May 21	21:50	105	53	880	18	346	23	342	37	6.2	57	-4.8	y
2002 May 22[b]	00:06	87	243	1136	-14	92	-19	87	48	7.8	253	-10.0	y
2002 May 22	03:50	145	237	1494	1	84	-29	60	38	38.0	254	-16.4	y
2002 Aug 01	04:06	118	201	[c]531	-16	142	-28	141	7	11.6	150	-51.2	y
2002 Aug 13	08:54	104	46	[c]623	38	299	42	285	75	11.6	49	-3.1	y
2002 Aug 23	08:50	78	84	[c]1179	-5	157	-10	154	25	5.3	100	16.0	y
2002 Oct 13	23:54	112	91	1009	-10	194	-20	186	40	12.9	107	15.8	y
2002 Oct 15	12:54	82	187	[c]1741	-25	252	-25	198	-90	48.5	154	-33.3	y
2002 Oct 25	07:27	51	121	580	-30	71	-40	35	75	30.9	132	10.9	y
2002 Nov 19	03:06	89	20	938	28	119	34	113	44	7.8	42	-21.8	nc
2002 Nov 26	17:06	77	300	479	22	129	26	126	30	4.2	294	-5.7	y
2002 Dec 28[a]	16:30	72	308	[c]1299	27	109	35	83	72	24.0	303	-5.2	nc

* y = agreement, nc = not clear agreement, cs = compact system.

[a] Far-side events, i.e. with mean absolute heliographic longitude greater than 90°.

[b] Events with neutral lines parallel to the limb, taken into account for Figure 3.34

[c] Events for which a 2nd order fit was more appropriate for the computation of the speed.

3.3 Basic properties

Information about the selected structured CMEs, found in columns 1 to 5 of Table 1, refer to CME date and time*, angular width (AW), position angle (PA) and speed*. These essential properties are analyzed below.

* Obtained from the SOHO LASCO CME Catalog at *http://cdaw.gsfc.nasa.gov/CME list/*.

3.3.1 Rate of occurrence

A histogram showing the time distribution of the 276 selected structured CMEs* is presented in Figure 3.2. While the total height of the columns represents the amount of structured CMEs per year, the grey-shaded portion corresponds to the number of events for which the source region could be identified (124 in total). The histogram is presented together with the yearly sunspot number (dash-dotted line) and the total amount of observed CMEs per year (dotted line) for comparison. Yearly sunspot numbers were derived from the monthly values available at *http://sidc.oma.be/html/sunspot.html* (courtesy of Van der Linden and the SIDC† team), while the yearly CME rate was acquired from Gopalswamy et al. (2003). As expected from the dependence of CME rate on the sunspot number, the structured CME frequency follows as well the sunspot cycle (see Figure 1.3). Note that the subset of selected structured CMEs represents 4% of the total amount of observed CMEs (Yashiro et al. 2004), while those with identified source regions represent approximately 2%.

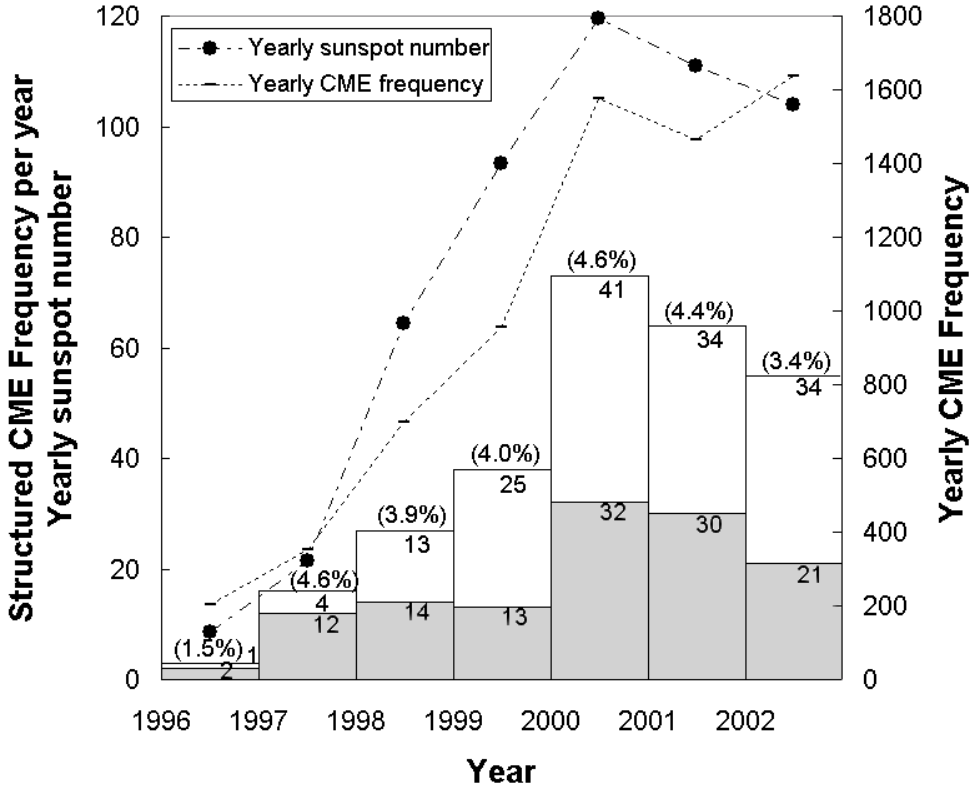

Figure 3.2. Time distribution histogram of the 276 structured CMEs (columns) in comparison with the yearly sunspot number (dash-dotted line) and the yearly CME frequency (dotted line). Gray-shaded portions of the columns represent the number of events with identified source region. The numbers in brackets indicate the fraction of structured events with respect to the total CME frequency per year.

3.3.2 Angular widths and position angles

Although included in the CME Catalogue, the central position angle (PA) and angular width (AW) of the CMEs were recalculated, since the method used to determine the values provided by

* A full version of Table 1 with the 276 selected events may be obtained at *ftp://ftp.linmpi.mpg.de/outgoing/cremades* or by request to the author.
† Solar Influences Data analysis Center, Royal Observatory of Belgium.

the CME Catalogue is not satisfactory for our purposes. It takes into account brightness differences with respect to the surrounding corona, which often were found not to be part of the structured CME itself (problem addressed by Michalek et al. 2003). They consisted rather of deflections of pre-existing coronal structures or short-lived wave-like disturbances of the ambient corona. The recalculation of these two angular parameters for the selected CMEs was carried out on the last C2 image in time that showed the leading edge of the CME before it left the FOV of C2. To improve the contrast, a pre-event snapshot was subtracted, obtaining in this manner a differential image, exemplified in Figure 3.3. With the aid of brightness contour levels, taking into account the brightness of the individual event and that of the background corona, the AW and central PA were calculated as:

$AW = PA_1 - PA_2$ and
$PA_{central} = (PA_1 + PA_2)/2$

Where PA_1 and PA_2 represent the two outer edges of the CME projected onto the plane of the sky measured counter clockwise from the solar north (PA = 0), with the vertex being located in the centre of the solar disk.

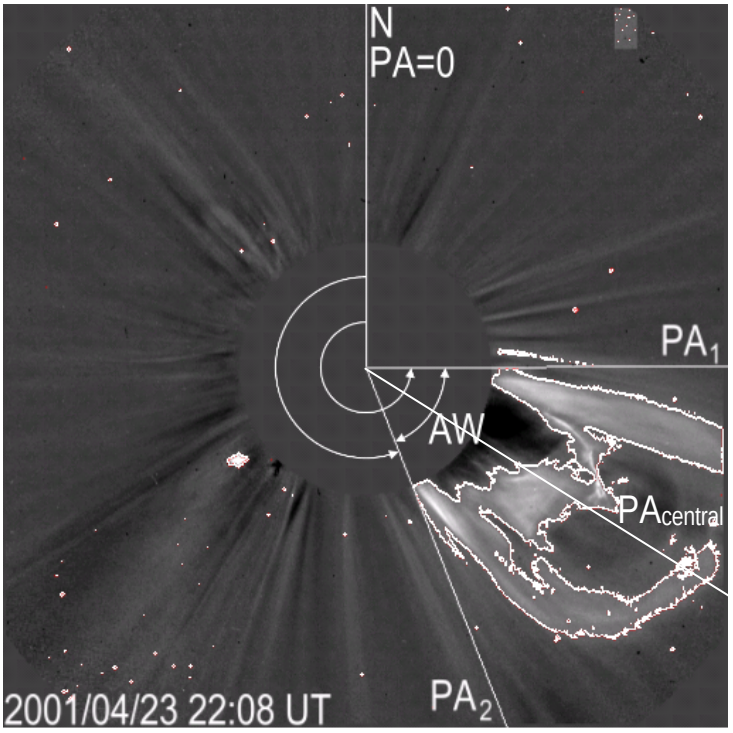

Figure 3.3. LASCO/C2 image of a structured CME on April 23, 2001, from which a pre-event image at 18:11 UT has been subtracted. A white contour delineates the structured CME, delimited by the position angles PA1 and PA2 and subtending an angular width AW.

The recalculated values of AW and PA are given in columns 3 and 4 of Table 1 respectively. They can be compared to those of the CME Catalogue. The individual differences range from just a few to more than two hundred degrees, since the method used to determine the Catalogue values includes also disturbances sometimes not part of the CME, resembling therefore some doubtful halo CMEs (mimic halos). The frequency distribution of the recalculated AWs is presented in Figure 3.4 as a histogram with bins of 15°. The maximum frequency lies in the range 75°-90°, with an average AW of 85°, while the average AW as calculated from the CME Catalogue would have been of 155°. The finding implies that CME parameters need to be treated carefully in general, especially when physical quantities, such as CME masses and kinetic energies, are considered. Furthermore, it is worth to note that AW and PA are apparent quantities that depend on the orientation of the CME with respect to the observer. A different direction of

propagation may give the impression of a wider or narrower AW, what is known as projection effect. The average AW of structured CMEs is substantially larger when compared with the mean AWs of CMEs observed by previous space missions (in agreement with the results from Burkepile et al. 2004). For instance, the average AW obtained for the CMEs detected by the Solwind instrument onboard the P-78 spacecraft during 1979-1981 was 45°, and 24° for the years 1984-1985 (Howard et al. 1985, 1986). For the ~1300 CMEs recorded by the SMM instrument during 1980 and 1984-1989, the average AW resulted to be 47° (Hundhausen 1993), while the mean value of the AW for the 240 CMEs recorded by the ground-based coronagraph MK3 during 1980-1989 yielded 37° (St. Cyr et al. 1999). Furthermore, St. Cyr et al. (2000) determined an average AW of 72° for the 841 LASCO CMEs identified between January 1996 and June 1998; whereas Yashiro et al. (2004) calculated yearly averaged AWs for the LASCO CMEs (with AW between 20° and 120°) during the period 1996-2002, yielding values ranging from 47° up to 61°. The larger value of the average AW obtained for structured CMEs seems to be closely related to the selection criterion: the most spectacular events were all quite sizeable, whereas narrow CMEs typically showed no fine structure. Note that the overall shape of the AW distribution displayed in Fig. 5 agrees with those of previous studies (Howard et al. 1985, 1986; Hundhausen 1993; St. Cyr et al. 1999; Gopalswamy et al. 2003), somewhat skewed on the right, but in this case displaced toward higher values.

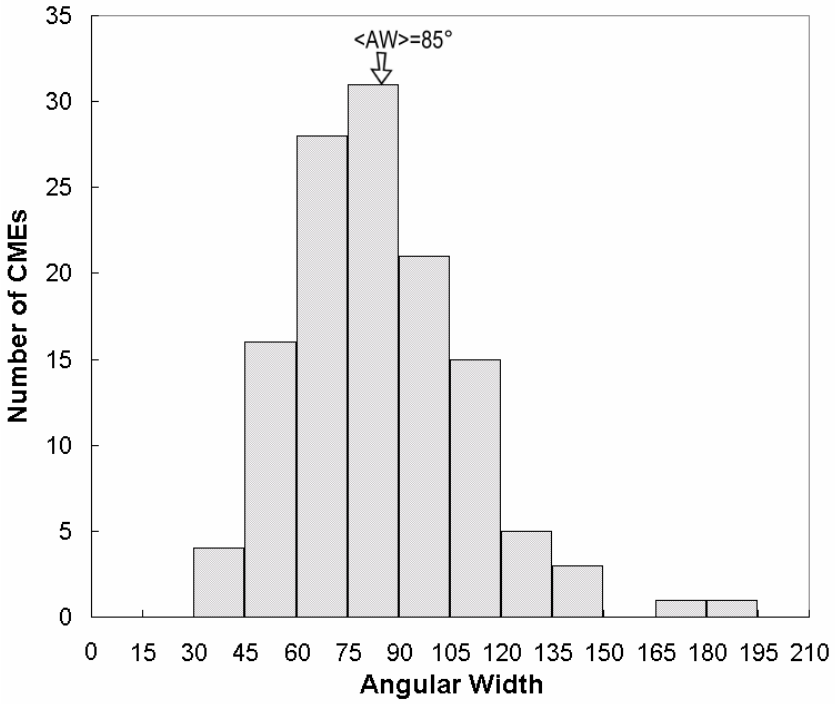

Figure 3.4. AW distribution histogram for the 124 structured CMEs with identified source regions. The arrow indicates the average AW.

New PAs resulted from the recalculation of the AWs, listed in column 4 of Table 1. Their frequency distribution, presented in Figure 3.5, shows a marked concentration of events at equatorial latitudes, equivalent to PAs of 90° and 270°. On the other hand, very few events were found at polar latitudes (PAs of 0° and 180°). The reason for such a distribution becomes clear when the locations of their associated source regions are analyzed. The CME PAs are discussed together with those of the corresponding source regions in Subsection 3.5.3.

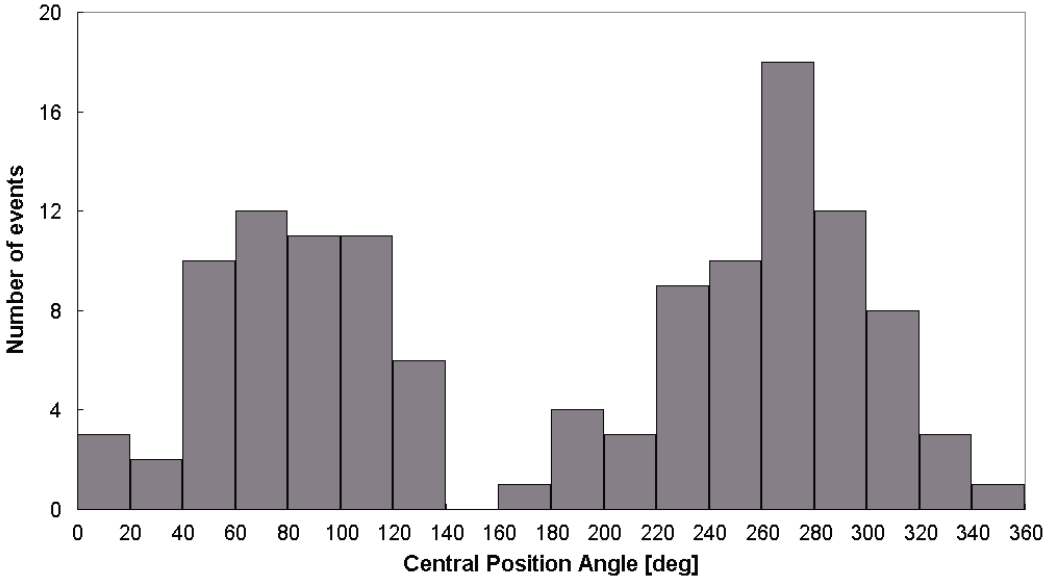

Figure 3.5. PA distribution histogram for the 124 structured CMEs with identified source regions.

3.3.3 Speeds

The speeds of the structured CMEs presented in column 5 of Table 1 have been extracted from the LASCO CME Catalogue at *http://cdaw.gsfc.nasa.gov/CME list/*. These arise either from a linear or from a second-order fit through the points of a height-time (H-T) diagram. The H-T diagrams created by the LASCO CME Catalogue display the height evolution of the fastest feature, usually the leading edge, as a function of time (see Figure 3.6 and Figure 3.7). The diagram of each particular event was inspected, in order to deduce whether it was more appropriate to use the speed approximated by a linear fit or by a second-order fit. It is not the aim to subdivide the structured CMEs into two groups according to their speed profile, as addressed by, e.g., Sheeley et al. (1999). However, the most suitable fit through the points was chosen in each case. In the case of second order fit, the speed corresponding to the last height of measurement was considered. The two examples of H-T diagrams presented in Figure 3.7 show a) a case better approximated by a linear fit, and b) an event better approximated by a second-order fit. It is worth to note that all the presented speeds are plane-of-sky speeds, i.e. the measured quantity is the projection of the real propagation speed on that plane. The overall speed distribution of the structured CMEs is presented in Figure 3.8. The maximum is centred at ~750 km s^{-1}, while the average speed is ~900 km s^{-1}. These values are quite high when compared with other CME datasets. For instance, Hundhausen et al. (1994) found for SMM CMEs during 1980 and the period 1984-1989 annual averages of ~400 km s^{-1}. The amount of low features (< 300 km s^{-1}) was considerably higher, while the upper values of speeds barely exceed the 1200 km s^{-1}. A similar behaviour was found by Howard et al. (1985) and St. Cyr et al. (1999). Howard et al. (1985) calculated for Solwind CMEs during 1979-1981 an average speed of 470 km s^{-1}. St. Cyr et al., in their comparison between MK3 and SMM CMEs during 1980-1989, calculated average values of 533 and 519 km s^{-1} respectively for each coronagraph. In the case of LASCO CMEs within 1996-2002, Yashiro et al. (2004) found annual averages between ~300 and 500 km s^{-1}.

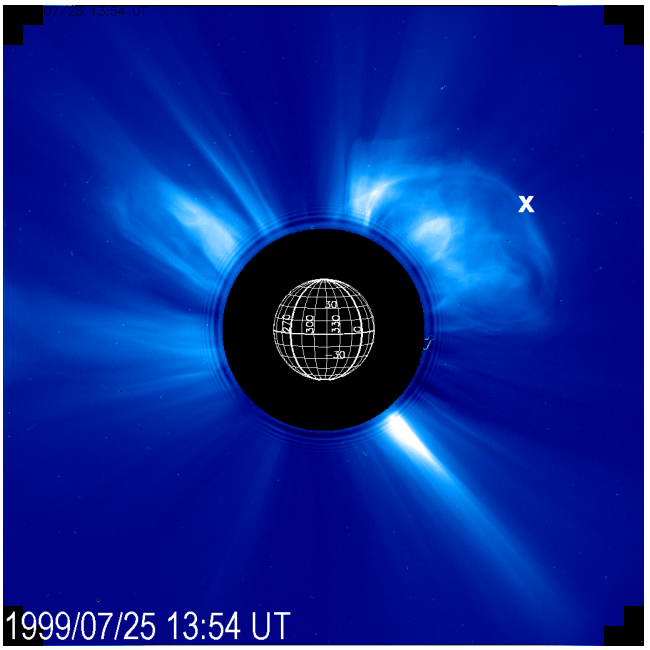

Figure 3.6. The CME on July 25, 1999, as recorded by LASCO C2. The cross indicates the position of the fastest feature of the CME, employed to construct the height-time diagram.

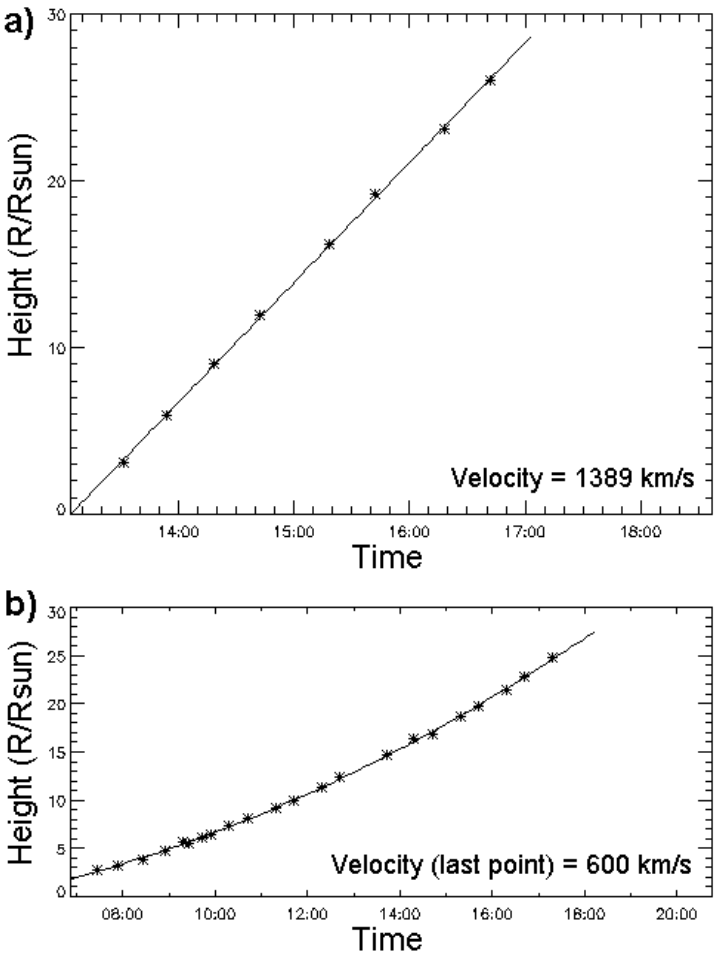

Figure 3.7. Height-time diagrams extracted from the LASCO CME Catalog. a) a linear fit through the points corresponding to the event on July 25, 1999. b) a second-order fit related to the event on March 17, 1999.

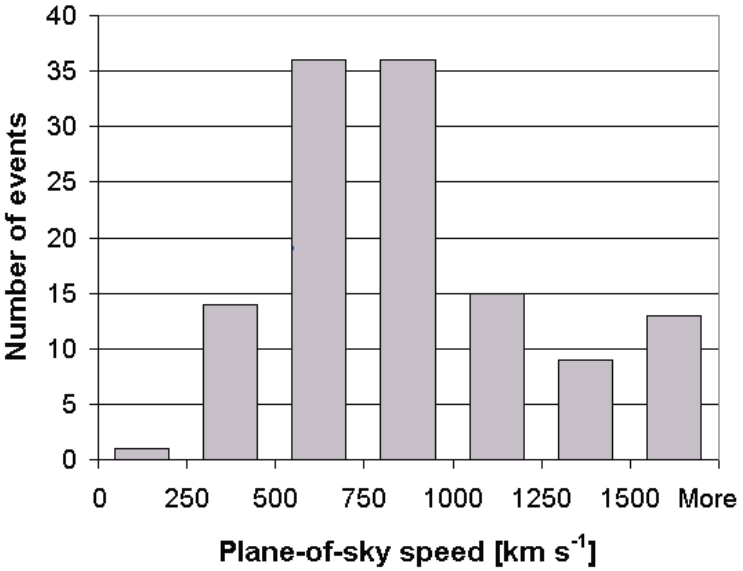

Figure 3.8. Histogram of the plane-of-sky speeds related to the structured CMEs, in bins of 250 km s^{-1}.

3.4 Source regions

The dependence of CME properties on their associated source regions' attributes has been tackled by numerous authors (e.g., Munro et al. 1979; Subramanian & Dere 2001; Pojoga & Wang 2003), and is nonetheless a matter still under research. In an attempt to reveal the configuration of the structured CMEs, an approach based on the source region characterization is addressed. To begin, the main aspects of the source regions associated with the structured CMEs are discussed in the following subsections.

3.4.1 Identification

In order to identify the source region (SR) in the low corona for each of the 276 structured CMEs, EIT observations taken at 195 Å were investigated for pre- and post-eruptive signatures of CMEs, such as: outward motion of coronal material in form of loops or eruptive prominences (e.g., Webb & Hundhausen 1987), flares (Hudson et al. 1998), coronal waves and dimmings (Thompson et al. 1998; Zhukov & Auchère 2004) or post-eruptive loops/arcades (Sterling et al. 2000; Tripathi et al. 2004). Some of these are exemplified in Figure 3.9, for four of the CME events of Table 1. To reveal faint features, running difference images were employed, which are obtained after the subtraction of successive snapshots (see Section 2.4). White areas denote an increase of emission from the previous image to the new one, while dark areas symbolize a decrease of emission. The Figure shows in the clockwise direction: rising low coronal loops, a prominence eruption, a post-eruptive arcade and a coronal dimming characterized by a transitory absence of emission.

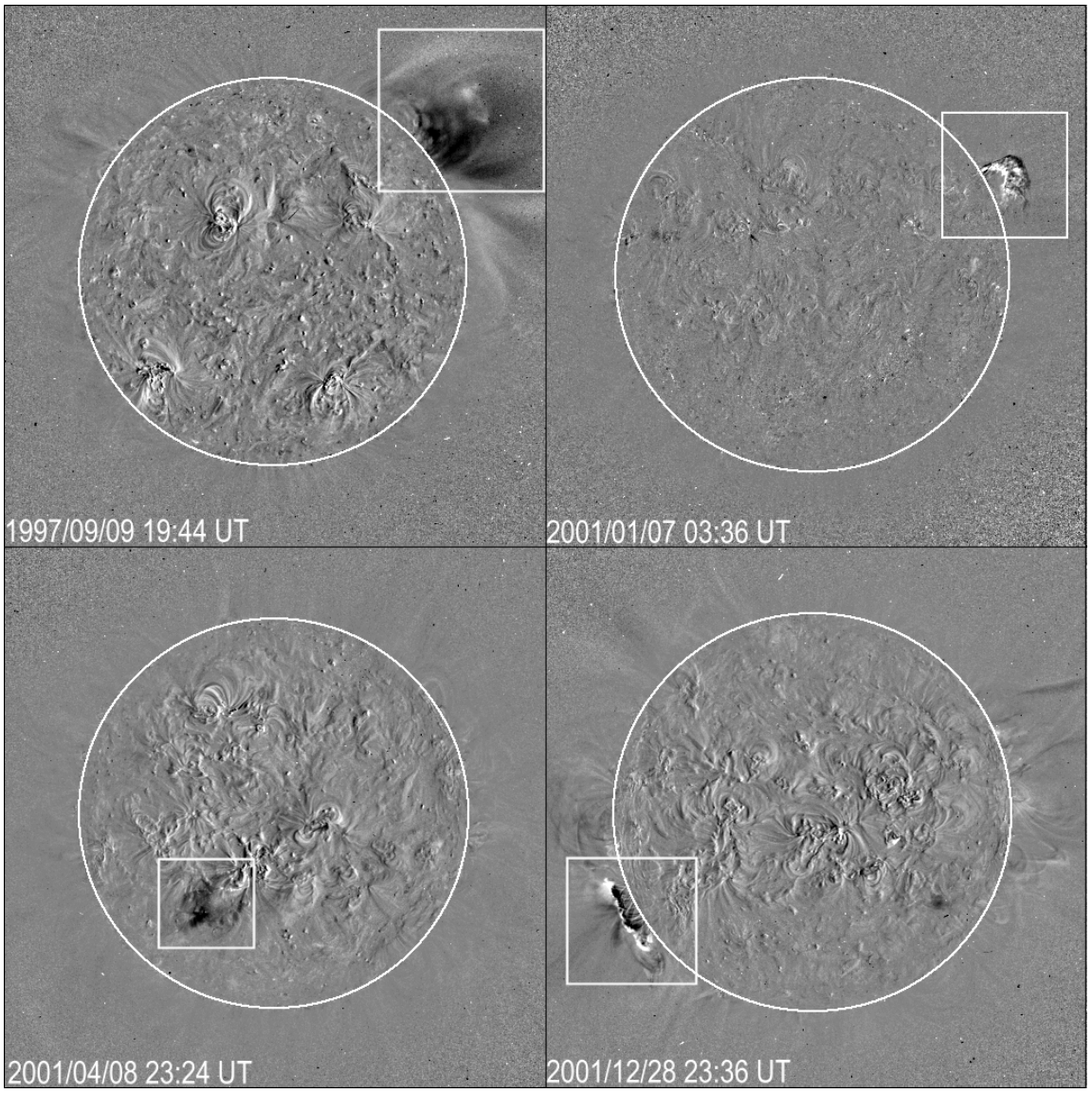

Figure 3.9. EIT 195 Å running difference images, of eruptive (top) and post eruptive (bottom) signatures associated with four structured CMEs. Features within the squares, in clockwise direction: rising low coronal loops, a prominence eruption, a post-eruptive arcade and a coronal dimming.

For each event the temporal and spatial relationship of LASCO and EIT features were investigated, in order to make proper associations. At times of high solar activity, when the proliferation of active regions and the brightness of the overall solar corona increase, the search for associations was especially difficult. The time of the first observation of the CME in the FOV of C2 needed to be in agreement with the expected propagation time of the features seen by EIT lower down in the corona, as verified with the aid of height-time diagrams acquired from the CME Catalogue. Naturally the features identified in EIT observations had to be enveloped by the two edge PAs defining the CME spatial extent. Additionally Hα and SXT data from Yohkoh were consulted in order to ensure the veracity of the candidate SR. After evaluating all events and associated activity in the EIT FOV, the SR could be identified for 124 (45%) events out of the total number of 276 structured CMEs, which are listed in Table 1. For 152 events (55% of the cases) the SR could not be identified, most often because they were far sided (117 events, 77%) and/or they showed very weak or too complex signatures.

3.4.2 Solar location

The source regions of the structured CMEs found in EIT 195 Å were traced back to MDI synoptic charts, in order to establish their photospheric magnetic counterparts. MDI synoptic charts are magnetic maps of the Sun for a full solar rotation, built by putting side by side vertical bands from daily full-disk MDI observations. After direct visual comparison, it turned out that the SRs were generally associated with opposite polarity regions in both hemispheres, in agreement with the findings of Subramanian & Dere (2001). Note that the term opposite polarity regions is used rather than bipolar regions because it comprises not only active bipolar regions but also decaying ones, and hence it can be employed for bipolar regions independently of their characteristics (e.g., Wang & Sheeley 1989). Examples are presented in Figure 3.10, where the SRs for the selected CMEs during Carrington rotation 1961 are denoted by dashed circles (events dated April 5, April 8 and April 23, 2000 of Table 1). The solid line within the circles defines the disturbed portion of the polarity inversion line, identified through the position of the filament that erupted or through the location of post-eruptive EUV arcades or dimmings. Although polarity inversion lines might present substantial curvature in individual cases (see Figure 3.32 later), they have been approximated by straight lines. Note that neutral lines may be certainly long, being only a portion of them involved in the eruption. In this work, *the source region extent was solely determined by the length of a disappearing filament or by the extent of post-eruptive features.* The location of a SR is determined by the Carrington coordinates of the two endpoints of the neutral line's disturbed section. Carrington latitudes and longitudes of the first and second endpoints (indicated by a subscript '1' and '2' respectively) are given in columns 6 to 9 of Table 1. They were ascertained with the aid of the IDL procedure IMAGE_TOOL (see Subsection 2.4.2) and inferred directly from Hα images in cases of clear filament disappearances, and from EIT images if neat post-eruptive loops were observed. In the remaining cases the coordinates resulted from a combined investigation of EIT, Hα, and MDI data to minimize uncertainties in the heliographic coordinates.

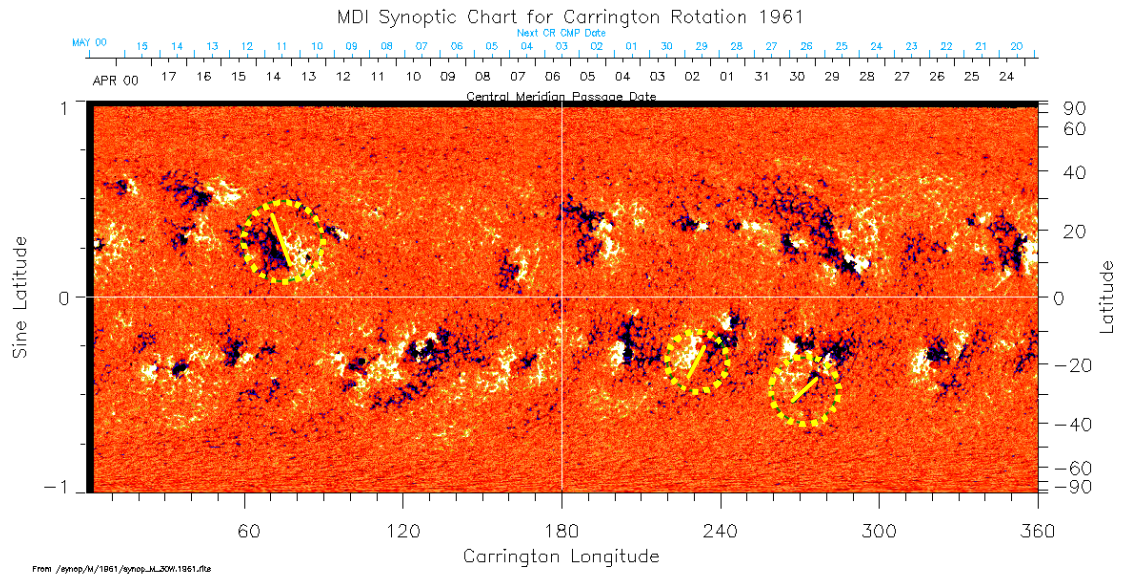

Figure 3.10. SOHO/MDI synoptic chart exhibiting (encircled) the photospheric source regions of three structured CMEs as identified from backtracking of EIT images. The straight line within the circles represents the disturbed portion of neutral line separating opposite polarities. White areas represent positive magnetic polarities, and black areas negative ones.

The position and extents of the structured CMEs' SRs are illustrated in Figure 3.11. A big concentration of SRs is found in the two activity region belts centred at ±20° latitude. At trans-equatorial latitudes and at latitudes above 60° no SRs could be observed, either because of the absence of solar activity at such high latitudes or given the extremely poor resolution of the MDI instrument in polar regions. The average SR latitude in the northern hemisphere was of 25°±11° and in the southern -24°±9°. In the figure, the source regions have been classified in three categories, distinguished by their colours. SRs sorted as 'active regions' may have involved or not an observable disappearance of an active filament. The group 'filaments outside active regions' comprises source regions related with a disappearing filament located in a decaying bipolar region. Finally, the category 'uncertain' includes events that didn't qualify for any of the previous groups, e.g. in the cases of filament re-formation* or backside-located SRs. Out of the 124 structured CME SRs, 47 (38%) corresponded to active regions, 65 (52.5%) to filaments outside active regions, and 12 (9.5%) cases were uncertain. The average latitude of the 'active regions' group was 19°±7°, while that of 'filaments outside active regions' was 28°±11°.

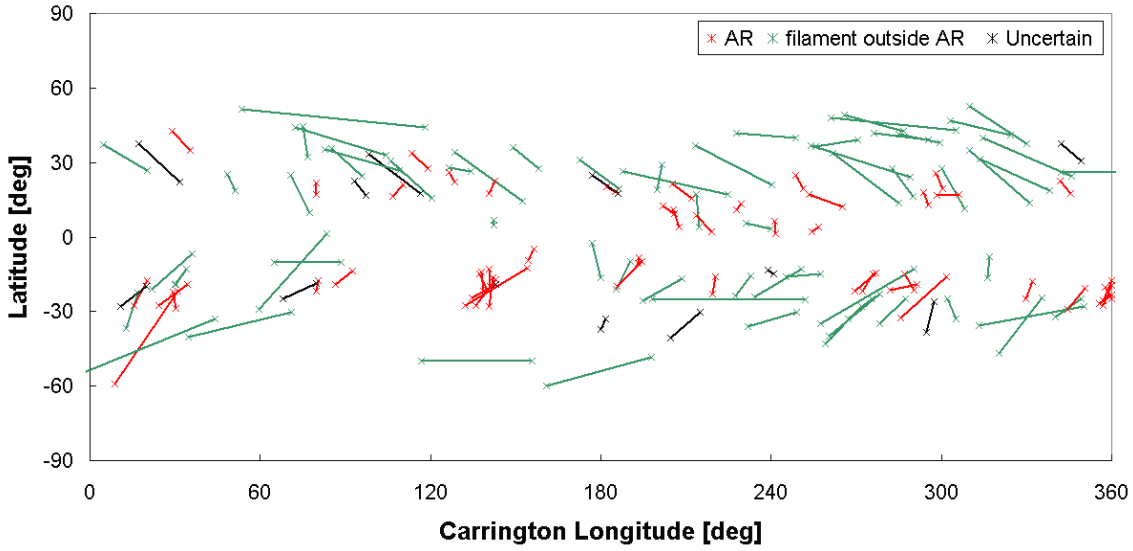

Figure 3.11. The positions and lengths of the 124 structured CMEs' SRs identified during 1996-2002, represented by straight lines and compiled together in a Carrington Map. The color codes indicate the type of source region: active region (AR, red), filament outside active region (green), and uncertain (black).

The SRs' locations on the solar disk with respect to the observer can be calculated in terms of their heliographic longitudes. For this purpose, the coordinates of the source regions have been approximated by those of their midpoints. The frequency distribution of the SRs' relative location on the Sun is indicated in Figure 3.12. Events located not farther from the limb than ±20° in heliographic longitude have been grouped in the *limb* category, i.e. events in the range 70° to 110° in longitude with respect to central meridian. Events situated between 50° and 70° heliographic longitude were classified as *near limb* events. Finally, the category *disk events* was devoted to those SRs located at the remaining longitudes. Some far-side SRs could also be identified, especially at times of low activity, when the CME PA matched the location of well-pronounced isolated regions, seen in the magnetogram before they entered the far side of the Sun or when they appeared at the east limb, with noticeable eruptive and post-eruptive signatures

* It is not unusual that, after a filament disappearance, a new filament reforms at almost the same location of its predecessor.

from SRs that were just behind the limb. Such cases, i.e. those whose mean absolute heliographic longitudes were greater than 90°, have been denoted by a superscript *a* in Table 1. The least likely place that allows the determination of a CME's SR lies obviously close to disk centre on the opposite side of the Sun, as viewed from SOHO. As can be seen from Figure 3.12, and as may be anticipated from the definition of structured CMEs, the highest percentage of events resulted from SRs located at and near the limb. This finding indicates that projection effects play a major role in the appearance of CMEs in the FOV of the LASCO coronagraphs, since halo CMEs cannot be different from structured CMEs in general. Hence the identified set of structured events provides a unique database , since limb events provide the purest samples for the determination of the physical parameters characterizing CMEs, such as AW, speed, or mass. It is known that limb CMEs keep their AW during their outward propagation, while CMEs originating from other regions of the solar disk will seemingly gain AW as they travel farther away from the Sun, due to projection effects (e.g., Webb et al. 1997; Burkepile et al. 2004). Note that about half of all partial halos turn into full halos shortly after they are detected, and from then on encompass completely the occulting disk. Furthermore, the observed speed of the leading edge on the plane of the sky of limb CMEs is approximately equal to the real propagation speed of the CME.

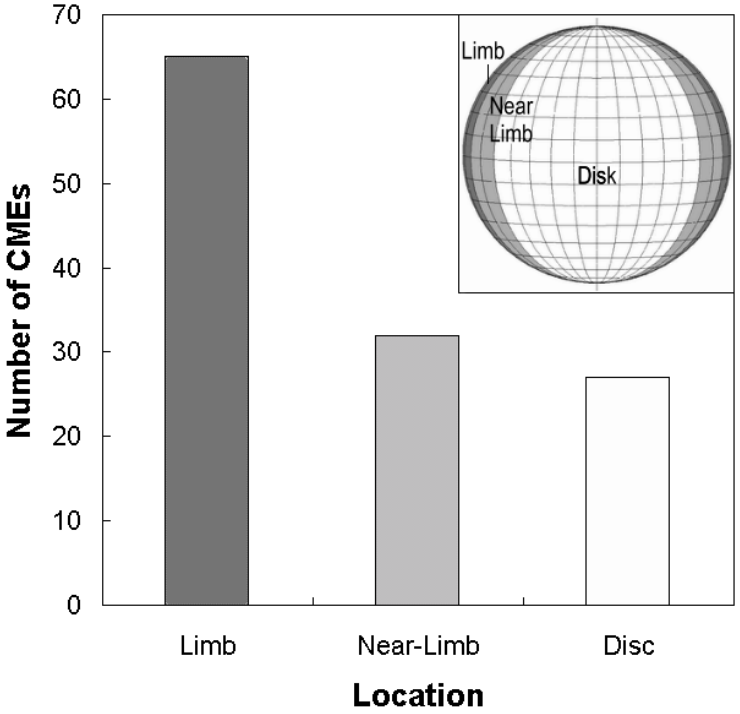

Figure 3.12. Distribution of the identified SRs on the Sun, as seen from SOHO. The inset explains the bin tags: limb cases (SRs not farther from the limb than ±20° hel. lon.), near limb cases (SRs between 50° and 70° hel. lon.) and disk cases (remaining longitudes).

3.4.3 Tilt and length

According to Figure 3.11, the typical orientation of the structured CME SRs is from NE to SW in the northern hemisphere and NW to SE in the southern. These orientations follow Joy's Law (Hale et al. 1919), according to which the following polarity of sunspot pairs tends to appear farther away from the Equator than that of the preceding one of opposite polarity. The tilt angle γ displayed in column 10 of Table 1 has been measured with respect to the north-south line (method also used by Trottet & MacQueen 1980), as sketched in the inset of Figure 3.13. The angle γ varies from 0° to 90°, where a tilt of 0° corresponds to a vertical neutral line and one of 90° to a horizontal line. Positive values of γ correspond to the natural inclination as expected from Joy's law, while negative tilts oppose to those. From the 124 analyzed events, just 18 (14.5%) showed negative γ, noticeable in Figure 3.11. A histogram of the tilt γ is presented in

Figure 3.13, in bins of 30° and sorted by source region type. The overall distribution has its maximum in the interval 30° - 60° while averages amount 44° and -37° for positive and negative γ respectively. After sorting the SRs according to their properties, the averages found for each group are substantially different. For instance, $\langle +\gamma \rangle = 35° \pm 18°$ in the case of active regions, while $\langle +\gamma \rangle = 52° \pm 23°$ for the extended filaments in decaying regions that have suffered for a longer period of time the effects of the solar differential rotation.

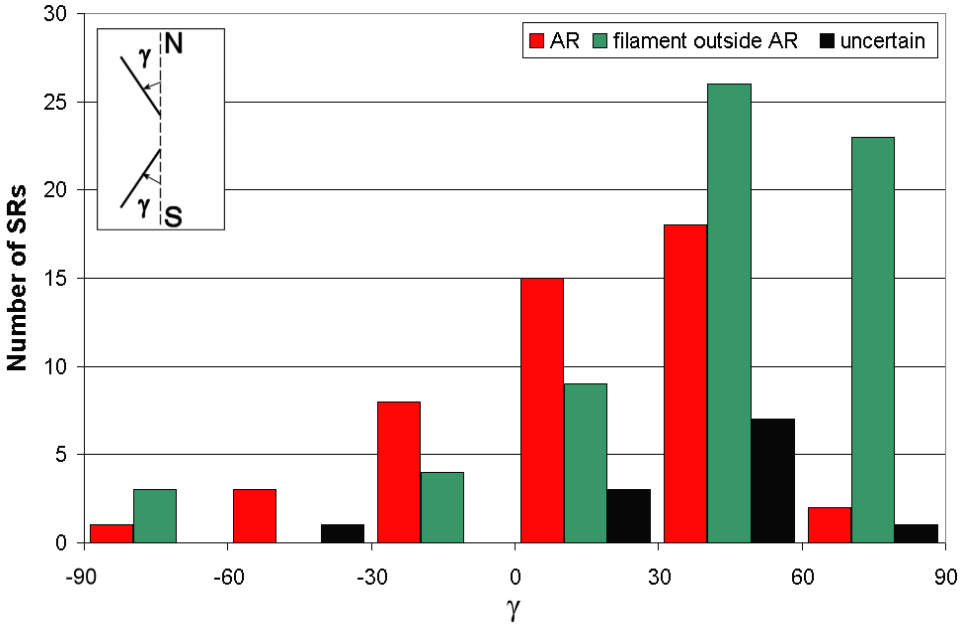

Figure 3.13. Frequency distribution of the SRs' tilt angle γ. The inset explains the direction in which positive tilts grow in both hemispheres. The color codes indicate the type of source region.

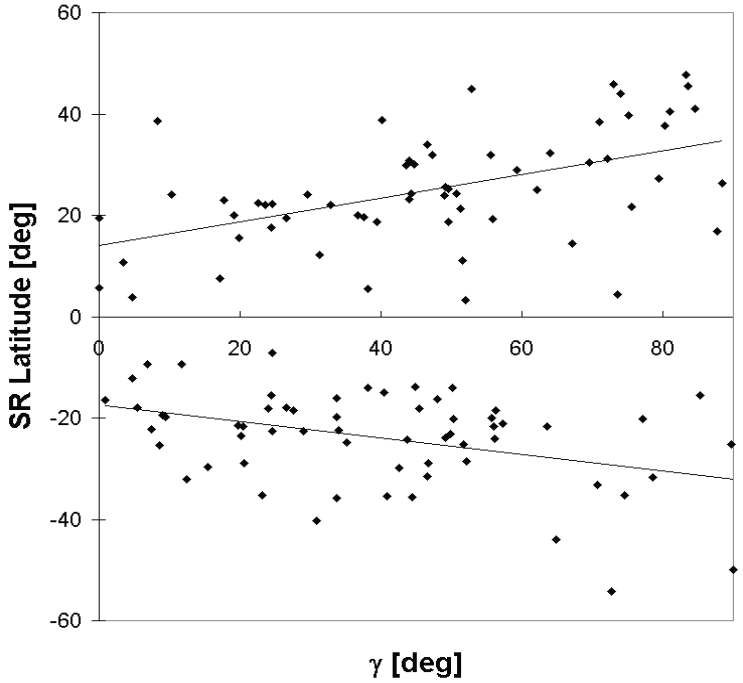

Figure 3.14. Heliographic latitude of the structured CME SRs as a function of absolute tilt γ. A γ = 0° represents vertically oriented SRs. The straight lines indicate linear fits through the points corresponding to the northern and southern hemispheres.

There is a marked dependence of γ on the SR latitude, as may be seen in Figure 3.14. The linear fits in the north and south hemisphere are asymmetric. The dependence is more pronounced in the northern hemisphere, related to a different latitudinal distribution of the SRs in both hemispheres.

The measured lengths of the SRs, displayed in column 11 of Table 1, range from a few degrees up to more than 40°. The histogram displayed in Figure 3.15 shows a poissonian-type distribution, with its maximum located in the bin 6°-12° and average length of 14.5°. The lengths of the SRs are considerably smaller than the AWs of the respective CMEs (see Table 1), indicating an enormous expansion of small-scale magnetic structures from the low corona into the FOV of C2, which will be addressed later in Subsection 3.6.2.

The behaviour of the SR Length with respect to the latitude is compared in Figure 3.16. There is a clear tendency at higher latitudes for longer SRs, i.e. with lengths above 20°. Conversely, the shortest CME SRs are located below heliographic latitudes of ±30°. Recapitulating, an increase in latitude is directly related with an increase in γ and an increase in the the SR length as well. Thus, the larger SRs tend to appear at higher latitudes, and at high latitudes there is a trend for γ to be more horizontal. Then, there is also a dependence between SR length and SR tilt, i.e. the larger SRs tend to be more horizontal.

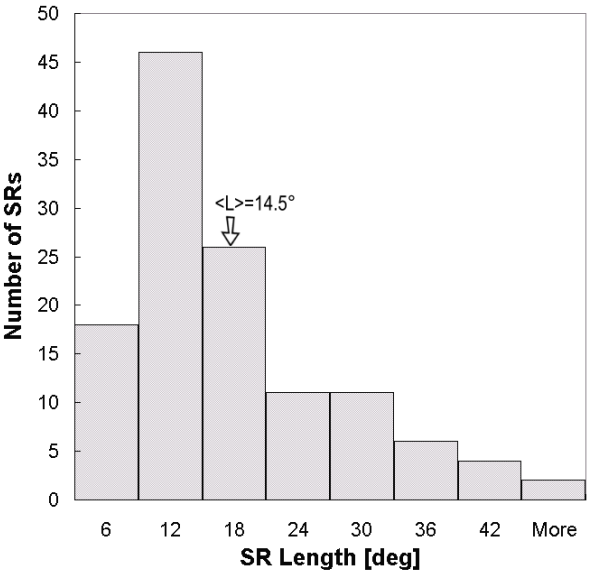

Figure 3.15. Distribution histogram of the SR lengths, sorted in bins of 6°. The overall average length is indicated by the arrow.

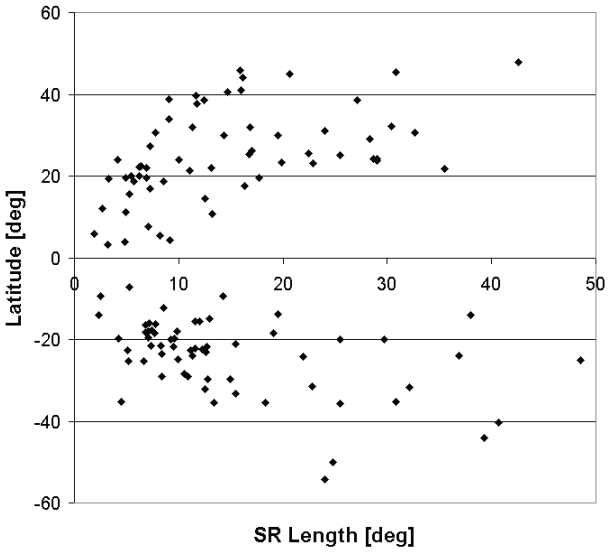

Figure 3.16. Latitudinal dependence of the SR Length based on 124 cases of the set of structured CMEs.

3.5 Solar cycle variation

The time coverage of the SOHO mission has not only been extensive, but also basically uninterrupted (with exception of few months during the year 1998). In this sense, the dataset that the SOHO mission provides is exceptional and constitutes a unique opportunity to analyze temporal variations on large time scales. The evolution of CME and SR parameters over the rising and maximum phases of solar cycle 23 are investigated in the following subsections. These include SR tilt angle, SR latitude, CME PA, and deflection of CMEs with respect to their source regions.

3.5.1 Source region tilt

The tilts of neutral lines are of special interest because of their plausible relationship with MC orientation (Bothmer & Schwenn 1998; Yurchyshyn et al. 2001; Bothmer 2003). The tilt angle γ arises from the lineal approach of neutral lines as CME source regions, and has been calculated as already specified in Section 3.4.3. A tilt $\gamma = 0°$ corresponds to a vertical neutral line and $\gamma = 90°$ relates to a horizontal line. Figure 3.17 displays absolute values of γ (black points) as a function of time during the period 1996-2002. Blank triangles are the result of averaging sets of 10 consecutive values of γ, while the bars' lengths are given by the standard deviation of the corresponding averaged points. The temporal variation of γ reveals no clear systematic trend until mid 2000. After that (i.e. after the Sun's global magnetic polarity reversal, Wang et al. 2002) a tendency for lower inclined cases ($\gamma > 45°$) becomes visible. The higher values of γ indicated by the averages in mid 2000 may be related with the appearance of high-latitude source regions addressed in the next subsection. This fact is also consistent with the relationship between γ and latitude derived from Figure 3.14.

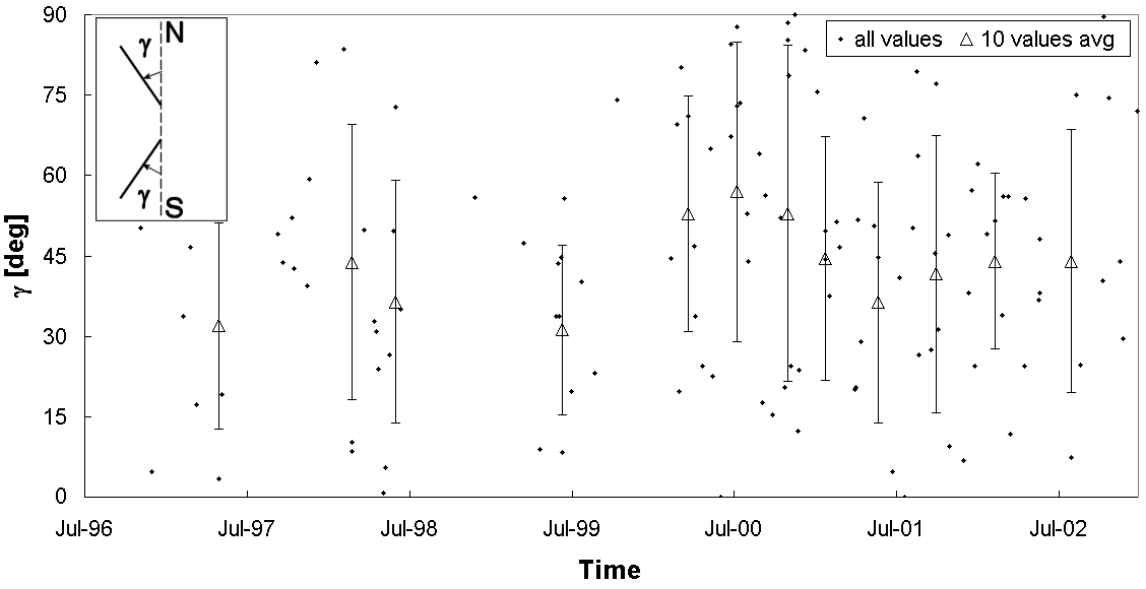

Figure 3.17. Evolution of the structured CME SR tilt angle γ in time (dark points). The inset indicates the direction in which positive tilts grow in both hemispheres. Triangles represent averages over 10 consecutive values of γ, and error bars are determined from the standard deviation of the respective averaged values.

3.5.2 Source region latitude

To investigate the temporal variation of the SR latitude, only the midpoint of each linear source region was considered as representative of the SR. Absolute values of the SR latitude are plotted in Figure 3.18, together with averages of 10 consecutive data points (blank triangles). The overall distribution follows the butterfly diagram (see Figure 1.3) of the appearance of sunspots. This behaviour is probably due to the significant presence of active regions in the group of the structured CMEs' SRs.

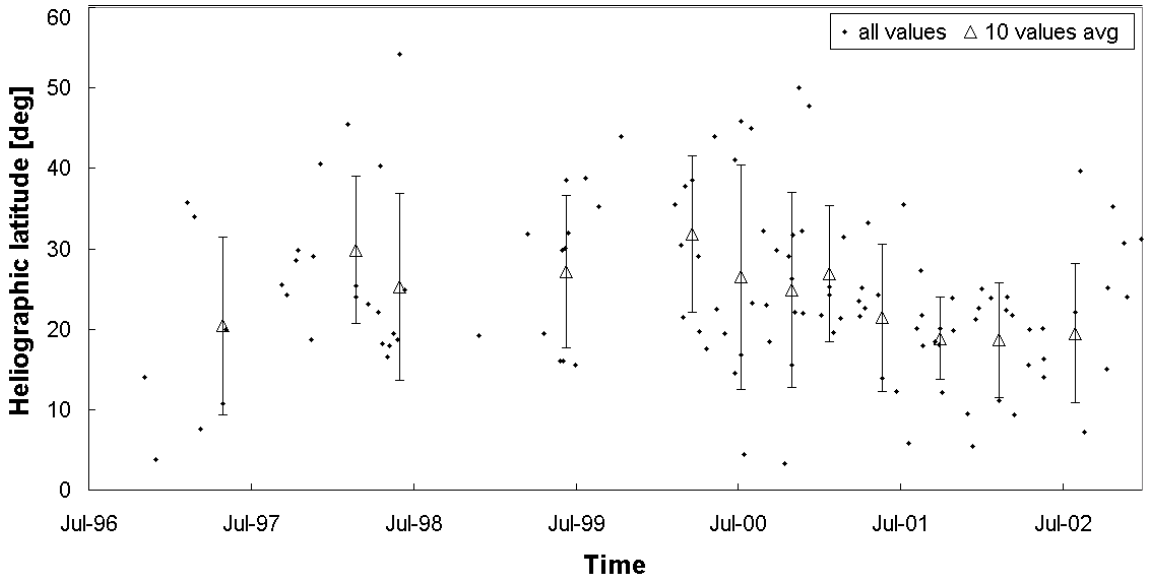

Figure 3.18. Temporal evolution of the structured CME SR latitude (dark points). Triangles represent averages over 10 consecutive values of γ, and error bars are estimated from the standard deviation of the respective averaged values.

The similar trends revealed in Figure 3.17 and Figure 3.18 demonstrate the dependence of γ on latitude, as already mentioned in the previous section: on average, higher latitude SRs are more horizontally inclined (high γ) while lower latitude ones are more vertically inclined (small γ).

It is interesting to compare the temporal evolution of the latitudes together with the longitudinally averaged magnetic field (provided by D. Hathaway, NASA/NSSTC) for the same period of time, as done in Figure 3.19. Again, only the midpoint of each source region was considered as representative. In the figure, blue-shaded areas refer to negative polarities and yellow ones to positive polarities, while red diamonds represent active regions and green squares filaments outside active regions. The comparison reveals on the one hand that especially active regions as structured CME sources follow the butterfly diagram. On the other hand, the migration towards higher latitudes of CME source regions associated with filaments outside active regions is also apparent. This fact seems to coincide with times of large spread in latitude of newly emerging magnetic flux and strong flux migrations towards the poles (e.g., Benevolenskaya et al. 2002).

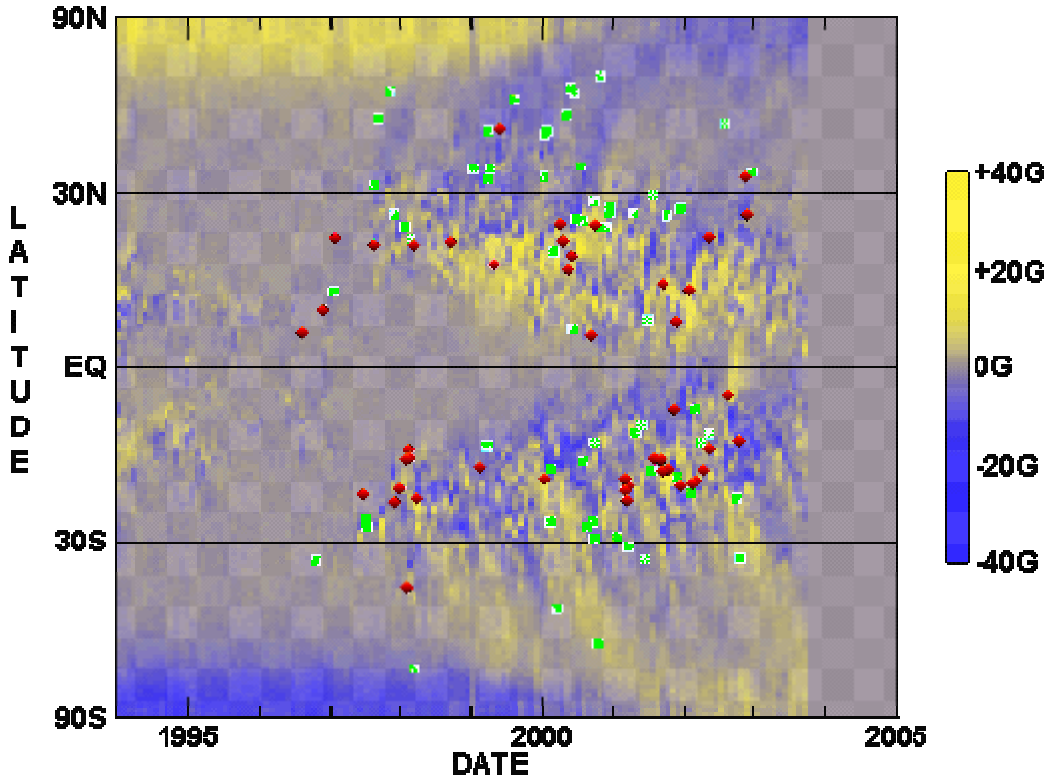

Figure 3.19. Latitudinal evolution in time of the structured CME SRs, superimposed on the longitudinally averaged magnetic field for the same time period, courtesy of D. Hathaway, NASA/NSSTC. Red diamonds stand for active regions and green squares for filaments in decaying bipolar regions. Yellow- and blue-shaded areas represent positive and negative polarities respectively.

3.5.3 CME and source region position angle

The variation of the central position angles derived for the structured CMEs is plotted against time in Figure 3.20. The CME central PAs may be sorted in two categories: eastern PAs (0°-180°, lower data points) and western PAs (180°-360°, upper data points). During low solar activity (green circles), there is a clear confinement of CME PAs to equatorial regions (PA ≅ 90° and PA ≅ 270°), while in times of maximum activity (red diamonds) the PAs fluctuate, reaching even polar values (PA ≅ 0° and PA ≅ 180°). The confinement of CMEs to equatorial regions in times of solar minimum, as well as the spread over all PAs during solar maximum, have been previously observed in the Solwind (Howard et al. 1985, 1986), the SMM (Hundhausen 1993) and the MK3 (St. Cyr et al. 1999) datasets.

In order to interpret correctly the meaning of PA, it is worth to keep in mind that it is just an apparent measure of the angular position of a CME, projected on the sky-plane. Therefore, CMEs with polar values of PA may just seem to be located above the poles due to projection effects. In fact, a CME does not necessarily need to originate from polar latitudes on the Sun itself to be seen 'apparently' above the poles. That is the case of the structured CME observed on February 27, 2000 (see Figure 3.21), apparently located over the North Pole, but actually originated from a source region located at a latitude of ~30°N.

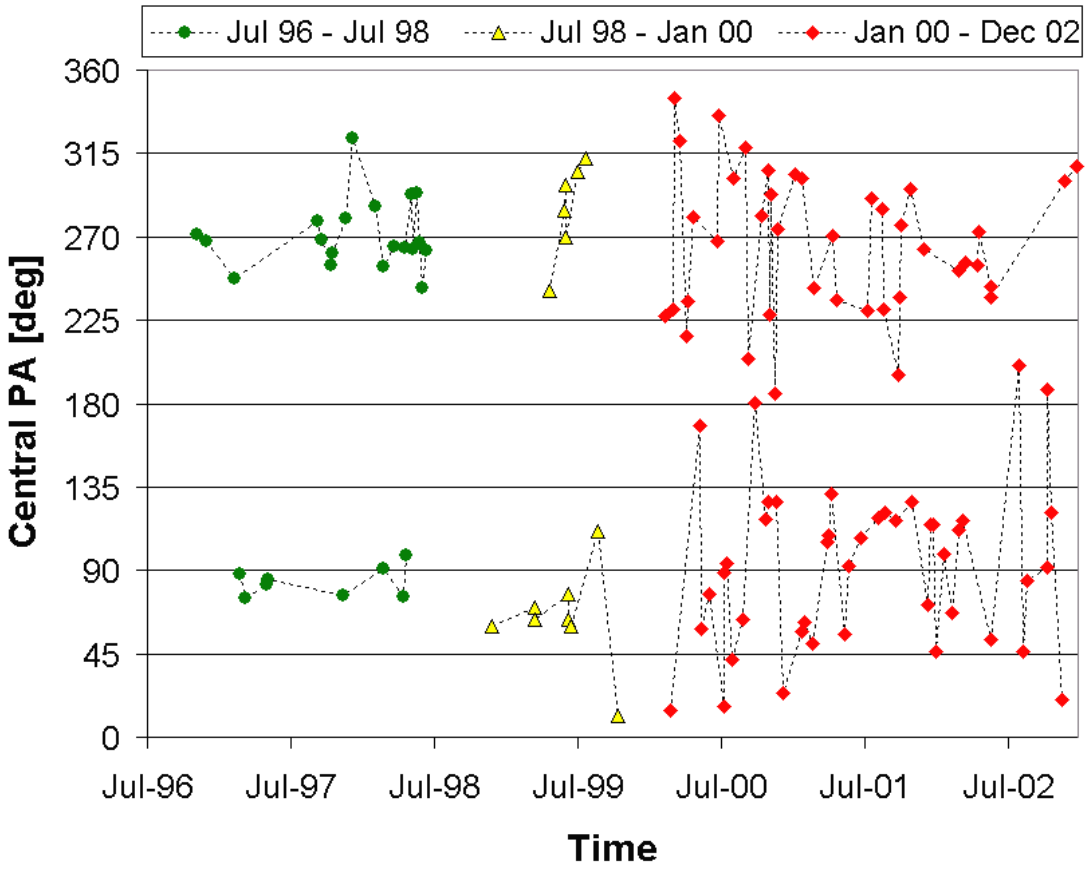

Figure 3.20. PA evolution in time of the structured CMEs. Upper data points represent eastern PAs (0°-180°) whereas lower datapoints represent western ones (180°-360°). The points have been sorted into three time periods with different behaviour.

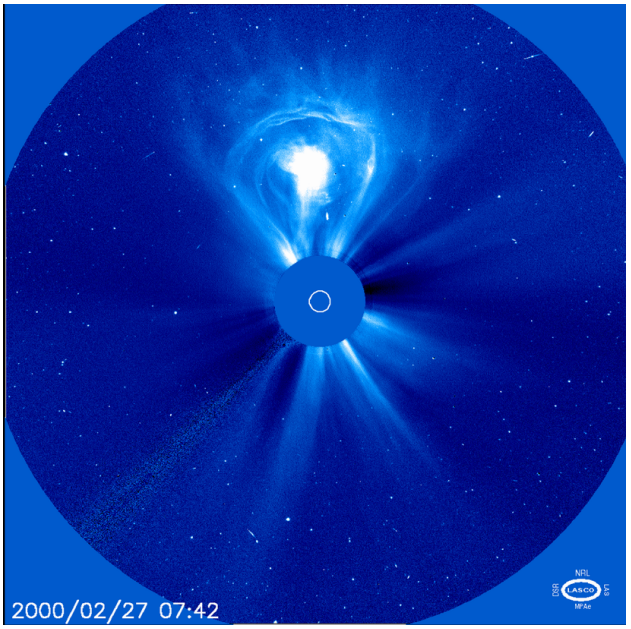

Figure 3.21. The "lightbulb" CME on February 27, 2000, as observed by the LASCO/C3 coronagraph.

A proper way of comparing the position angle of a CME with the location of its respective SR is by means of the source region PA. It is calculated by projecting the midpoint of a SR on the solar limb, given its heliographic latitude and longitude, and therefore it accounts for projection effects determined by the source region location. CME and SR position angles are contrasted in Figure 3.22, where CME occurrence rates are given by the rectangular columns and SR frequencies by the solid line.

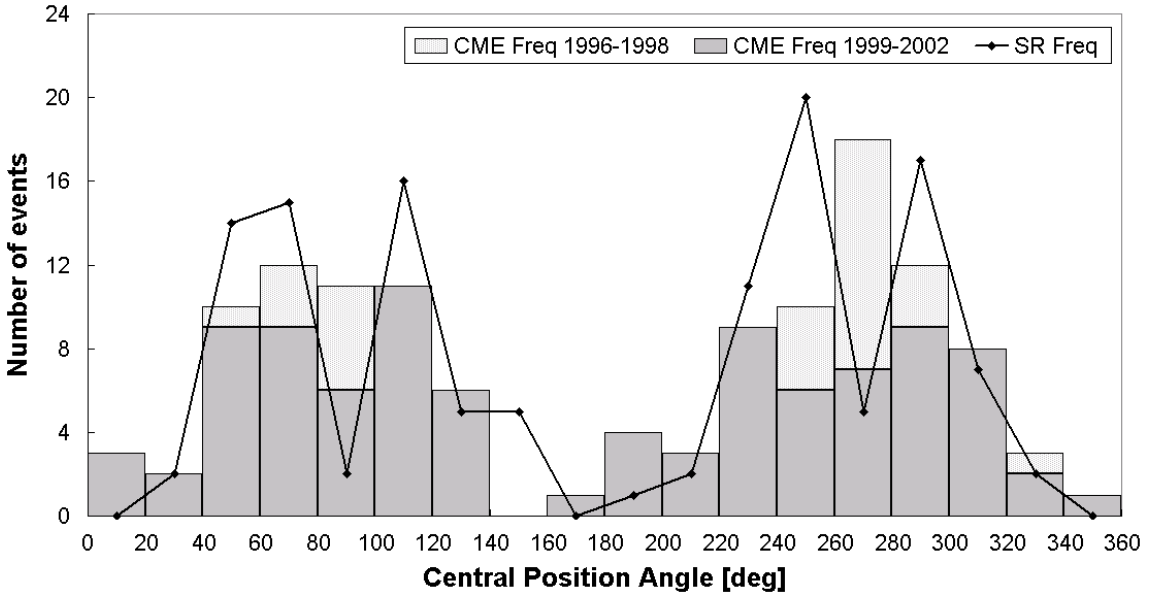

Figure 3.22. Distribution histogram of the structured CME central position angles (columns), in comparison with the SR central position angles (solid line) during 1996-2002, in bins of 20°. The CME PAs have been split in two time periods: 1996-1998 (light grey columns) and 1999-2002 (dark grey columns).

Despite the fact that the SR frequency peaks at PAs corresponding to the two activity belts (see Figure 3.22), the CME frequency concentrates at equatorial PAs (PA ≅ 90° and PA ≅ 270°). If one splits the columns into times of lower (1996-1998) and higher (1999-2002) solar activity periods, a two peak behaviour arises in the CME PA distribution, similar to that of the SRs. By comparing the PAs of the structured CMEs with those of their associated SRs, it was found that CMEs often do not travel radially outwards regarding the position of their source regions. An example showing deflection on June 2, 1998 is displayed in Figure 3.23. During solar minimum any solar wind outflow from the activity belts in each hemisphere is usually embedded in fast solar wind emanating from large polar coronal holes (e.g., Bothmer 1999). CMEs that originate during these times from the solar activity belts, and which possess a total plasma and magnetic field pressure not exceeding that of the surrounding flow, will get deflected towards lower latitudes thus explaining the CME PA confinement in times of low solar activity.

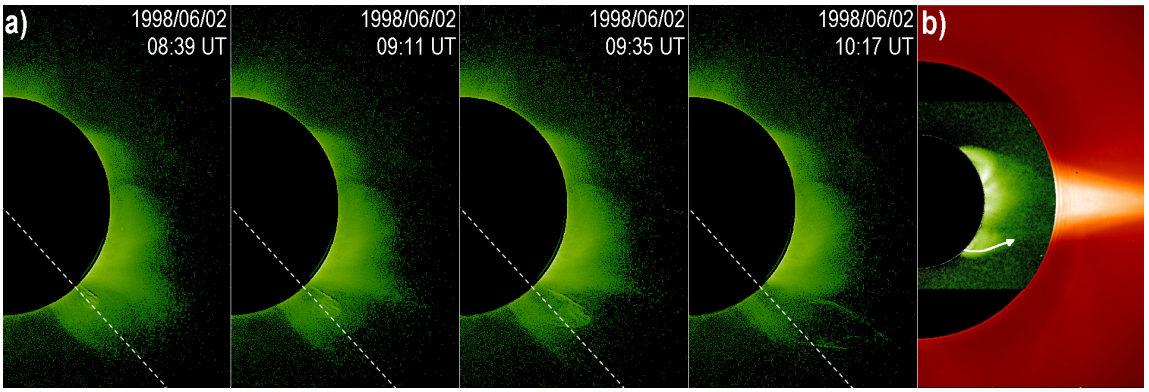

Figure 3.23. a) Temporal evolution of the CME on June 2, 1998 as captured by the LASCO/C1 coronagraph. The central PA of the SR was 222° (indicated by the dashed line), while that of the CME resulted to be 242°, as measured later in the LASCO/C2 coronagraph. Image processing courtesy M. Mierla. b) A LASCO C1/C2 composite image of the solar corona. The white arrow indicates the direction of CME deflection.

3.5.4 CME deflection

The discrepancy found between CME and SR position angles obviously results from the deflection of the outward-propagating CMEs with respect to the corona. Due to these possible interactions, CMEs appear often at PAs different from those of their SRs*.

The CME deflection δ has been quantified as the angular distance between the CME central PA and the PA of the source region's midpoint. The obtained values of δ (column 13 of Table 1) have been plotted in Figure 3.24 as a function of time. The inset in the figure indicates that positive values of the deflection angle δ correspond to equatorward-deflected CMEs, while negative ones correspond to poleward-deflected CMEs, always with respect to their SRs. Figure 3.24 shows that until mid 1998 (green circles) the structured CMEs were systematically deflected towards the equator in both hemispheres, though the second half of 1998 was unfortunately disrupted by the SOHO recovery phase. The average δ until mid 1998 was ~18°±10°. From January 2000 until the end of 2002 (red diamonds), the direction of deflection shows no systematic trend, with $\langle\delta\rangle$ = -4.4°±14°. CMEs deflected towards the equator showed commonly a smaller deflection angle and a number of CMEs was almost not deflected at all. Especially at times of solar activity maximum in 2000, about two thirds of the CMEs were deflected rather towards the poles, with δ oscillating around -7.1°. The year 1999 (yellow triangles) seems to have been an intermittent time period concerning CME deflection.

* Another outcome of the CME-ambient corona interaction is the modification of the CME shape, as ascertained from the distorted profile of some of the events listed in Table 1.

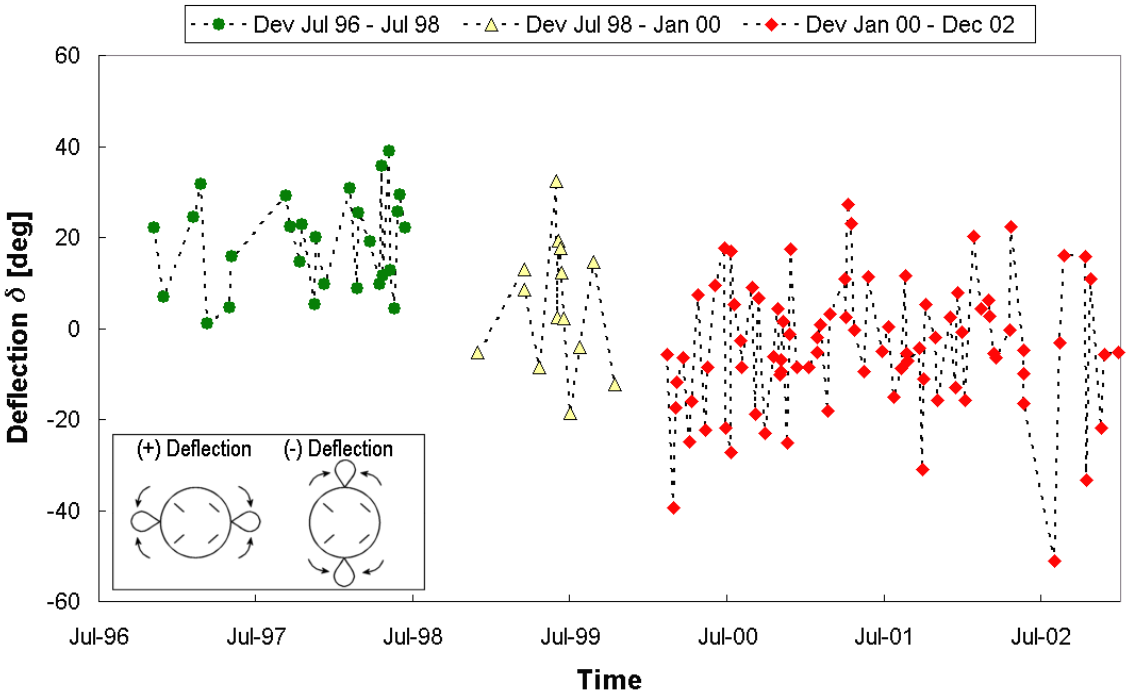

Figure 3.24. Deflection angle δ of each structured CME with respect to its associated source region as a function of time. Data points have been sorted into three time periods: Jul 96-Jul 98 (green circles), Jul 98-Jan 00 (yellow triangles) and Jan 00-Dec 02 (red diamonds). Positive values of δ correspond to CME deflections towards the solar equator, while negative values of δ correspond to deflections towards the poles.

3.5.5 CME deflection – relation to coronal holes

The temporal evolutions of the CME deflection and the total coronal hole (CH) area are compared in Figure 3.25. The total area of coronal holes during the corresponding Carrington rotation (derived from NSO/Kitt Peak He 10830 Å data), is given in percentage of solar surface. At times of low solar activity, a good correspondence was found between the CME deflection and the total area of coronal holes. It is possible that the presence of polar and neighboring CHs affects the outward evolution of CMEs near the Sun, as addressed by Schwenn (2000).

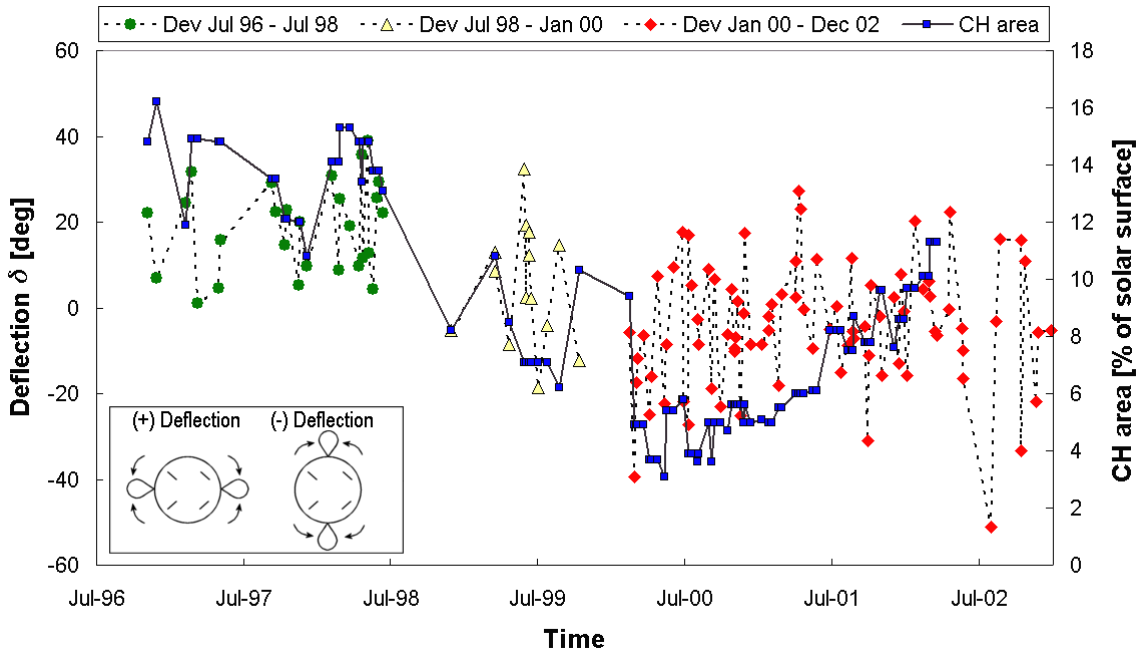

Figure 3.25. Deflection angle δ of each structured CME with respect to its associated source region as a function of time. Data points have been sorted into three time periods: Jul 96-Jul 98 (green circles), Jul 98-Jan 00 (yellow triangles) and Jan 00-Dec 02 (red diamonds). Positive values of δ correspond to CME deflections towards the solar equator, while negative values of δ correspond to deflections towards the poles. The temporal evolution of the total coronal hole area, provided by NSO/Kitt Peak He 10830 Å data, is displayed for comparison for the related Carrington rotations (blue squares on solid line).

In order to test our assumption on the effects of the CHs on the CME direction of propagation, we introduced the relation given in 4.1, based on the arbitrary force vector **F**. The process of interaction between CHs and CME expansion and direction of propagation needs to be investigated in more detail to understand more precisely the underlying physics. Certainly kinetic and magnetic pressures as well as magnetic interactions should be considered, which is beyond the scope of this study. The relationship introduced in 4.1 by means of the arbitrary force vector **F** is tested empirically. The quantity **F** is representative for the CHs' influence on the CME propagation direction, and accounts for the total deflection force exerted by the CHs on each CME source region. The vector **F** is considered to be directly proportional to the CH area, and inversely proportional to the distance from the CH to the source region's midpoint. The total **F** exerted by the neighbouring and polar CHs on an erupting CME is calculated as the sum of the individual contributions from each CH:

$$\mathbf{F} = \sum_i \frac{A_{CHi}}{|\mathbf{r}_{CHi}|} \cdot \mathbf{u}_{r_{CHi}} \qquad (3.1)$$

Where A_{CHi} stands for the area of the i-th CH and $|\mathbf{r}_{CHi}|$ for the distance to the i-th CH in the corresponding Carrington rotation (see example in Figure 3.26). The unity vector $\mathbf{u}_{rCHi}$ represents the direction of the radius vector $\mathbf{r}_{CHi}$. Since most of the structured CMEs originated from limb regions, only the elevation component of the net exerted force was taken into account. To analyze deflections in azimuthal direction, either a polar view onto the ecliptic is needed, which

will be achieved by future missions such as ESA Solar Orbiter or NASA Solar Probe, or stereoscopic views (primary goal of the forthcoming NASA STEREO mission, see Appendix).

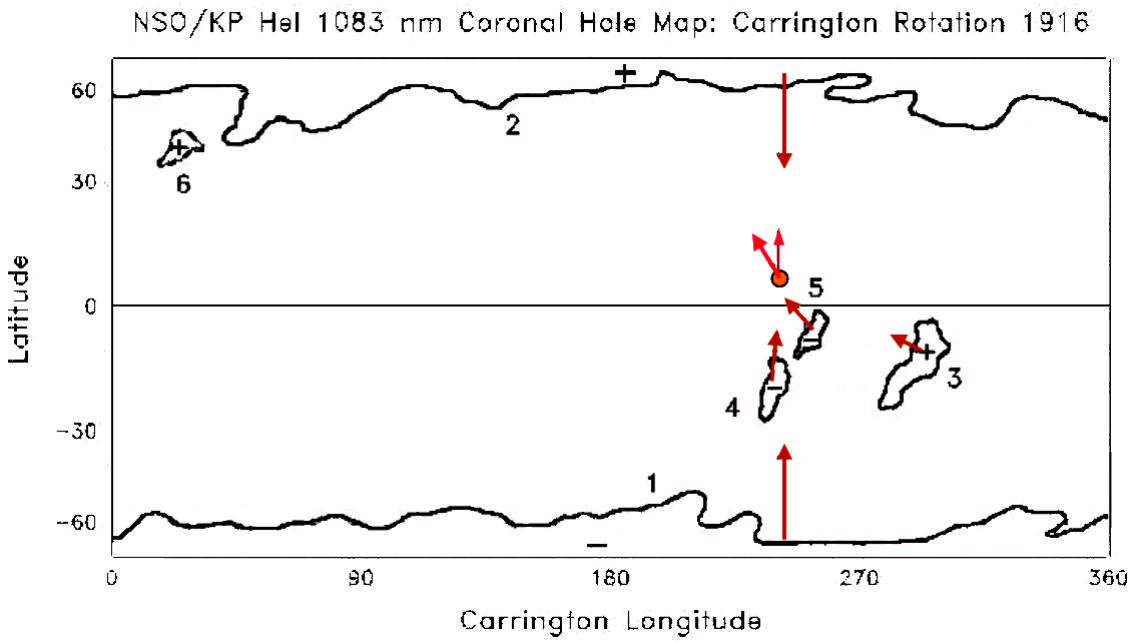

Figure 3.26. Synoptic coronal hole map for Carrington rotation 1916, provided by NSO/KP 10830 Å data. The forces exerted on the source region by the polar and nearby coronal holes are sketched with arrows. The bold pink arrow on the SR (here simplified to its midpoint) denotes the magnitude and direction of the net force **F**. The scenario corresponds to the SR of the structured CME on November 28, 1996.

For all the structured CMEs with identified SR, the elevation component of the net force **F** (F_{elev}) was calculated. It is compared with the deflection d of the structured CMEs in Figure 3.27. A positive sign in d and in F_{elev} represents an equatorward direction, while a negative sign stands for poleward directions. Additionally, the data points have been sorted into three time periods according to their behaviour evident in Figure 3. Out of the 62 events with positive d, i.e. deflection towards the equator, 41 (66%) coincided with a positive F_{elev}. On the other hand, out of the 48 events that exhibited negative deflections, i.e., towards the poles, 37 (77%) matched with negative F_{elev}. Figure 3.27 confirms the assumption that neighbouring and polar CHs play a major role in the deflection of CMEs. However, other factors are certainly involved as well. External sources of deflections, such as the presence of active regions may play a substantial role, especially at times of minimum solar activity. Intrinsic parameters of CMEs such as its magnetic field configuration and speed (Wang et al. 2004) should also be taken into account for the calculus of the CME deflection. In addition, projection effects may also bias the derived values for the CME deflection.

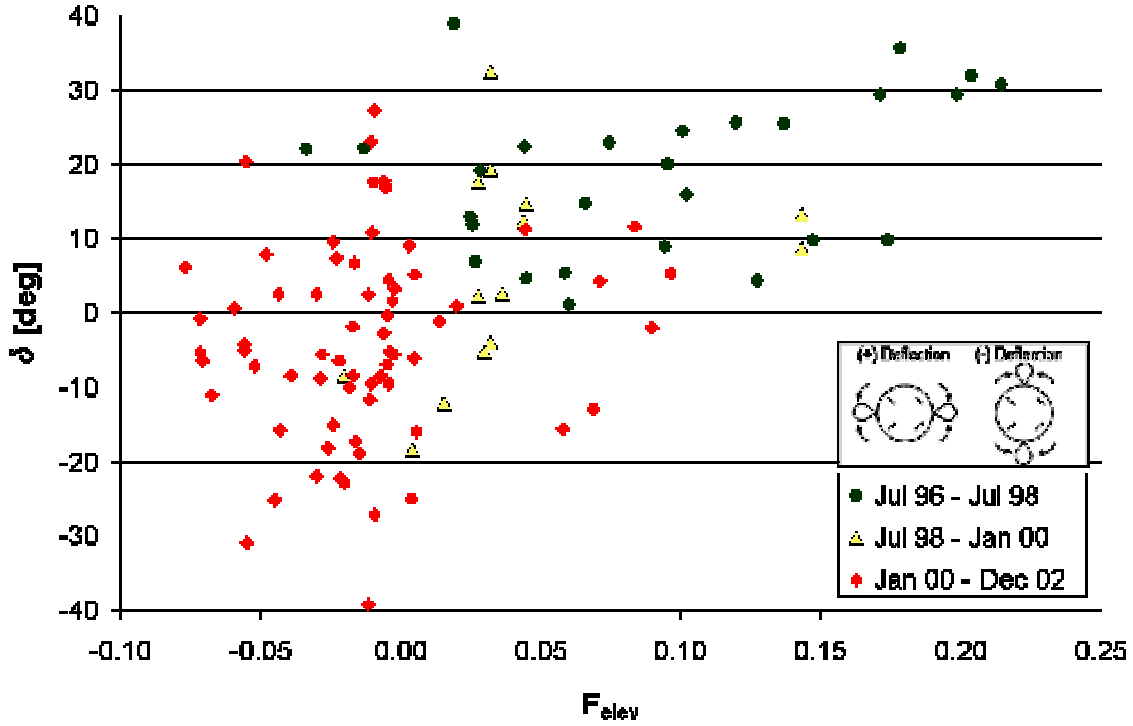

Figure 3.27. Dependence of deviation delta on the elevation component of **F**. The force **F** is directly proportional to the CHs' areas and inversely proportional to their distances to the source region. The upper inset indicates that equatorward CME deviations correspond to positive values of *d*, while poleward deviations correspond to negative ones. The lower inset denotes the symbols used for the three different periods of time in which the data have been sorted according to their behaviour.

3.6 The Scheme of 3D CME configuration

Although early studies considered the possibility of CMEs as being simply planar loops (e.g., Trottet &MacQueen 1980), that idea was abandoned after later analyses which supported shell-like configurations (e.g., Webb 1988, 1998). Still under debate is the question whether the 3D configuration of CMEs resembles more an arcade of loops, a curved flux rope, or a bubble-like shape with symmetry of rotation. Studies committed to answer this question based on observational properties of CMEs include, e.g., Crifo et al. (1983), Schwenn (1986), MacQueen (1993), Plunkett et al. (2000), and Zhao et al. (2002). Other efforts have been directed towards the attainment of 3D MHD models that describe the initiation, expulsion out of the corona, and evolution of the classic three-part structure CME (e.g., Gibson & Low 1998; Amari et al. 2000). Below, an approach based on the analysis of observational characteristics of CMEs and their source regions attempts to infer their 3D nature.

3.6.1 Comparison of CME features and SR properties

Each structured CME-SR pair was investigated for similarities between magnetic structures apparent in the low corona at EUV wavelengths and in white-light in the FOV of LASCO C2. The evolution of the structured CME on January 4, 2002 can be followed in Figure 3.28. It begins with the rise of the prominence and surrounding loops at around 09:12 UT in EIT, and develops further into the FOV of C2 at ~9:40 UT. In the left frame of Figure 3.28 a, the

prominence is observed to lie almost perpendicular to the line of the limb, i.e., perpendicularly to the line of sight. This prominence also appears to be located underneath a loop system which grows in size as the prominence rises and lifts off (mid and right frames of Figure 3.28a). This structured CME is a typical three-part CME. The dark cavity, embedded by the bright leading edge and trailed by prominence material, is often interpreted as the site of a magnetic flux rope (Chen et al. 1997; Dere et al. 1999; Hundhausen 1999; Wood et al. 1999; Gibson & Low 2000). The physical existence of large-scale expanding helical flux ropes is supported by satellite observations of magnetic clouds in the solar wind and their association with disappearing filaments (e.g., Bothmer & Schwenn 1998), as well as by theoretical models (e.g., Low 2001). In Figure 3.28b, the generic structure of the core material of the CME later seen in C2 matches the structure of the erupting prominence in EIT, and the growing loops above the prominence correspond with what later is referred to as the leading edge of the CME. A closer look at the source region may be attained by superposing MDI and EIT images from two days after the event when the CME's SR appeared on the visible disk. This composite image is displayed in Figure 3.28c, showing that the filament originated from a filament channel that lay along the neutral line separating opposite polarities. The whole system was oriented almost perpendicular to the line of the limb.

However, when the neutral line is approximately parallel to the line of the limb as indicated by the post eruptive arcade in Figure 3.29a and by the neutral line evident in Figure 3.29c, the shape of the subsequent CME is essentially different (Figure 3.29b). In this case, a linear feature parallel to the limb and a broad, diffuse inner core are evident. The generic structure of this CME in C2, apparent as a side-viewed prominence/overlying loop system, can be identified already in the EIT images, supporting the assumption of self-similar expanding structures.

The two structured CMEs shown in Figure 3.28 and Figure 3.29 exhibit archetypical features representative for most of the events collected in Table 1. These basic characteristics can be interpreted through expanding loop systems with cylindrical symmetry agreeing with the magnetic flux rope nature evident in some events (see Figure 1.13). Based on this interpretation, the two complementary cases of Figure 3.28 and Figure 3.29 show a CME from two very different perspectives. In the case of Figure 3.28, the CME is observed along its symmetry axis, while in the event of Figure 3.29 the line of sight is perpendicular to the symmetry axis.

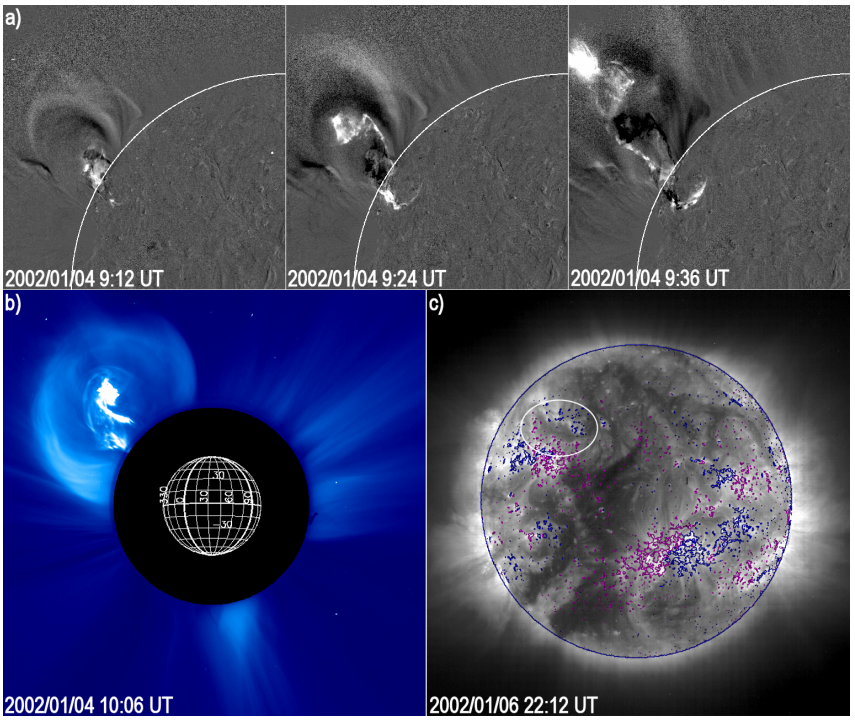

Figure 3.28. Structure and evolution of the CME on Jan 4, 2002. a) EIT running difference images of the prominence eruption. b) The resulting CME as seen by LASCO/C2. The FOV has been cropped to focus on the CME. c) Contours of an MDI magnetogram superposed onto the EIT 195 Å low coronal image, from observations taken 2 days after the eruption, when the SR (encircled) became visible on the disk. Magenta contours represent positive polarities, while blue contours represent negative ones.

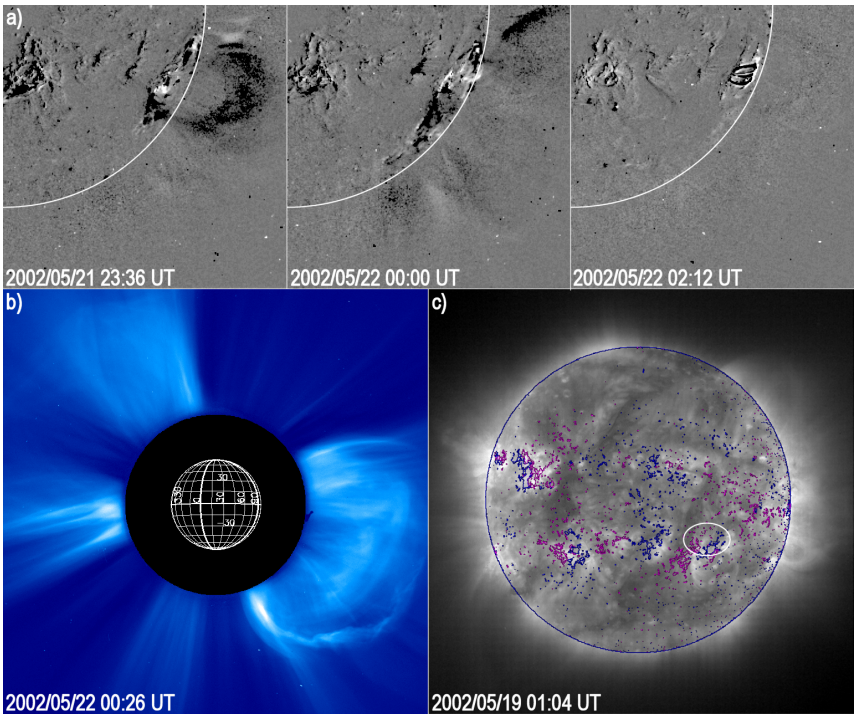

Figure 3.29. Structure and evolution of the CME on May 22, 2002. a) EIT running difference images of the rising loops. b) The resulting CME as seen by LASCO/C2. The FOV has been cropped to focus on the CME. c) Contours of an MDI magnetogram superposed onto the EIT 195 Å low coronal image, from observations taken 3 days before the eruption, when the SR (encircled) was still visible on the disk. Magenta contours represent positive polarities, while blue contours represent negative ones.

Assuming that the typical orientation of the neutral lines follows Joy's Law (see Subsection 3.4.3), for front-side cases close to the east limb, the neutral lines would be approximately perpendicular to the limb, whereas for cases near the west limb the neutral lines would be roughly parallel to the line of the limb on average. This implies that front-sided CMEs originating from near the east limb would be prone to be seen along their symmetry axis, while the ones from near the west limb would tend to have their axes oriented perpendicular to the line of sight, as sketched in Figure 3.30a. The examples selected out of Table 1 show perfect cases of these two types of projected CMEs in Figure 3.30b. East limb CMEs have their core material concentrated along the line of sight and show clear three-part structure. On the other hand, west limb CMEs have their core material extended and perpendicularly oriented to the line of sight. Figure 3.30c presents the EUV SRs associated with the corresponding CMEs of Figure 3.30b. The two cases in the northern hemisphere show eruptive features being self-similar to the CME structures observed later in C2, while the two southern ones depict post-eruptive arcades perpendicular to the limb in the East case and parallel to it in the West case. It must be noted that the described picture in Figure 3.30 reverses for far-sided CMEs near the limb (Figure 3.31) because the orientation of the neutral lines with respect to the observer is reversed in this case.

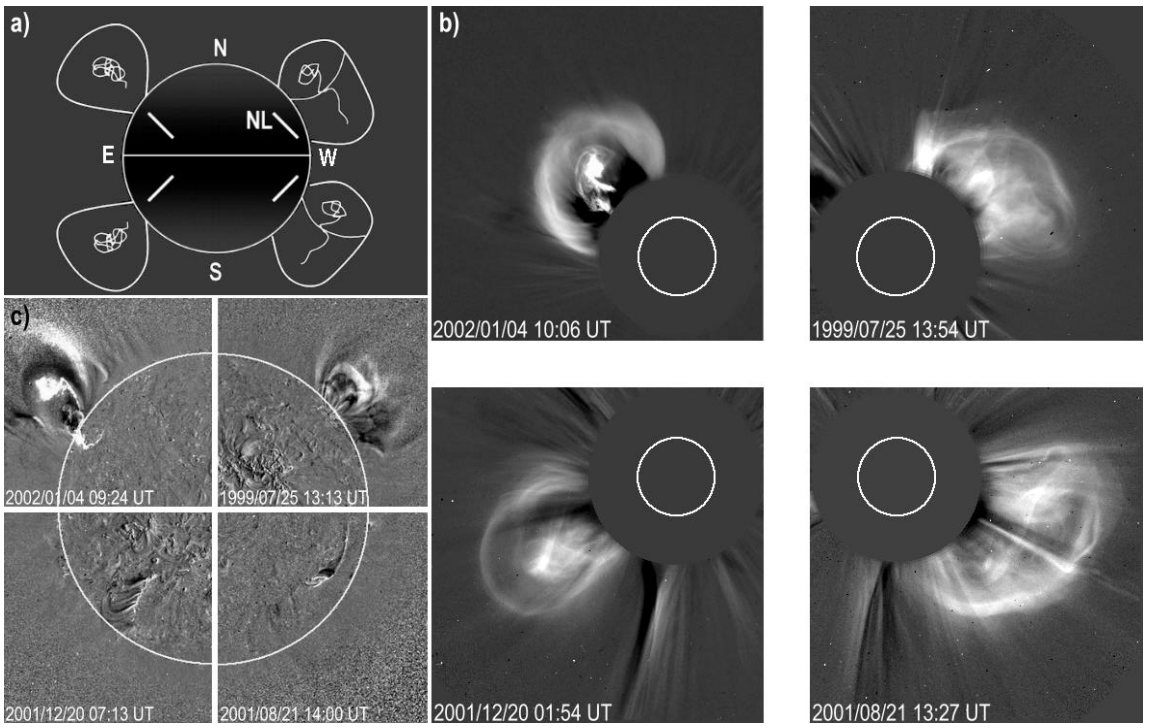

Figure 3.30. a) Simplified scheme depicting the extreme cases of CME projection for front-side events. NL stands for neutral line. b) Examples of four projected LASCO/C2 CMEs matching the basic scheme. c) Source region features of the CMEs shown in b). Eruptive features are shown in the northern hemisphere, and post-eruptive arcades in the southern.

The topology of the white-light structured CMEs can be considered under general circumstances as consistent with the orientation of the neutral line and its position on the solar disk. Column 14 of Table 1 specifies for each event whether the orientation of the SR matched the expected CME shape approximated by a straight or curved axis of an imaginary cylinder. For 94 out of the 124 selected structured CMEs (76%; including backside events) such an agreement was found. This finding suggests that CMEs can be interpreted as three-dimensional magnetic field entities whose global configuration agrees with the characteristics of the underlying photospheric SR geometry,

with its loops or flux ropes expanded into the low corona. It should be noted here that this interpretation is independent of the existence of U-shaped white-light features, considered by some authors as to outline the flux rope when it is oriented along the line of sight (Chen et al. 1997; Wood et al. 1999). Because of the concave-up nature of magnetic field lines in flux ropes, in principle U-shaped features may also be visible for flux ropes highly inclined with respect to the line of sight (Gibson & Low 2000; Gibson et al. 2004). The neutral line location and its orientation play a crucial role in determining the topology of the projected CME in C2, but other factors may also affect it as experienced from the inspection of the collection of structured events. This finding might be anticipated from the scheme depicted for structured CMEs in Figure 3.30, if one takes variations of the initial conditions into account.

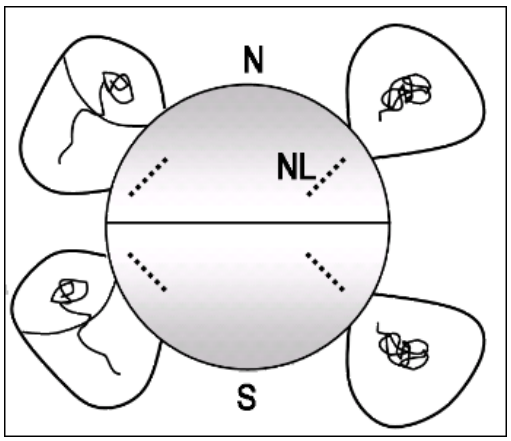

Figure 3.31. Simplified scheme depicting the extreme cases of CME projection for backside events. The neutral lines (NLs) are dotted in this case, indicating their far-side locations.

3.6.2 Complications to the scheme

The ideal view presented in Figure 3.30 and Figure 3.31 is based on cases with typical hemispheric orientations of the SRs. However, in reality the apparent profile of a CME may differ more or less from the basic scheme because of the variability and complexity of the parameters involved in the shaping of a CME. Altogether these factors, which are apparent from solar observations, imply the existence of complicated configurations and deflections from the basic CME scheme. For instance, the scheme assumes the general orientation of neutral lines as 45° tilted from the north-south line. Even though 45° is the average value of the tilt γ in both hemispheres, the various inclinations range from almost horizontal to nearly vertical, as already presented in Subsection 3.4.3. The scatter of γ will yield intermediate cases of projected CMEs, whose structure in C2 will be a combination of the two basic views, ranging from being purely aligned along the line of sight or perpendicular to it. There are other complicating factors also related to the SRs themselves. Many neutral lines often cannot be represented by fairly straight lines, having rather complicated topologies, especially in active regions (see Figure 3.32). Further, the loops overlying SRs may undergo considerable shear motions, which may affect CME orientations by means of rotations.

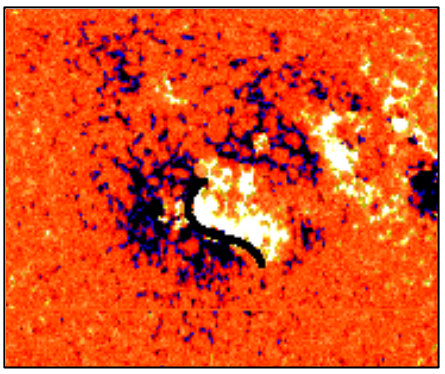

Figure 3.32. Example of a considerably curved neutral line, separating opposite polarities in an active region. The image corresponds to an MDI synoptic chart (Carrington rotation 1955), cropped to focus on the SR.

The dynamics of prominences can exhibit various levels of complexity (e.g., Tandberg-Hanssen 1974), and may also contribute to complicate the simple configuration suggested by the scheme. Prominences do not always rise uniformly, as one of the legs seems to detach and rise before the rest of the prominence material lifts off (see Figure 3.33), leading eventually to alterations of the expected C2 white-light profile.

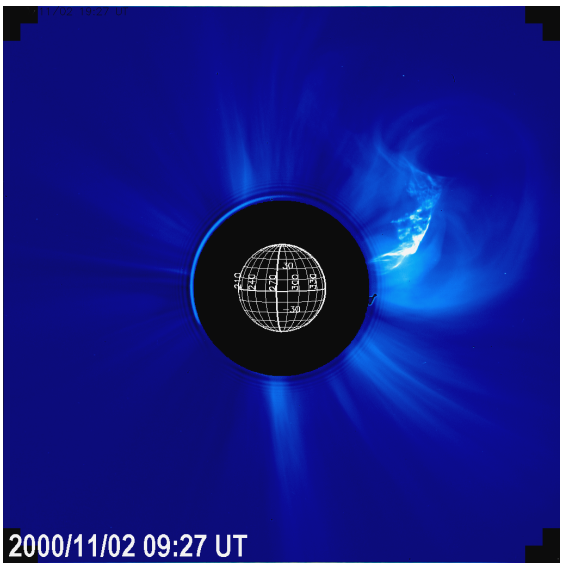

Figure 3.33. The structured CME on June 2, 2000 as seen by LASCO/C2. One of the prominence legs rose before the other one, distorting the shape predicted by the scheme of 3D configuration.

The CME scheme implies a relationship between the length of the SR and the AW of the corresponding CME. To investigate this dependence, the SR lengths of neutral lines closely parallel to the west limb were compared with the AWs of the respective CMEs in Figure 3.34. These events are indicated by a superscript *b* in Table 1, and are expected to yield CMEs with their core material aligned perpendicularly to the line of sight, as in Figure 3.29. The data points plotted in Figure 3.34 show considerable scatter, though it is possible to trace a linear fit through them. The scatter of the data points may be partially attributed to projection effects still present in the measured AWs of the CMEs.

Another aspect that can lead to the dilution of the trend arises from Figure 3.35. There, the ratio between AW and SR length of each particular structured CME has been plotted as a function of the SR length. SRs shorter than 10° produced CMEs at least seven times wider than their SRs, whereas SRs longer than 15° generated CMEs whose AWs were less than seven times the length of their SRs. A power-law fit yields $AW/Length_{SR} = 85\ Length_{SR}^{-1}$, in direct agreement with the average AW of 85° found in Subsection 3.3.2. On the whole, the longer the SRs, the less that the produced CME seems to expand with respect to its SR length. The longest SRs are found in

magnetically decaying regions, which do not seem to produce wide spreading CMEs, while some small source regions did produce some very impulsive, wide spreading CMEs.

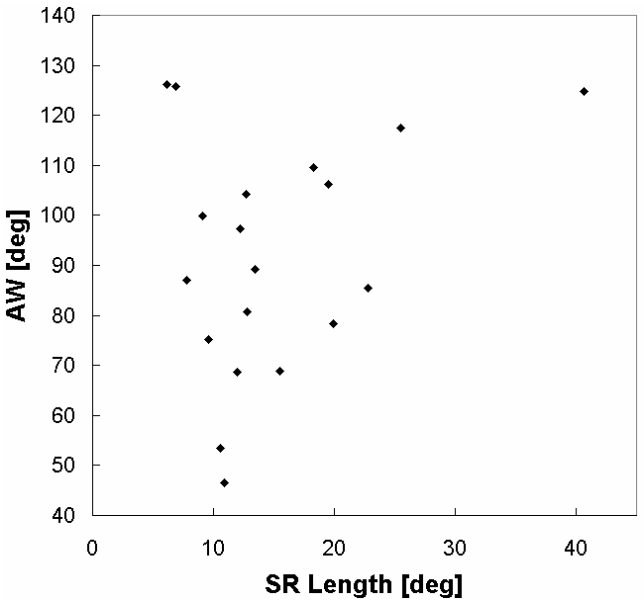

Figure 3.34. AW of structured CMEs as a function of the associated SR Length, for cases in which the neutral line was parallel to the limb.

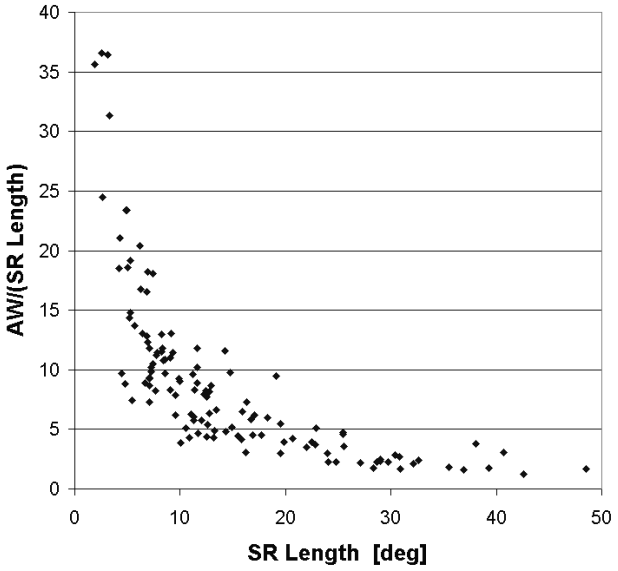

Figure 3.35. Ratio between AW and SR Length of the 124 structured CMEs, as a function of the SR Length.

An additional factor that plays a role in the 3D CME configuration is also related with the SR length. In general the events presented in Table 1 reveal that the cylindrical geometry presented in the scheme of Figure 3.30 especially matches CMEs with large SR lengths, which are typically found in decaying regions that are preferentially located at higher latitudes. On the contrary, CMEs associated with shorter neutral lines, especially those of newly-developed rather compact active regions, showed a lower degree of correspondence and a more bubble-like shape. The correspondence with the scheme of the 124 structured CMEs, as a function of the SR length, has been summarized in the histogram presented in Figure 3.36. The columns have been coloured according to the degree of correspondence, in purple (agreement), blue (not clear agreement), and light purple (compact system). Further, the numbers on top of the columns indicate the percentage of events in each bin, which showed disagreement. It is evident from the figure that the bins with higher percentage of disagreement are those related with the shortest SRs.

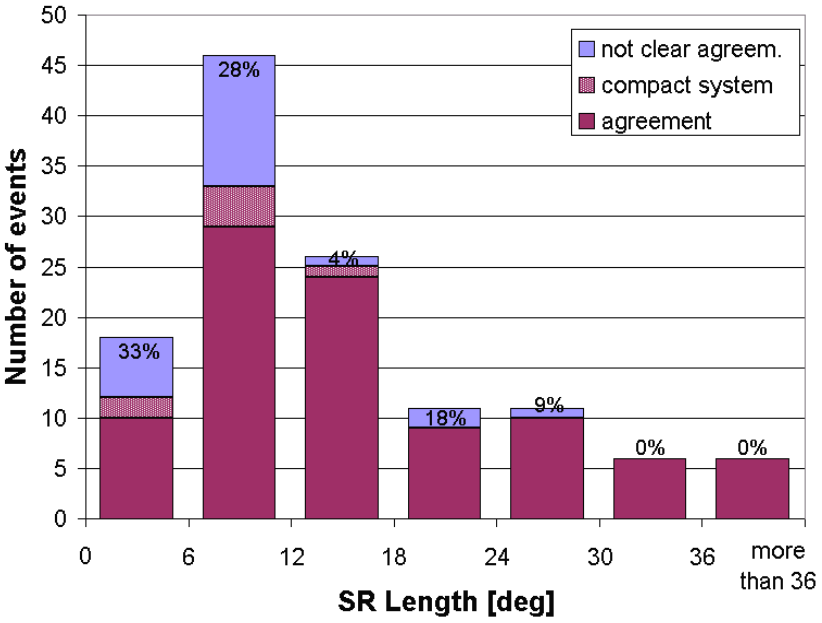

Figure 3.36. Frequency histogram of the SR Length, in bins of 6 degrees. The columns have been coloured according to the degree of correspondence with the scheme, detailed in the inset. The percentages indicate the fraction without clear agreement.

The interaction with the ambient corona as a CME propagates outward is another important issue. In their journey across the coronagraph FOV, CMEs feel the effects of the corona in which they are immersed. This may lead, on the one hand, to deflections of the ambient corona, especially in the case of very explosive events. These events have presumably high internal pressure, leading to substantial expansion. On the other hand, the presence of coronal holes and active regions in the vicinity of SRs may lead to deflections and changes of PA (discussed in Subsection 3.5.4). Other effects of the corona-CME interaction are distortions and significant changes in shape, observed in a number of CMEs as they propagate.

3.6.3 Typical dimensions of structured CMEs

The generic scheme for the 3D CME configuration deduced in Subsection 3.6.1 considers the projected profiles of CMEs as mainly dependent on their SR locations and orientations, regarding CMEs as cylindrical entities (supported also by the recent study of Moran & Davila 2004, based on a polarization analysis). This approximately cylindrical symmetry implies the existence of a main axis, consistent with the alignment of the filamentary material constituting the CME's core, and raises the question of whether the AWs of CMEs seen along their symmetry axis differ from those seen perpendicularly to it. In order to investigate how alike the AWs of these two views are, the structured CMEs exhibiting the two purest cases of projection –seen along their axis or perpendicular to it– were identified from the set of 124 structured CMEs. Examples of the two cases of projection are depicted in Figure 3.37.

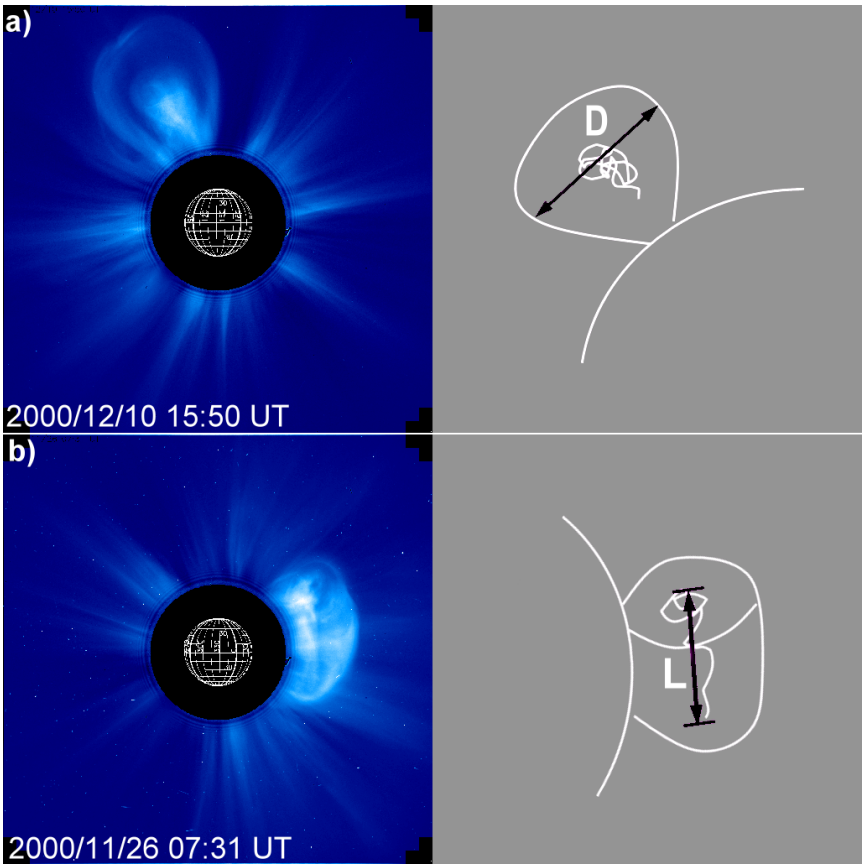

Figure 3.37. Two structured CMEs seen in extreme projection in LASCO/C2 (left) and schematic views (right). a) main axis primarily oriented along the line of sight, i.e. CME seen in cross-section with diameter D. b) main axis L oriented perpendicular to the line of sight.

As sketched in Figure 3.37, the angular width "*D*" of the axial cases indicates the diameter of the imaginary cylinder's cross-section (Figure 3.37a), while the width "*L*" of the events observed perpendicular to their axis denotes the length of the imaginary cylinder's axis, most likely aligned with the extended prominence material (Figure 3.37b). Since it is unlikely to find CMEs exactly oriented parallel or perpendicular to the line of sight, to measure the widths *D* and *L* a different strategy than the one used for the AWs was employed. In the case of the AW, it is delimited by the outermost edges of a CME (see Subsection 3.3.2). However, the width *D* is measured as the width of the cavity, without considering the bright outer rim; and *L* as the extension of the bright, extended feature typical of events oriented perpendicular to the line of sight.

The widths of *L* and *D* were measured once more in LASCO/C2 and, if possible, in EIT 195 Å images as well. Altogether, 16 events were identified as seen along their axis, out of which 9 were also measurable in EIT 195 Å, and 17 events were found to be seen perpendicular to their axis, out of which 9 were measurable in EIT 195 Å. The 33 structured events have been compiled in Table 2. The columns on the left refer to events oriented along the line of sight, while the columns on the right contains events oriented perpendicular to it. For each of the two groups CME date and time are given, the width of *D* (or *L*) in EIT if possible, and the width of *D* (or *L*) in C2. The quantities *D* and *L* were measured at average heights of 1.3 and 4 $R_{\odot}$, in EIT 195 Å and LASCO/C2 respectively.

Table 2. Structured CMEs from Table 1 that exhibit extreme projection. Left: along the line of sight. Right: perpendicular to the line of sight. Columns 1 and 4 indicate date and time of CME appearance in the FOV of LASCO/C2. Columns 2 and 5 give widths of D and L in the FOV of EIT, and columns 3 and 6 in the FOV of LASCO/C2.

CME date and time (UT) (1)	**D** in EIT (deg) (2)	**D** in C2 (deg) (3)	CME date and time (UT) (4)	**L** in EIT (deg) (5)	**L** in C2 (deg) (6)
97 Mar. 09 04:30		32	97 Apr. 30 04:50	23	32
97 Sep. 09 20:06	12	41	97 Oct. 12 06:26	22	27
97 Nov. 18 08:27		32	97 Dec. 06 10:27		69
98 Feb. 24 07:28		29	98 Feb. 04 17:02		26
98 Jun. 02 08:08	10	39	98 Apr. 20 10:07		68
99 May 30 11:06		40	99 Jul. 25 13:31	15	51
00 May 15 08:50	21	46	00 Feb. 13 22:06	28	56
00 Dec. 10 03:26		30	00 Jun. 27 10:54	16	33
01 Jan. 26 16:06	8	37	00 Aug. 02 17:54	25	63
01 Apr. 23 19:09		29	00 Sep. 12 11:54		80
01 May 15 18:52	18	46	00 Nov. 26 06:30		66
01 Jul. 23 11:08		33	01 Jul. 12 00:06		56
01 Aug. 19 06:06	15	41	01 Aug. 21 12:06		61
01 Dec. 20 00:30	17	33	01 Nov. 01 14:30	17	47
02 Jan. 04 09:30	13	47	01 Dec. 28 20:06	32	70
02 Aug. 13 08:54	16	38	02 Mar. 18 02:54		105
			02 May 22 00:06	24	68

The widths of *D* and *L* derived from the analyzed events in Table 2 were compiled in histograms, displayed in Figure 3.38. Each histogram shows in two different levels of grey the values measured in the EIT 195 Å and LASCO/C2 FOVs. Although limb CMEs seem to keep their AWs from the FOV of LASCO/C2 and further out, there is a marked difference between the widths measured in EIT 195 Å and in LASCO/C2, supporting the assumption that the CME's greatest expansion takes place already between 1 and 2.5 solar radii, i.e. into the transition from closed to open coronal fields (e.g., Wang et al. 2000; Abbo et al. 2003). The averages of *D* in EIT 195 Å and in LASCO/C2 were 14°±4° and 37°±6°, while the larger averages of *L* in EIT 195 Å and in LASCO/C2 yielded 22°±6° and 58°±20° respectively[*]. The rather distinct average widths in EIT 195 Å (14° for *D* against 22° for *L*) and in LASCO/C2 (37° for *D* against 58° for *L*) reveal an asymmetry between the axial direction and the perpendicular one. The ratio *L*/*D* allows the comparison of the averages of *D* and *L* of the imaginary cylinder, yielding the value of 1.6±0.6 in both cases, EIT and LASCO/C2. The invariability of the ratio *L*/*D* in EIT and LASCO/C2 for this particular set of events, may be a sign of self-similar expansion, addressed by some theoretical models (e.g., Gibson & Low 2000).

[*] The error is given by the standard deviation of the values, which measures their dispersion with respect to the average.

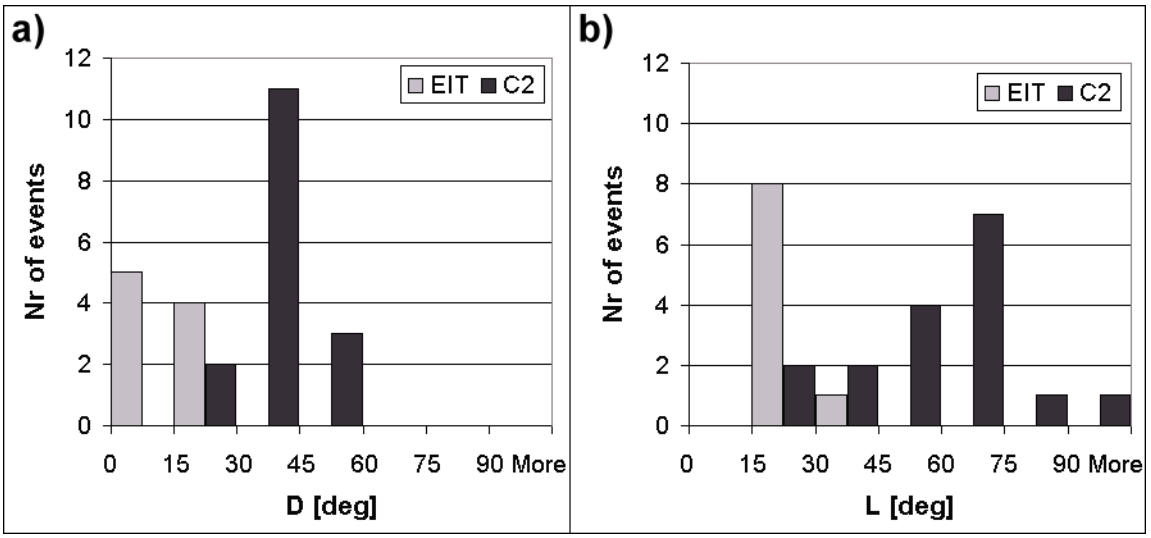

Figure 3.38. Width distribution histogram of the CMEs seen in extreme projection. Light and dark grey columns indicate measurements carried out in the EIT 195 Å and LASCO/C2 FOVs respectively. a) Main axis primarily oriented along the line of sight. b) main axis aligned perpendicular to the line of sight.

The arcade-like rather than bubble-like structure derived from the basic scheme implies an essential difference in the profiles projected onto the plane of the sky, depending on the arcade's orientation with respect to the observer. If the arcade is approximated by a cylinder, the measured widths of its cross-section *D* and length *L* can be substantially different. It is expected that halo CMEs will present cases of asymmetry as well, as a consequence of the imprints of source region characteristics. Halos entirely seen from top, i.e. originating from exactly the centre of the solar disk, shouldn't then look completely circular, but rather elliptical. The next chapter looks forward to find such a discrepancy between *D* and *L* in halo CMEs.

Chapter 4 The Elliptical Cone Model

4.1 Introduction

Those cases of structured CMEs seen in extreme projection, i.e. seen approximately along their axis or perpendicular to it, have been identified in Subsection 3.6.3. The distinct averaged widths found for these two groups revealed an asymmetry between the axial direction and the perpendicular one, with a ratio of $L/D \cong 1.6$. Based on these results, it is expected that halo CMEs will also present cases of asymmetry, i.e. the outer edge of some halo CMEs travelling in the Sun-Earth direction should appear elliptical instead of circular.

The circular cone model introduced by Zhao et al. (2002) approximates CMEs as cones with circular base. The basis of a circular cone with vertex in the Sun and oriented in any direction, projects typically an ellipse on the plane of the sky. For this reason, the appearance of elliptical full halos in LASCO/C2/C3 could merely be the result of projection effects, of intrinsically circular halo CMEs travelling in other directions rather than exactly the line of sight. The circular cone model from Zhao et al. (2002) could not fit a substantial number of halo CMEs. This result suggests the existence of real elliptical halos, observed as such not only as an effect of projection. In order to prove the existence of asymmetric halos, an elliptical cone model was developed as an improvement to the cone model, in an effort to reproduce a set of bright, front-side halo CMEs detected by LASCO. The contents of this chapter are based on the findings presented in Cremades & Bothmer (submitted to Proc. of IAU Symposium 226 on Stellar and Coronal Mass Ejections).

4.2 The model

The circular cone model presented by Zhao et al. (2002) (henceforth referred to as Zhao's model) has served as foundation for the development of the elliptical cone model presented in this chapter. The motivation of Zhao's model is to obtain the "real" angular width (AW) and direction of propagation of a halo CME, by fitting its outer edge with the base of a circular cone projected on the plane of the sky according to its orientation. Zhao's model assumes that CMEs propagate almost in a radial direction after the first solar radii, i.e. in the FOVs of LASCO C2 and C3. Additionally, the angular widths of CMEs are considered to be constant, suggested by the almost invariable AWs of limb CMEs (e.g., Webb et al. 1997) and the similar AWs of their interplanetary counterparts (Webb & Jackson 1990). It is also assumed in Zhao's model that the width of a CME is essentially the same when measured in perpendicular directions, i.e. its cross-section is circular.

Another model that considers cones as good proxies of CMEs is the well-known ice-cream cone model developed by Fisher & Munro (1984). However, in order to resemble the distribution of observed polarized brightness the modelled CME is restricted to travel in the plane of the sky.

The model of Michalek et al. (2003) is similar to that of Zhao in the sense that it also regards CMEs as symmetric cones with constant speeds and AWs. The technique to calculate the free parameters is yet different, since it requires measurements of sky-plane speeds of halo CMEs above opposite limbs. The nature of Zhao's model makes straightforward its modification towards an asymmetric cone with an elliptic instead of a circular cross section.

4.2.1 Zhao's circular cone model

Zhao's model considers a CME with the shape of a cone of circular cross section, whose central axis is oriented in the positive X_c-direction (see Figure 4.1). Its vertex coincides with the origin of the coordinate system, also the location of the Sun. The half angular width of the cone is w, while the slant height of the cone is given by s. The slant height s is related to the radial distance r by: $r = s \cdot \cos(w)$, measured from the origin to the base of the cone. Accordingly, the cone of circular cross section is given by the following set of equations, which arise after a straight transformation from spherical coordinates:

$$\begin{aligned} X_c &= s \cdot \cos(w) \\ Y_c &= s \cdot \sin(w) \cdot \cos(d) \\ Z_c &= s \cdot \sin(w) \cdot \sin(d) \end{aligned} \qquad (4.1)$$

Where the X_c axis is aligned with the central axis of the cone and origin in its vertex, and Y_c and Z_c are orthogonal to X_c and between themselves. The subscript c refers to the conic geometrical figure. The parameter d varies from 0° to 360°.
The result is a cone with circular base and vertex in the Sun, considered as a punctual object.

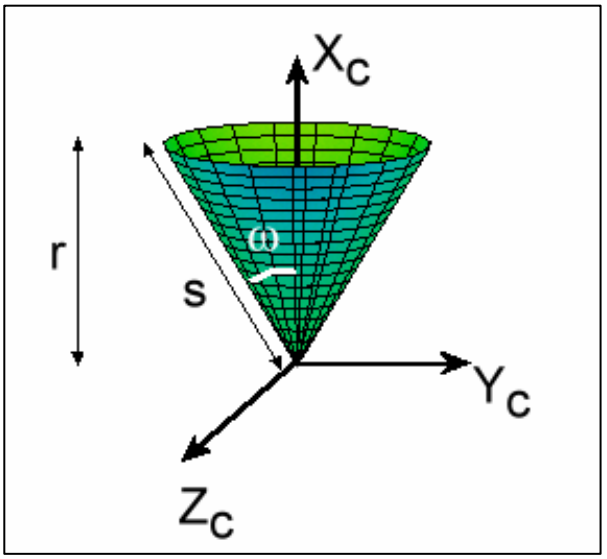

Figure 4.1. A circular cone in its coordinate system. The axis X_c is aligned with the central axis of the cone, and the axes Y_c and Z_c are orthogonal. The half AW of the cone is given by ω, while r and s are the radial distance and the slant height respectively.

Given w and s (or r), a specific cone is generated, described by X_c, Y_c and Z_c. The cone will be oriented with respect to the observer according to the direction of propagation of the CME, i.e. according to the orientation of X_c. The projection of the cone's base on the plane of the sky, depending on the cone's main axis orientation, is given by the transformation from the cone's coordinate system into the heliographic coordinate system. The latter originates at the Sun's center, with X_h pointing towards the Earth, Z_h being northward directed, and Y_h westward. In this

manner, the plane Y_hZ_h represents the plane of the sky. If the Y_c axis is positioned in the plane X_hY_h, then the projection of the cone's base in the plane of the sky (Y_hZ_h) is given by:

$$\begin{aligned} Y_h &= X_c \cdot \cos(l) \cdot \sin(f) + Y_c \cdot \cos(f) - Z_c \cdot \sin(l) \cdot \sin(f) \\ Z_h &= X_c \cdot \sin(l) + Z_c \cdot \cos(l) \end{aligned} \tag{4.2}$$

Here the heliographic latitude l and longitude f determine the orientation of the main axis of the cone, X_c. In Zhao's model, the three free parameters w, l and f can be uniquely determined by reproducing the outer edge of a halo CME with the base of the circular cone projected at a given distance r. Examples are given in Figure 4.2. If it is the case that the cone's main axis is exactly aligned with the line of sight (l = 0, f = 0), there are infinite solutions, so that a faster but narrower CME may produce the same outer edge as a slower and wider CME.

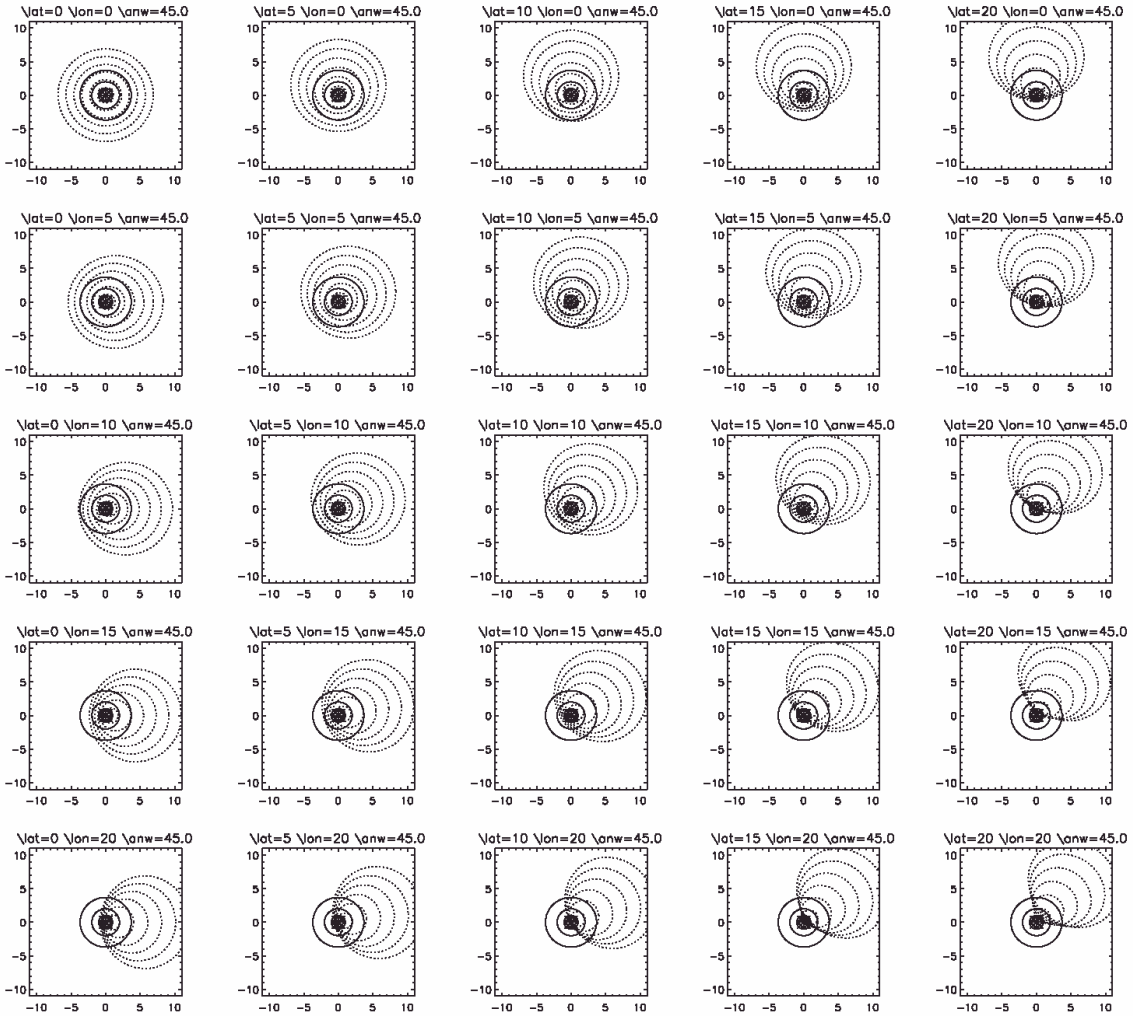

Figure 4.2. Halo CMEs reproduced with Zhao's model (dotted lines). The full lines represent the occulters of LASCO C2 and C3, while the innermost circle denotes the solar disk. The spatial scales are given in solar radii. The latitude increases from left to right, whereas the longitude increases from top to bottom, both in steps of 5 degrees. The AW is 45° in all 25 cases. The six dotted lines in all cases correspond to radial distances of 3, 6, 9, 12, 15 and 18 solar radii. Adapted from Zhao et al. (2002).

Zhao's model demonstrates that the result of projecting the base of an arbitrarily oriented circular cone on the plane of the sky yields usually an ellipse, whose eccentricity becomes more pronounced as the latitude and longitude increases. The existence of apparently elliptical halos (as shown later in Figure 4.7) may then just be the result of projection effects. However, when Zhao's model was applied to the set of halo CMEs described in Section 4.3, a number of events could not be fitted. This finding supports the assumption that CMEs may be approximated by cones with elliptical bases, and led us to further develop Zhao's model into the elliptical cone model.

4.2.2 The elliptical cone model

The elliptical cone model employs a nomenclature very similar to that employed in Zhao's model, and incorporates new additional variables. In this case we consider a cone with elliptical cross section, as can be seen from the three-dimensional sketch in Figure 4.3. In order to generate an elliptical cone, not only one half-AW (w) of the cone is needed, but two: one for the direction of the semi minor axis and another one for the semi major axis, called w_a and w_b respectively (see Figure 4.3 b and c). From these two half-AWs arise the two slant heights s_a and s_b, which are related by the condition: $s_a \cdot \cos(w_a) = s_b \cdot \cos(w_b) = r$. The fact of producing an elliptical base involved the insertion of the new variable c, which defines the tilt of the semi major axis with respect to the Y_c axis (see Figure 4.3a). The equations that define the cone in its own coordinate system are given by:

$$
\begin{aligned}
X_c &= s_a \cdot \cos(w_a) \\
Y_c(d) &= s_b \cdot \sin(w_b) \cdot \cos(d) \cdot \cos(c) + s_a \cdot \sin(w_a) \cdot \sin(d) \cdot \sin(c) \\
Z_c(d) &= s_a \cdot \sin(w_a) \cdot \sin(d) \cdot \cos(c) - s_b \cdot \sin(w_b) \cdot \cos(d) \cdot \sin(c)
\end{aligned}
\qquad (4.3)
$$

Where, using the same nomenclature of the circular cone model when applicable, X_c is directed along the central axis of the cone, Y_c and Z_c are oriented in the directions of the semi major and semi minor axis respectively (for tilt c = 0), and d is the parameter that varies between 0° and 360°. The three different views of the cone can be seen in Figure 4.3.

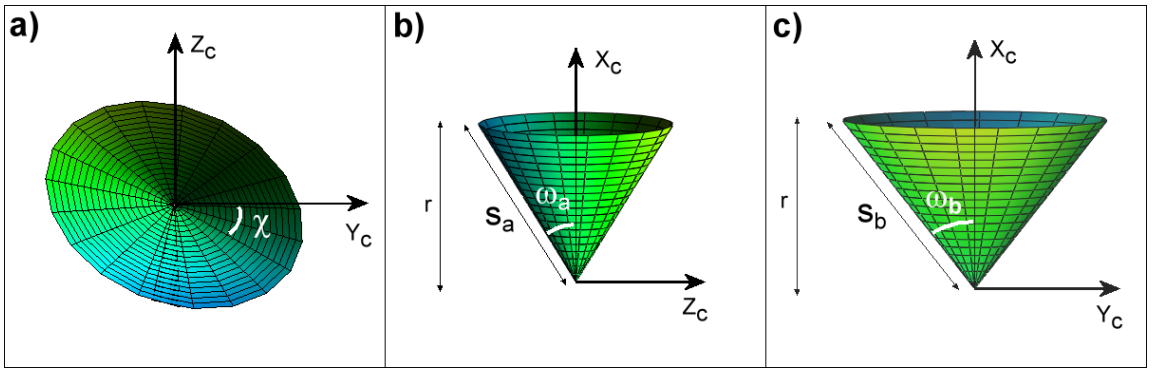

Figure 4.3. Three views of an elliptical cone generated by the elliptical cone model with width ω_a=30° and ω_b=40°. a) Plane Z_cY_c: the base of the cone, with χ=20°. b) Plane X_cZ_c: minor width ω_a of the cone. c) Plane X_cY_c: major width ω_b of the cone.

To project the base's rim of the elliptical cone into the plane of the sky, the same transformation as applied in Zhao's model was employed (Equations 4.2) by introducing the heliographic

latitude l and longitude f in which the central axis of the cone is oriented. The projections of elliptical cones, oriented similarly to the examples shown in Figure 4.2, are displayed in Figure 4.4.

The combination of equations 4.2 and 4.3 allows the projection of an elliptical cone's base on the plane Y_hZ_h, which represents the plane of the sky. Moreover, the projected cone's base characterizes the bright outer edge distinctive for a halo CME event. The elliptical cone model is able to artificially generate a projected halo CME given its characteristic parameters (c, l, f, w_a, w_b, and r), as already exemplified in Figure 4.4. Likewise, a real halo CME observed in LASCO C2/C3 may be approximated by an ellipse. The equation of the ellipse fitted to the measurements may be matched with the model's equations, which will yield in turn the characteristic parameters of the measured halo CME.

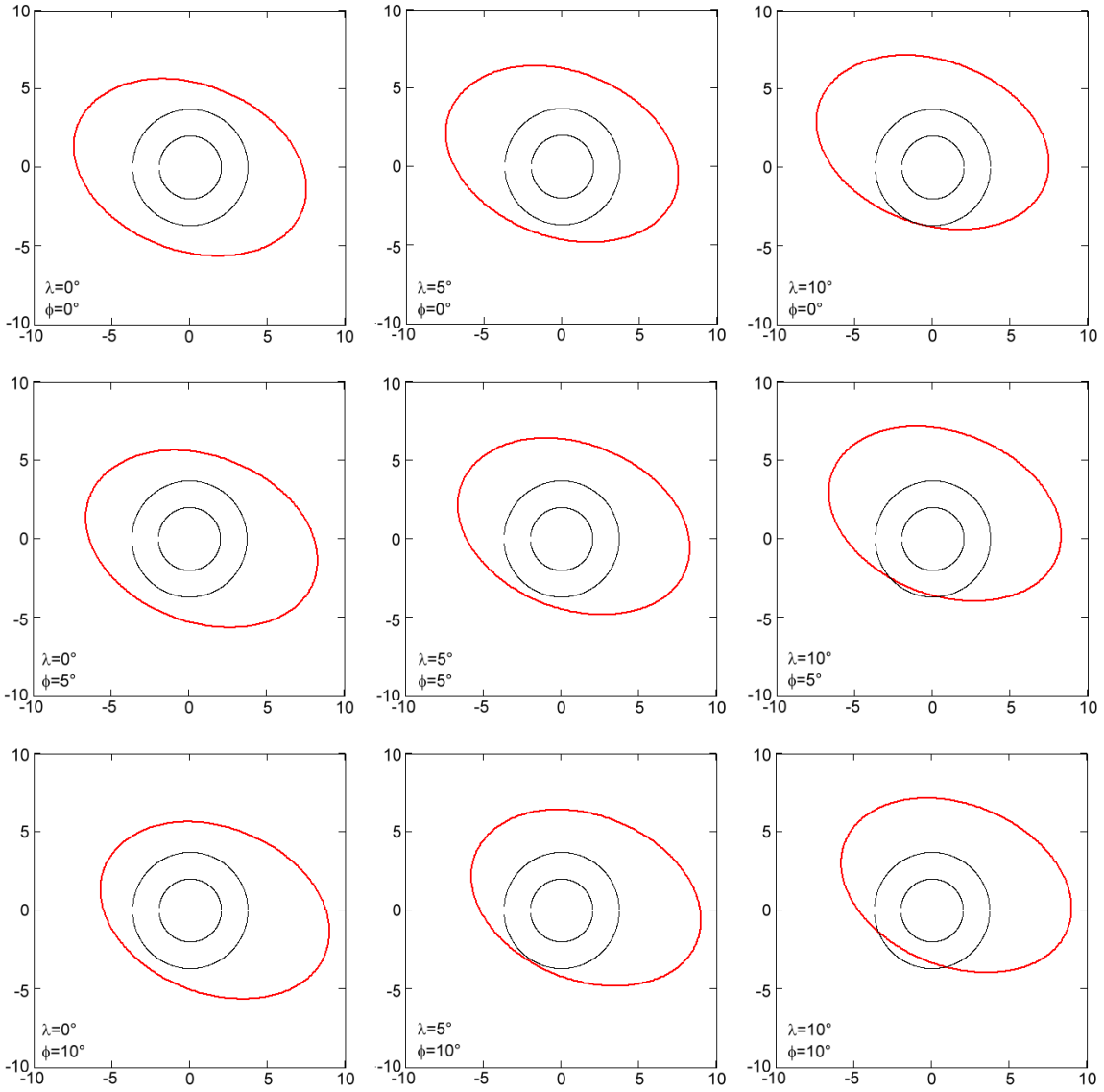

Figure 4.4. Halo CMEs reproduced with the elliptical cone model (red line). The black circles indicate the boundaries of the occulters of LASCO C2 and C3. The scales are given in solar radii. The elliptical cone's inclination is determined according to the values of λ and ϕ, which increase in steps of 5° from left to right and top to bottom, respectively. The half-AW values are ω_a = 30° and ω_b = 40°, while the tilt χ = 20°. The cuts to the cones correspond to a radial distance of 9 solar radii.

The fitting procedure starts with the determination of the coordinates (measured in terms of solar radii) of 5 points that lie in the outer edge of the halo CME, as displayed in the example of Figure 4.5. The points were selected from the frame of the image sequence that showed best the white-light structure of the halo CME (the entire set of analyzed halo CMEs is presented in the next Section). From the five points, it is possible to obtain the coefficients *A*, *B*, *C*, *D*, *E* and *F* of the general second-degree equation:

$$A \cdot x^2 + B \cdot x \cdot y + C \cdot y^2 + D \cdot x + E \cdot y + F = 0 \tag{4.4}$$

Equation 4.4 represents an ellipse if *A* and *C* are of the same sign and different from zero. After mathematical simplifications of the general equation's coefficients, the equation of the measured ellipse can be rewritten as a parametric equation:

$$\begin{aligned} y_p(d) &= h - a \cdot \cos(y) \cdot \cos(d) + b \cdot \sin(y) \cdot \sin(d) \\ z_p(d) &= k - a \cdot \sin(y) \cdot \cos(d) - b \cdot \cos(y) \cdot \sin(d) \end{aligned} \tag{4.5}$$

Where *h* and *k* are the coordinates of the ellipse's centre, *a* and *b* are the semi minor and semi major diameters, y is the tilt of the semi major axis and *d* is the parameter that ranges from 0° to 360°.

Once y, *a*, *b*, *h* and *k* are determined from the ellipse measured in the LASCO C2/C3 images, equations 4.5 may be matched with equations 4.2 (where equations 4.3 have been introduced). In other words, the parametric equations of the ellipse measured in LASCO C2/C3 images are matched with those of the ellipse synthetically generated by the model. The terms of equations 4.2 that involve *cos(d)* and *sin(d)* are respectively matched with those of equations 4.5, as well as the independent terms. The matching yields a system of six equations with six unknowns:

$$\begin{aligned} h &= s_a \cdot \cos(w_a) \cdot \cos(l) \cdot \sin(f) \\ -a \cdot \cos(y) &= s_b \cdot \sin(w_b) \cdot [\cos(f) \cdot \cos(c) + \sin(l) \cdot \sin(f) \cdot \sin(c)] \\ b \cdot \sin(y) &= s_a \cdot \sin(w_a) \cdot [\cos(f) \cdot \sin(c) - \sin(l) \cdot \sin(f) \cdot \cos(c)] \\ k &= s_b \cdot \cos(w_b) \cdot \sin(l) \\ a \cdot \sin(y) &= s_b \cdot \sin(w_b) \cdot \cos(l) \cdot \sin(c) \\ -b \cdot \cos(y) &= s_a \cdot \sin(w_a) \cdot \cos(l) \cdot \cos(c) \end{aligned} \tag{4.6}$$

The terms on the left of the equal sign are known from the ellipse fitted to the five points measured in the LASCO images. Analytical solutions can be determined for all of the unknowns: c, l, f, w_a, w_b, and r. The slant heights s_a and s_b are obtained from $s_a \cdot \cos(w_a) = s_b \cdot \cos(w_b) = r$.

The start point of the ellipse ($d = 0$) can be modified by introducing the phase angle *d2*, which is added to the parameter *d*. After the insertion of *d2*, the left terms of equations 4.6 turn into more complicate expressions, which are renamed as x_i to simplify the mathematical deductions of the unknowns:

$$
\begin{aligned}
x_0 &= h \\
x_1 &= -a \cdot \cos(y) \cdot \cos(d2) + b \cdot \sin(y) \cdot \sin(d2) \\
x_2 &= a \cdot \cos(y) \cdot \sin(d2) + b \cdot \sin(y) \cdot \cos(d2) \\
x_3 &= k \\
x_4 &= -a \cdot \sin(y) \cdot \cos(d2) - b \cdot \cos(y) \cdot \sin(d2) \\
x_5 &= a \cdot \sin(y) \cdot \sin(d2) - b \cdot \cos(y) \cdot \cos(d2)
\end{aligned}
\tag{4.7}
$$

Finally, the analytical solutions for all the unknowns are:

$$
\begin{aligned}
f &= \arcsin \sqrt{\frac{1 + \frac{x_1}{x_4} \cdot \frac{x_2}{x_5}}{1 - \frac{k^2}{h^2} - \frac{x_1}{x_4} \cdot \frac{k}{h} - \frac{x_2}{x_5} \cdot \frac{k}{h}}} \\
l &= \arctan\left(\frac{\sin(f)}{h} \cdot k \right) \\
c &= \arctan\left[\frac{\cos(l)}{\cos(f)} \cdot \left(\frac{x_2}{x_5} + \tan(l) \cdot \sin(f) \right) \right] \\
w_a &= \arctan\left(\frac{\tan(l)}{\cos(c)} \cdot \frac{x_5}{k} \right) \\
w_b &= \arctan\left(\frac{-\tan(l)}{\sin(c)} \cdot \frac{x_4}{k} \right) \\
s_a &= \frac{h}{\cos(w_a) \cdot \cos(l) \cdot \sin(f)} \\
s_b &= \frac{s_a \cdot \cos(w_a)}{\cos(w_b)}
\end{aligned}
\tag{4.8}
$$

The value of *d2*, which lies in the interval from 0° to 360°, is crucial. The transcendent equations in 4.6 yield non-unique solutions. Solutions vary according to the phase angle *d2*, added to the parameter *d*. Fortunately, in the considered application the valid solutions are constrained to occur within four equivalent, limited ranges of *d2*'s, with noncomplex values. An example is illustrated in Figure 4.6, which corresponds to the ellipse fitted to the halo CME shown in Figure 4.5. The four ranges of solutions (90° apart) are restricted within the red crosses, while the blue crosses denote the central solution. Outside these ranges the solutions are complex. The solutions close to the extremes of the range (those near the red crosses) can be easily discarded for being highly improbable. For instance, the distance may become infinite and at the same time the AW gets close to zero, or the distance may be only a couple of solar radii while the AW becomes unusually large. The solution for which f coincides with the heliographic longitude of the source region (column 6 of Table 3) has been chosen as the most realistic one. It usually lies close to the centre of the range of valid solutions.

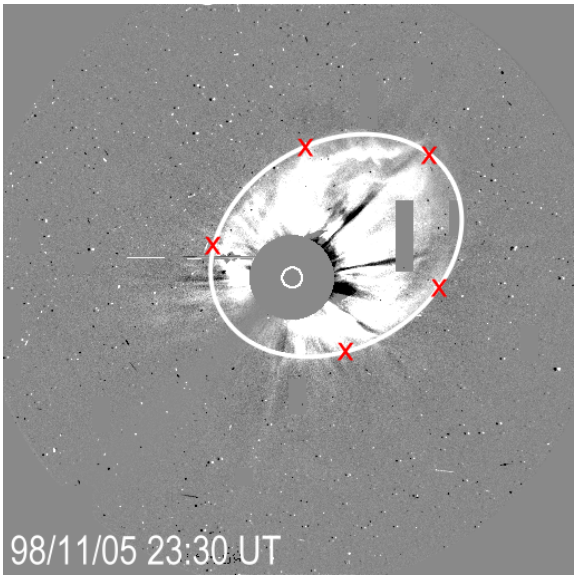

Figure 4.5. The halo CME on November 5, 1998, as captured by the LASCO/C3 coronagraph. A pre-event image has been subtracted to increase the contrast of faint features. The five selected points are indicated by the red crosses, while the thick white line represents the ellipse fitted to those points.

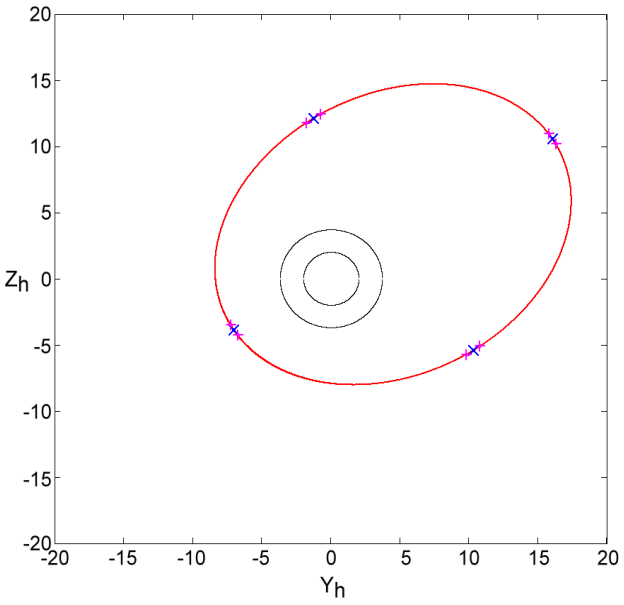

Figure 4.6. The simulated halo CME on November 5, 1998. The crosses and x refer to different start points of the ellipse. The four groups of non-complex solutions are constrained to starting points within the red crosses. The central solutions are marked by the blue crosses.

4.3 The set of analyzed halo CMEs

The set of halo CMEs to be reproduced by the above described elliptical model consists of 30 events, selected from the halo CME database at *ftp://ares.nrl.navy.mil/pub/lasco/halo*. The selected events occurred within the period Jan 1998 – Dec 2002, in which the halo CME database reports ~225 events. Since halo CMEs are normally quite dim, the selection process was carried out on the basis of differential images, in order to improve the visualization of faint features. The selected halo CMEs fulfil the following conditions:

- They are front-sided, so that it is possible to identify their associated source region in the low corona, in order to allow for later comparisons between the tilts of the halo CMEs (χ) and those of their corresponding source regions.
- They are full halo CMEs, i.e. their round outer edge surrounds completely the coronagraph's occulter. This is to avoid uncertainties in the determination of the ellipse to be fitted by the model. Moreover, limb CMEs exhibit a round leading edge (as pointed out

by Schwenn et al. (2005), and not flat as assumed by the flat base of the cone model as discussed here. This effect may be disregarded if the leading edge is observed from above, which is the case of full halo CMEs.

- They are bright events with respect to their surroundings, or they show neat outer edges. This characteristic is pursued in order to make easier and less subjective the task of selecting the five points that define the fitting ellipse.

Examples of the selected halo CMEs are shown in Figure 4.7. Even though the first example is quite faint, its outer edge is well defined. There are only 2 faint events like this one in the set of 30 selected halo CMEs, identified by an asterisk in Table 3.

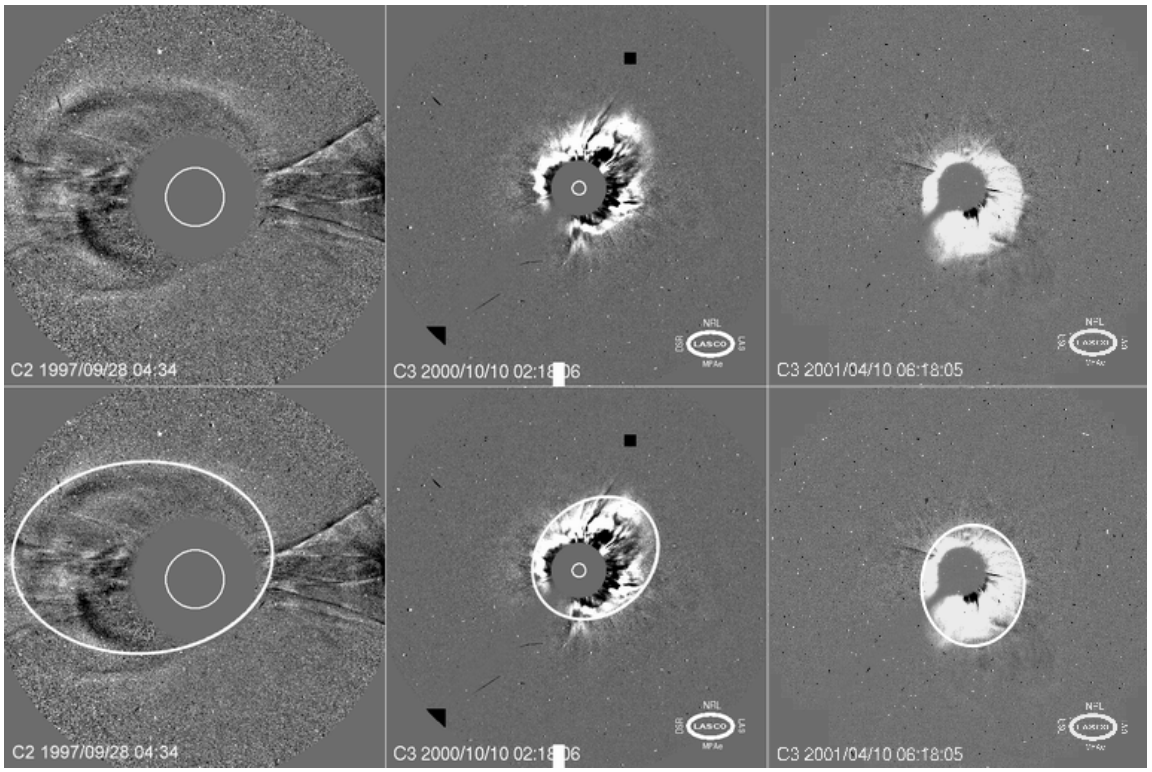

Figure 4.7. Top: three examples from the selected set of halo CMEs, displayed as running difference images. Bottom: the matched ellipses for the corresponding cases. The leftmost example corresponds to a CME in LASCO C2, while the 2 remaining cases show the CME in the FOV of LASCO C3.

Relevant information on the 30 selected halo CMEs is compiled in Table 3. Date and time of observation (columns 2 and 3) correspond to the time of the CME's detection by LASCO. Column 4 contains the CME's plane-of-sky speeds, as given by the SOHO/LASCO CME Catalogue (*http://cdaw.gsfc.nasa.gov/CME_list*). The presented speeds result from a linear fit through the points of the event's height-time diagrams (see Figure 3.7 a). When projected onto the plane of the sky, features within a halo CME travel at a speed that roughly corresponds to the expansion speed of the CME. The CME expansion speed is defined as the growth rate approximately perpendicular to the direction of propagation of the CME (Dal Lago et al. 2003). The frequency distribution of the plane-of-sky speeds of this set of halo CMEs is presented in Figure 4.8. The average speed is located at ~1200 km s^{-1}, a somewhat higher value when compared to the plane-of-sky speeds measured for other CME sets (see Subsection 3.3.3). Dal Lago et al. (2003) found the expansion speed (V_{exp}) to be related to the radial speed of

propagation of the CME (V_{rad}) through the empirical formula: $V_{rad} = 0.88 \cdot V_{\exp}$. It was derived from the comparison of the expansion and propagation speeds of 57 limb CMEs.

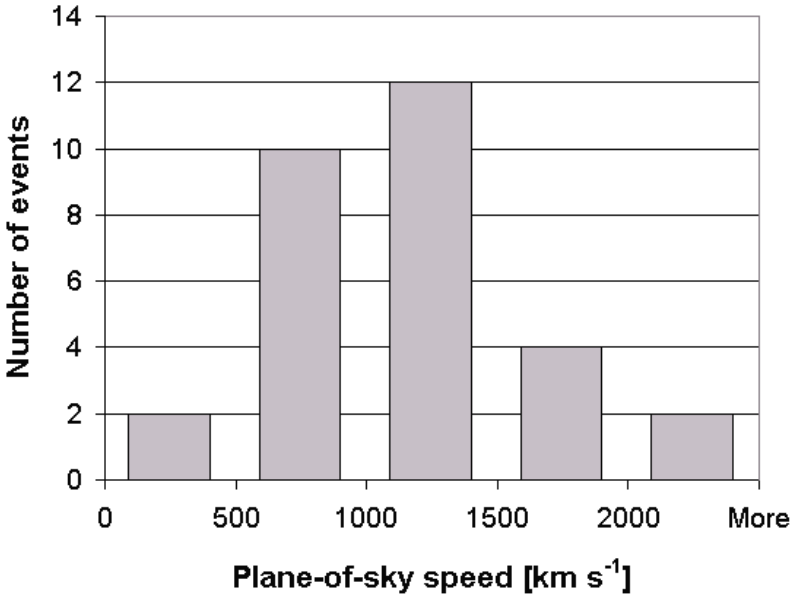

Figure 4.8. Speed distribution of the 30 halo CME events presented in Table 3.

The associated source regions of the selected halo CMEs have been identified by using the same technique described in Subsection 3.4.1. Columns 5 and 6 in Table 3 denote the heliographic coordinates of the source region's central point. The distribution of the absolute latitude values of the source regions are plotted in Figure 4.9a. The average absolute latitude is located at 19°±7°, which coincides with the typical latitudes of ARs found for the set of structured CMEs (see Subsection 3.4.2). Figure 4.9b confirms, as expected, that the source regions are located near the center of the solar disk. The average absolute heliographic longitude was ~20° with respect to central meridian. No source regions of the halo CMEs listed in Table 3 were found to be located further away from central meridian than 45° heliographic longitude.

Column 7 contains information on the length of the associated SRs, and will be analyzed in the next Section.

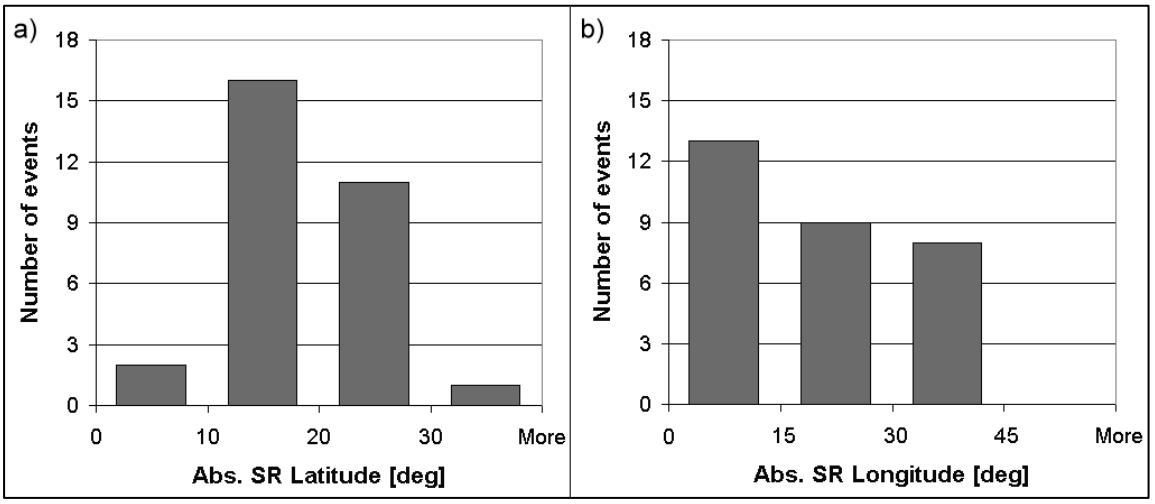

Figure 4.9. a) Latitude and b) Longitude distribution of the SRs associated with the halo CMEs of Table 3.

Table 3. The 30 selected halo CMEs and spatial parameters of their source regions. Events indicated with an asterisk correspond to faint halo CMEs.

Nr.	CME date	CME time (UT)	CME speed linear-fit (km/seg)	SR central latitude (deg)	SR central longitude (deg)	SR length (deg)
(1)	(2)	(3)	(4)	(5)	(6)	(7)
1	1997 Apr 07	14:27	878	-30	-20	10.6
2*	1997 Sep 28	01:08	359	33	-3	13.6
3*	1998 Jan 02	23:28	438	27	40	15.7
4	1998 Apr 29	16:58	1374	-16	-21	8.5
5	1998May 02	14:06	938	-14	17	6.0
6	1998 Nov 05	20:44	1118	23	18	13.7
7	1999 May 03	06:06	1584	19	-43	9.5
8	2000 Feb 09	19:54	910	-14	41	11.8
9	2000 Feb 17	21:30	728	-29	-7	9.3
10	2000 Jun 06	15:54	1119	20	-14	9.3
11	2000 Jun 10	17:08	1108	20	41	9.6
12	2000 Jul 14	10:54	1674	18	0	15.9
13	2000 Sep 12	11:54	1550	-21	5	18.2
14	2000 Sep 16	05:18	1215	13	6	9.3
15	2000 Oct 09	23:50	798	0	14	10.2
16	2000 Nov 24	05:30	994	21	6	5.9
17	2000 Nov 24	15:30	1245	19	11	6.9
18	2001 Jan 20	19:31	839	-7	-39	9.7
19	2001 Feb 15	13:54	625	13	-6	10.5
20	2001 Apr 09	15:54	1192	-21	6	6.7
21	2001 Apr 10	05:30	2411	-24	9	10.1
22	2001 Aug 25	16:50	1433	-19	-38	9.3
23	2001 Sep 24	10:30	2402	-20	-29	11.0
24	2001 Oct 09	11:30	973	-29	-9	10.8
25	2001 Oct 19	16:50	901	15	30	10.1
26	2001 Oct 22	15:06	1336	-19	-21	9.8
27	2001 Oct 25	15:26	1092	-18	23	6.3
28	2001 Nov 22	23:30	1437	-13	26	12.1
29	2002 Apr 17	08:26	1240	-13	33	11.6
30	2002 Aug 16	12:30	1585	-12	-21	7.1

4.4 Application of the model to halo CMEs

The final goal of the model developed in Section 4.2 was to test how the ratio L/D (i.e. the ratio between the average width of structured CMEs viewed perpendicular to the line of sight and parallel to it; obtained in Subsection 3.6.3) compares with the ratio of the fitted major and minor widths w_b and w_a of the selected set of halo CMEs. The 30 full halo CME events listed in Table 3 were approximated by ellipses, selecting 5 points that lay on the outer edge of the halo CME. The parametric equations of the so-obtained ellipses were then matched with those of the projected cross section of an elliptical cone, to obtain its characteristic geometric parameters. Although these geometric parameters are not unique, they have been calculated for all cases under the same conditions, which allow inter-comparisons. The characteristics of the solutions

have been indicated in Subsection 4.2.2. The solution for which f coincides with the heliographic longitude of the source region (column 6 of Table 3) has been chosen as the most realistic one. It usually lies close to the centre of the range of valid solutions. For each of the 30 studied events, the overall behaviour of the solutions has been carefully taken into account. In some few exceptional cases that evidently had suffered from deflections in the longitudinal direction (because the solutions based on the value of the source region longitude were irrelevant), the central solution of the value range was taken as a trade-off solution. These exceptional cases have been indicated by a double asterisk in Table 4. It is worth to mention that the ratio w_b/w_a is nearly stable within the range of real solutions, except near the extremes.

Table 4 presents the values derived for the analyzed set of halo CMEs, by means of the elliptical cone model. The first two columns refer to CME index number and date. Columns 3 to 9 refer to the seven geometrical properties that define the elliptical cone fitted to the measured halo CME. The quantities in columns 10 and 11 arise from combinations of them.

Table 4. The geometrical characteristics derived with the elliptical cone model for the 30 halos listed in Table 3. Events indicated with a double asterisk refer to those for which the central solution was taken.

CME index (1)	CME date (2)	χ (deg) (3)	λ (deg) (4)	ϕ (deg) (5)	ω_a (deg) (6)	ω_b (deg) (7)	s_a ($R_\odot$) (8)	s_b ($R_\odot$) (9)	ω_b/ω_a (10)	$2\omega_b$-$2\omega_a$ (deg) (11)
1	1997 Apr 07	-33	-15	-20	62	69	8	10	1.12	15
2**	1997 Sep 28	2	13	-34	45	58	5	6	1.28	26
3	1998 Jan 02	-14	10	40	47	60	19	26	1.29	27
4	1998 Apr 29	19	18	-21	59	69	5	7	1.17	20
5	1998May 02	88	9	17	48	53	7	8	1.11	11
6	1998 Nov 05	-30	13	18	36	45	18	21	1.27	19
7	1999 May 03	6	27	-43	57	67	16	22	1.17	19
8	2000 Feb 09	36	-14	41	62	70	5	7	1.13	16
9	2000 Feb 17	65	11	-7	47	56	11	14	1.19	18
10**	2000 Jun 06	79	29	-3	84	85	9	12	1.02	3
11	2000 Jun 10	-29	24	41	67	76	11	18	1.14	18
12**	2000 Jul 14	-14	20	16	72	73	5	5	1.02	2
13	2000 Sep 12	56	-18	5	54	58	15	16	1.08	9
14	2000 Sep 16	37	13	6	55	56	11	12	1.03	3
15	2000 Oct 09	-39	11	14	40	48	13	15	1.19	15
16	2000 Nov 24	-80	7	6	24	31	9	10	1.31	15
17	2000 Nov 24	-75	12	11	37	46	6	7	1.23	17
18	2001 Jan 20	-60	5	-39	62	65	6	7	1.06	7
19	2001 Feb 15	74	6	-6	35	42	16	17	1.21	15
20**	2001 Apr 09	-44	-29	-8	67	70	9	11	1.05	6
21	2001 Apr 10	87	-12	9	36	41	14	14	1.11	8
22	2001 Aug 25	-30	-29	-38	62	69	15	20	1.12	15
23	2001 Sep 24	2	-13	-29	54	57	16	17	1.07	7
24**	2001 Oct 09	61	-10	0	29	29	25	25	1.01	1
25	2001 Oct 19	-27	23	30	75	77	13	15	1.02	3
26	2001 Oct 22	-65	-12	-21	56	59	11	12	1.04	4
27**	2001 Oct 25	73	-19	9	58	61	11	12	1.06	7
28	2001 Nov 22	-27	12	26	62	67	13	15	1.07	9

CME index (1)	CME date (2)	χ (deg) (3)	λ (deg) (4)	ϕ (deg) (5)	ω_a (deg) (6)	ω_b (deg) (7)	s_a ($R_\odot$) (8)	s_b ($R_\odot$) (9)	ω_b/ω_a (10)	$2\omega_b-2\omega_a$ (deg) (11)
29	2002 Apr 17	-25	20	33	59	65	13	16	1.11	13
30	2002 Aug 16	-47	-30	-21	62	64	12	12	1.04	4

It is interesting to analyse c, l and f (columns 3 to 5 of Table 4) derived for the set of halo CMEs. The comparison of c with the associated source region tilt provides clues on how the CME's main axis relates to the tilt of the SR neutral line, and eventually whether it may have suffered rotation during its outward expansion. However, this is beyond the scope of the present analysis. The prime goal of this study is directed towards the quantization of the ratio between the perpendicularly-directed widths w_a and w_b (columns 6 and 7). The histogram for the values w_a and w_b indicates that the asymmetry does also exist in halo CMEs, as evident from the shift of the distributions (see Figure 4.10). Their averages are located at 54°±14° and 60°±13° respectively, while the average difference between them $<2w_b - 2w_a>$ is ~12°. The difference between both widths is however not astonishing, and the calculated ratios w_a/w_b (column 10) differ from those previously obtained for the structured CMEs with extreme projections. The histogram of w_a/w_b presented in Figure 4.11 shows that ratios larger than 1.2 are not so common, while the average ratio is 1.12. This value is not so remarkable when compared to the $L/D = 1.6$ calculated in Section 3.6.3.

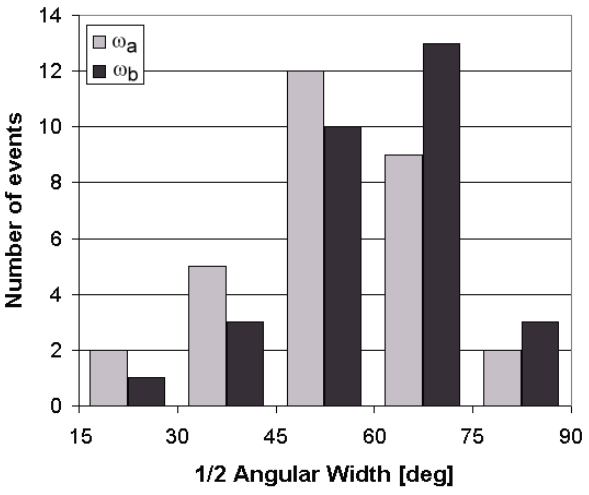

Figure 4.10. Histogram of the values ω_a and ω_b calculated for the set of halo CMEs, in bins of 15°. Light grey bars correspond to half-AWs in the direction of the ellipse's minor width (ω_a), while dark grey columns refer to half-AWs in the direction of the ellipse's major width (ω_b).

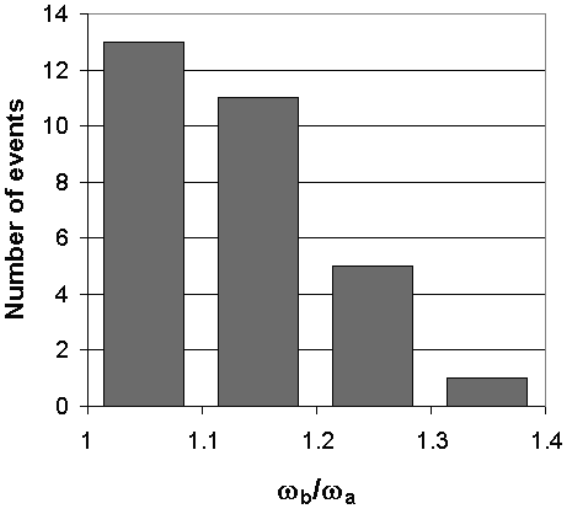

Figure 4.11. Histogram of the ratio ω_a/ω_b, in bins of 0.1.

The reason for the discrepancy in the symmetry ratio for the compared groups of CMEs (structured and halo) may lie in the different attributes of the source regions that characterize both groups of events. After the examination of individual events, it was noticed that the two faint events of the set of halo CMEs had large ratios w_a/w_b with respect to the rest of the fitted events. These originated in source regions whose neutral line length was above the average of the

group (~10°). The findings presented in Section 3.6.2 suggest that the degree of cylindrical symmetry depends on the length of the neutral line that is associated with the CME origins. Specifically, structured CME events associated with short SRs showed a lower degree of correspondence with the scheme, resembling more a bubble with rotational symmetry rather than a cylinder. If so, it is possible that the set of studied halo CMEs belongs to this kind of events. In order to test this hypothesis, it is necessary to compare the distributions of the source region lengths for both CME groups: the 30 full halo CMEs and the 33 structured CMEs exhibiting extreme projections. Figure 4.12 displays the frequency distribution for the lengths of the source regions for both sets of CMEs. The distribution for the halo CMEs is narrower, with its average located at ~10°±3°; while that of the structured CMEs is broader, reaching ~40° and with a larger average located at 16°±10°.

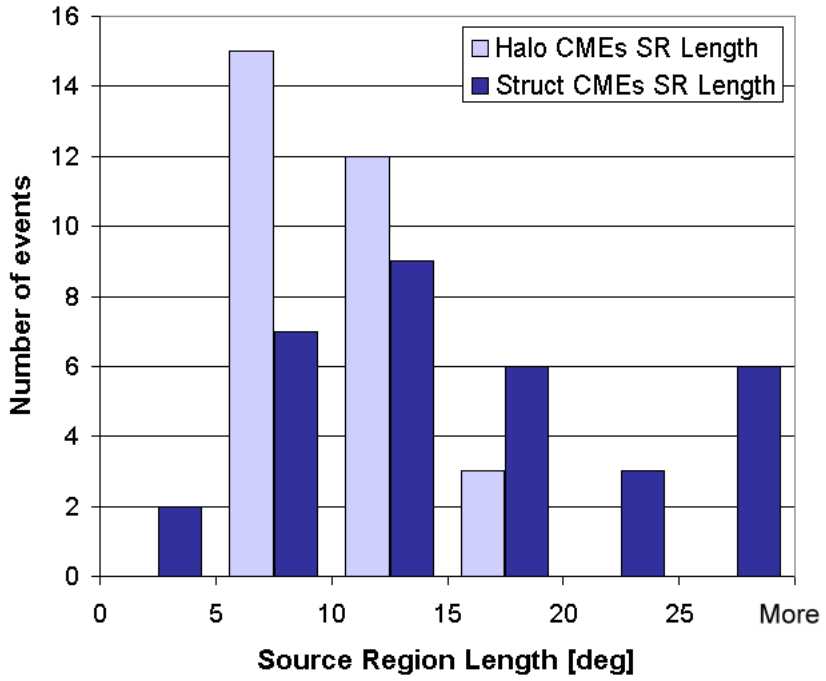

Figure 4.12. Histogram of the source region lengths for both sets of analyzed CMEs: halo and structured ones with extreme projections (see Section 3.6.3).

We believe that the dissimilitude in the SR length distributions might help to explain the discrepancies found in the two sets of CMEs. With the intention of finding further evidence of this phenomenon, a search of halo CMEs originating in very large source regions was carried out. Basically, the investigation was opposite to that of the set of 30 bright halo CMEs, for which the source region was analyzed after the selection process. In this case, the starting point of the search was the list of post-eruptive arcades (PEAs), published by Tripathi, Bothmer & Cremades (2004). PEAs can be considered as unique proxies for CME eruptions. In order to find CMEs associated with extended source regions, the longest PEAs of the list were inspected for counterparts in LASCO/C2 and C3. Additionally, the source region had to be located near the centre of the solar disk, so as to yield a full halo CME. A significant halo CME was identified, related to the PEA on January 28, 2002. The PEA was approximately centred at S30 E20, and subtended a length of ~32°. The observed halo CME (see Figure 4.13a) was not listed in the halo CME database at *ftp://ares.nrl.navy.mil/pub/lasco/halo*, possibly due to its faintness. The halo CME is substantially stretched out, and its fitted ellipse shows high eccentricity (see Figure 4.13b). The geometrical parameters of the CME, as derived from the elliptical cone model are presented in Table 5. A remarkably large ratio w_a/w_b=1.64 is found in this event, which was

associated with an extended source region. The result supports the idea that long source regions lead to a pronounced cylindrical symmetry of CMEs.

The study of the source regions for the set of structured CMEs, indicated that the largest source region lengths of CMEs are typically found at latitudes above 20°, in connection with decaying bipolar regions. The latter event, presented in Table 5, substantiates the idea that highly asymmetric halos with large w_a/w_b are expected to originate from large, extended source regions. Unfortunately, it will be difficult to observe a CME as a halo if it originated from these extended source regions, since they appear preferentially at high latitudes. Even though a halo CME were observed under these circumstances, it will not appear as the classic bright halo, being its detection and analysis more complicated.

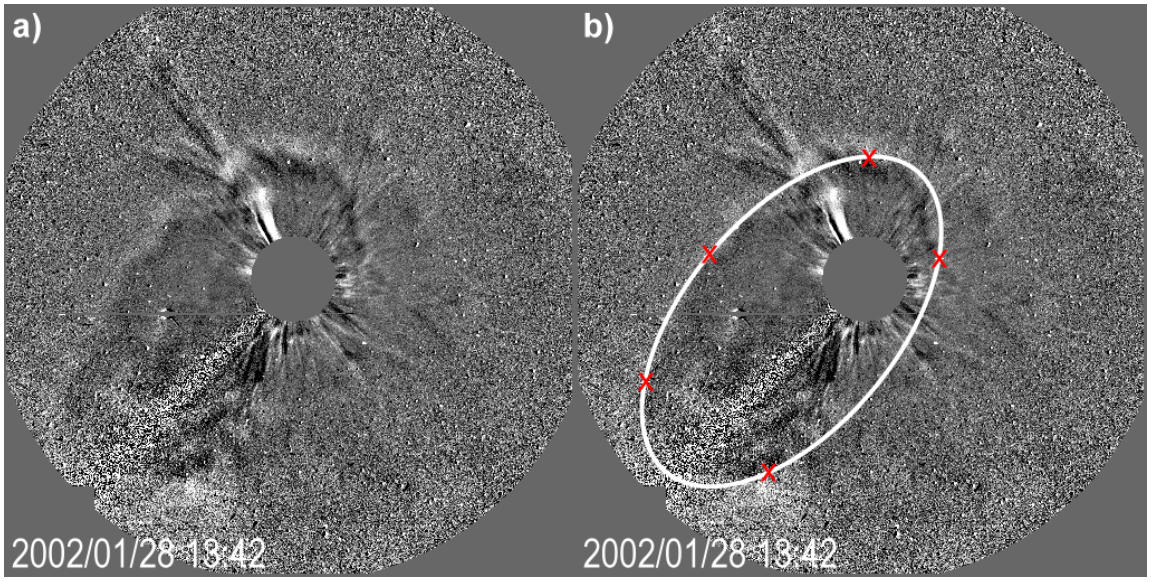

Figure 4.13. a) Differential image of the halo CME on January 28, 2002, as detected by the LASCO/C3 coronagraph. b) The ellipse fitted to the event displayed in a).

CME index (1)	CME date (2)	χ (deg) (3)	λ (deg) (4)	ϕ (deg) (5)	ω_a (deg) (6)	ω_b (deg) (7)	s_a ($R_\odot$) (8)	s_b ($R_\odot$) (9)	ω_b/ω_a (10)	$2\omega_b-2\omega_a$ (deg) (11)
31	2002 Jan 28	-44	-13	-23	30	49	22.3	29.4	1.64	38

Table 5. The geometrical characteristics derived from the application of the elliptical cone model to the halo CME on January 28, 2002.

Summary and conclusions

The instruments onboard the SOHO Mission, launched in December 1995, have provided to date unprecedented multi-wavelength data on the solar corona. The exceptional cadence and spatial resolution of the provided images reveal for the first time a wealth of dynamics and small-scale features, which allow detailed investigations of the involved physical processes. Fine structures perceived within CMEs for the first time are expected to promote better understanding of their three-dimensional configuration and the magnetic fields that organize them. In order to infer observational properties that facilitate this task, a set of 276 structured CMEs has been identified in the SOHO/LASCO data. The survey, which comprised observations from 1996 until the end of 2002, was based on the selection criterion by which: *a "structured" CME is an outward moving white-light feature in the field of view of LASCO/C2, that reveals inherent fine structure discernable from the ambient corona, and which develops in the field of view of C2 as part of the entire white-light feature during its outward motion.* Compared to the total number of CMEs detected during that period (~7000), the number of identified structured CMEs might seem small. However, it must be taken into account that events which showed less fine structure such as very narrow (jet-like) and halo CMEs were discarded in the selection process. The definition of structured CME implied that the majority of them originated from limb and near-limb regions, so that most of the disk- and backside events were also left out after the selection.
For 124 out of the 276 identified structured events, it was possible to detect their low coronal and underlying photospheric source regions uniquely. The study required the analyses of SOHO/LASCO/EIT/MDI and ground-based Hα data. In the next step, basic properties of these CMEs, such as angular widths and position angles were calculated, in order to properly compare them with the characteristic parameters of their source regions. From the backtracking of these regions to the photospheric magnetic field, it was found that they were associated with areas of opposite magnetic polarities. They were primarily located in the activity belts in both hemispheres, with typical lengths of 5°-20°, while the longer ones were found at higher latitudes in decaying regions. Active regions as sources of the structured CMEs showed agreement with the butterfly diagram. Conversely, source regions characterized by disappearing filaments outside active regions were related to the migration of magnetic flux towards polar latitudes.

The major results provided by the inter-analysis of the 124 structured CMEs and their associated source regions can be summarized as follows:

- *Deflection*: The central PA of the structured CMEs was systematically deflected with respect to that of the respective SRs by ~20° to lower latitudes during the period 1996-1998. At times of higher solar activity the deflections varied in correspondence with the complexity of the corona. A further analysis of the deflection yielded a significant correlation with the number of CHs present at a specific time, their area and their distance to the CMEs' source regions.

- *3D scheme*: The 3D topology of structured CMEs observed in the field of view of LASCO C2 (frequently matching the typical three-part CME structure) can be classified according to a basic scheme in which the fundamental parameters are the heliographic position and orientation of the source region's neutral line, separating opposite magnetic polarities. Imprints of the photospheric magnetic field configuration are evident in the white-light CMEs. The source regions exhibited considerably smaller spatial scales than the corresponding CMEs, indicating the expansion of low coronal magnetic structures into the FOV of C2, directly evident in some cases. The apparent profile of an individual CME, however, may differ more or less from the basic scheme because of the solar variability of the fundamental parameters, e.g. many neutral lines are not straight lines, but have rather complicated topologies, especially in active regions. The degree of correspondence with the scheme also depends on the absolute values of the SR lengths, which will impose difficulties for small values typically found in compact active regions.
- *Aspect ratio and self-similarity*: The average width of structured CMEs with axis oriented along the line of sight (D) was found to amount to 14° in EIT and 37° in LASCO/C2 images. Likewise, average widths of structured CMEs with axes perpendicular to the line of sight (L) were larger: 22° in EIT and 58° in LASCO/C2. Remarkably, the ratio L/D was identical as measured in both instruments, with a value of 1.6. In a subsequent step, an elliptical cone model was developed, on the basis of the circular cone model by Zhao et al. (2002). It was applied to a set of full, bright, and front-sided halos, looking forward to find whether the halo events showed a relationship similar to L/D=1.6. However, the average ratio ω_a/ω_b related to the halo CMEs yielded 1.12. The discrepancy is interpreted to be related with the considerably shorter source region lengths of the selected set of halo CMEs, in comparison to the larger ones found for the set of structured CMEs. Hence, highly asymmetric halos are expected to originate preferentially from extended regions of opposite polarity, typically found at higher latitudes than average.

The results of the detailed study of structured CMEs imply that their 3D configuration is organized along an axial direction, which is often directly visible in the case of extended prominences, shaped by the neutral line separating regions of opposite magnetic polarity. The real axis of the CME seems to correspond with the long axis of a large-scale helical magnetic flux rope that was formed in the SR, with the prominence being the bottom part of this magnetic system. The CME as represented by a magnetic flux rope formed in the low corona before its eruption will suffer an enormous expansion once it is triggered to lift off, as supported by the often directly visible self-similarity of the magnetic features in the studied events, in the low corona and further out. The study of CME events lacking self-similar expansion would be additionally interesting. The expansion of CMEs is most dramatic within the first two solar radii. Ultimately, the expanding flux rope CME may be identified as a magnetic cloud in the solar wind (see, e.g., Bothmer & Schwenn 1998).

The findings related to CME deflection explain the detection in the ecliptic of interplanetary CMEs that originated at high latitudes. Results related to the three-dimensional configuration and dimensions of CMEs can be directly employed as inputs for models, not only of CME evolution, but also of initiation. Concerning the structured CMEs' dimensions, the width D (likely associated with the diameter of a magnetic flux rope), of ~2.7 $R_\odot$ at 4 $R_\odot$, agrees with the value of radial diameter extrapolated for magnetic clouds, of ~2.4 $R_\odot$ at 4 $R_\odot$.(see Bothmer & Schwenn 1998). Likewise, the azimuthal broadness of a magnetic cloud (~60°) agrees with the

average value found for L of the structured CMEs (58°). It is very important to deduce expansion factors of CMEs, since they are decisive parameters in the determination of their early evolution in the heliosphere.

A primary representation of CMEs in three dimensions has been deduced, yet it does not explain the difficulties and complexity that arise from the initial configuration of the source region and the surrounding corona. The shape of the neutral line is often, but not always fully aligned with the prominence axis. During the eruption of the flux rope it may or may not undergo considerable distortion depending on the level of complexity of its evolution. High cadence and spatial resolution data are required to track the expansion and evolution of small features within infant CMEs, especially in the first couple of solar radii.

The overall cylindrical symmetry suggested by the structured CMEs is a big step towards the characterization of their 3D structure. The 3D configuration of other types of CMEs (e.g., jet-like CMEs) remains uncertain.

A recent study based on polarization measurements (Moran & Davila 2004), supports the findings on the cylindrical geometry found within structured CMEs. The 3D topology derived from this study and the validity of the presented general scheme can be directly proven by means of multipoint observations. The NASA STEREO mission, to be launched in early 2006, will provide for the first time observations of the same CME from two different vantage points, enabling the direct proof of these results. Magnetograph data from the upcoming Solar-B mission will be essential to characterize the magnetic field sources of CMEs.

Out of the ecliptic missions like the planned ESA Solar Orbiter or the NASA Solar Probe would allow further studies to prove deflections of CMEs in longitudinal directions.

Appendix

A The STEREO Mission

The Solar TErrestrial RElations Observatory (STEREO) consists of two almost identical spacecraft, which will observe the Sun simultaneously from two different vantage points in interplanetary space. In such a configuration, displayed in Figure A.1, it will be possible for the first time to observe the Sun, its corona, and interplanetary space in 3D. The two observatories are termed STEREO A and STEREO B, as acronyms for "ahead" and "behind". Scheduled to be launched in February 2006, the two spacecraft will initially approach the Moon. The lunar swingbys will ensure first the positioning of STEREO B in its orbit lagging Earth, and about a month later of STEREO A leading it. Each spacecraft will separate from Earth at the rate of 22° per year, within the ecliptic plane. The mission, part of the NASA Solar Terrestrial Probes program, is initially planned for two years. Instructions from the principal investigators (PIs) for commanding the instruments and experiments will be given at the Payload Operations Centers, situated at four different places in the world. These commands will be gathered by The Mission Operations Center at the Johns Hopkings University Applied Physics Laboratory and sent to the spacecraft via NASA's Deep Space Network.

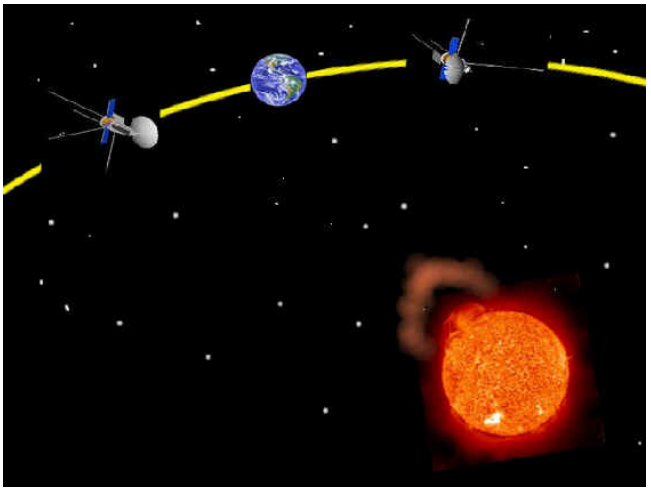

Figure A.1. Artist's conception of the two STEREO spacecraft location with respect to Sun and Earth. Credit: STEREO consortium (*http://stereo.jhuapl.edu/*).

The simultaneous views from the two spaced out spacecraft, in conjunction with a redundant view from ground-based observatories on Earth, will provide for the first time 3D stereoscopic images of the Sun. Main science objectives of the mission are to understand the causes and mechanisms that give rise to CMEs, reveal their 3D structure, trace their propagation through the heliosphere, investigate the processes and locations of energetic particle acceleration, and develop a 3D time-dependent model of the ambient solar wind (Rust 1998). In order to achieve its goals, the STEREO Mission comprises two instruments and two instrument suites, which make up 16 instruments in total. One of the spacecraft is sketched in Figure A.2 with its visible instruments. Among the instruments is the PLAsma and Supra Thermal Ion Composition (PLASTIC), which will study coronal-solar wind and solar wind-heliospheric processes. The STEREO/WAVES instrument will track the origins and evolution of radio disturbances from Sun to Earth. The instrument suites are the In situ Measurements of PArticles and CME

Transients (IMPACT), comprised of 7 instruments devoted to measure the solar wind electrons, interplanetary magnetic fields and solar energetic particles, and the Sun-Earth Connection Coronal and Heliospheric Investigation (SECCHI), described in the next subsection. Further information on the STEREO Mission may be found at *http://stereo.jhuapl.edu/* and at *http://stp.gsfc.nasa.gov/missions/stereo/stereo.htm.*

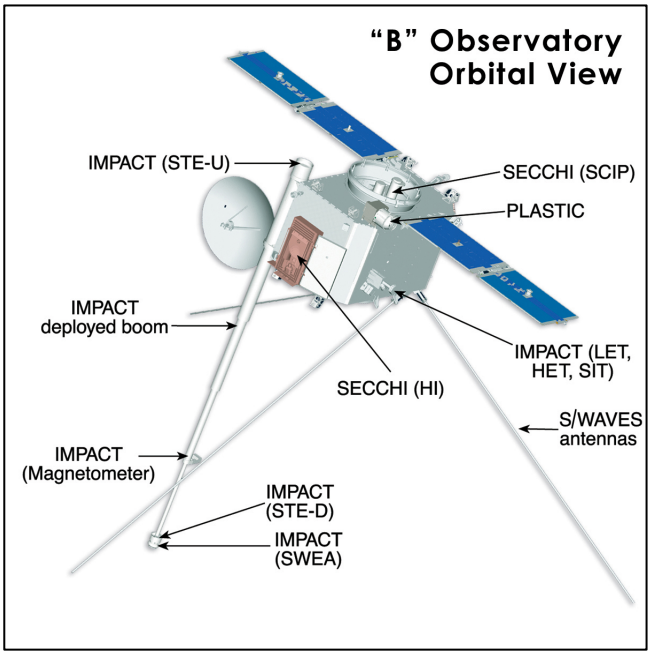

Figure A.2. View of the STEREO B spacecraft and some of its components. Credit: STEREO consortium.

A.1 The STEREO/SECCHI instruments suite

The Sun Earth Connection Coronal and Heliospheric Investigation (SECCHI) consists of an extreme ultraviolet imager (EUVI), two white light coronagraphs (COR1 and COR2), and a wide field heliospheric imager (comprised of HI-1 and HI-2). The EUVI and the CORs share mount in an assembly termed SCIP (for Sun Centered Instrument Package), illustrated in Figure A.3. The fundamental science objective of this suite of remote sensing instruments is to improve the present knowledge of the 3D structure of the Sun's corona, and in particular of CMEs. EUVI will allow observations at low coronal heights up to 1.7 $R_{\odot}$, while the coronagraphs will cover heights ranging from 1.25 up to 15 $R_{\odot}$ and the heliospheric imagers from 12 up to 318 $R_{\odot}$. In the case of CMEs directed towards Earth, it will be possible to track them since their birth, following their journey across the coronagraphs and through interplanetary space until their arrival at Earth, by means of the heliospheric imagers.

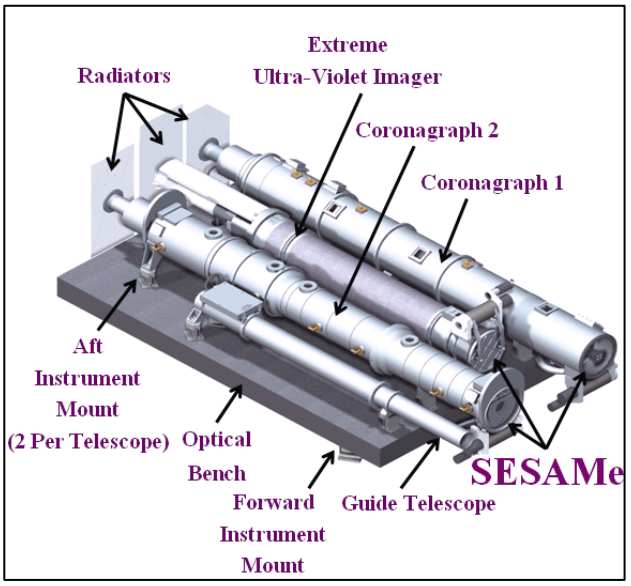

Figure A.3. The SECCHI package and its main components. Courtesy V. Bothmer.

While COR1, COR2, HI-1 and HI-2 will observe in the visible wavelength ranges, the EUVI bandpasses are similar to those of EIT: He II (**304** Å), Fe IX (**171** Å), Fe XII (**195 Å**), and Fe XIV (**211** Å). All the instruments will capture the images with CCDs of 2048×2048 pixels, which correspond to various resolutions depending on the field of view. For instance, EUVI's pixel to pixel resolution corresponds to 1.6 arc sec. In COR1 images, the pixel to pixel resolution will be of 7.5 arc sec, whereas in COR2 images it will be of 14 arc sec. Lastly, HI-1 and HI-2 will capture interplanetary features with a pixel to pixel resolution of 35.2 and 120 arc sec respectively. With respect to SOHO's EIT and LASCO instruments, not only the resolution has increased, but the cadence has improved as well. In the maximum cadence mode, EUVI may capture consecutive images every 11 sec at full resolution, while COR1 and COR2 may do it every 15 and 22 sec respectively. In the case of HI-1 and HI-2, the maximum cadence may reach correspondingly 1 and 8 min. However, the synoptic cadences amount 20 min, 8 min, 20 min, 1 hour and 2 hours for the EUVI, COR1, COR2, HI-1 and HI-2 respectively.

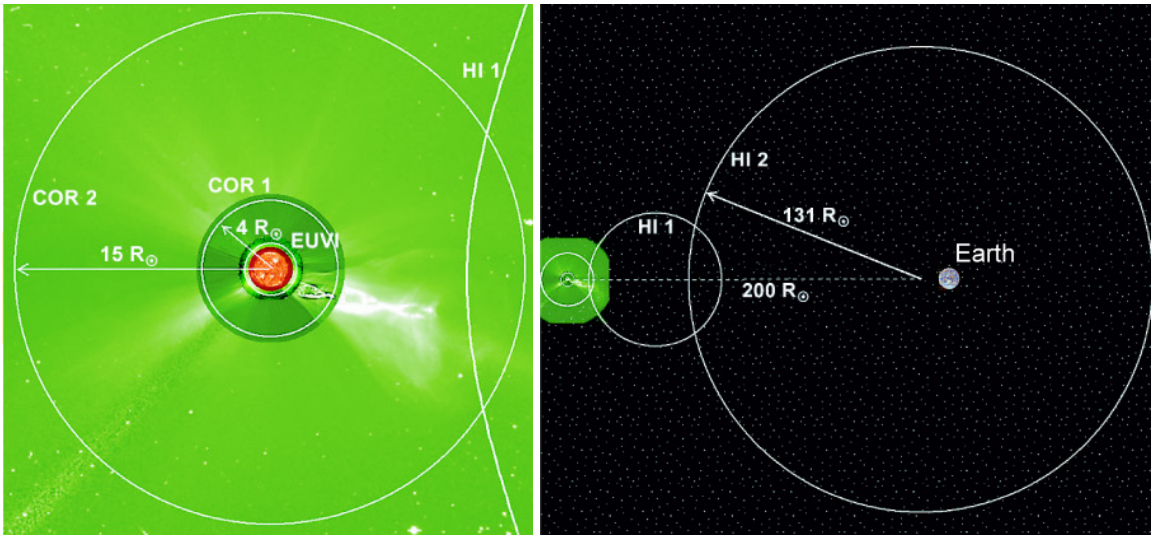

Figure A.4. Fields of view of the instruments constituting the SECCHI package. Left: EUVI, COR1 and COR2 fields of view of the solar corona. Right: spatial coverage of HI-1 and HI-2. Plates courtesy the STEREO consortium.

In all, the SECCHI package promises to provide unprecedented observations, which will help to unveil the 3D structure of coronal features, the origins and 3D structure of CMEs, as well as their interaction with the interplanetary medium. Eventually, a prime goal is the development of space weather forecasts, which will pursue the prediction of geoeffective CMEs and solar energetic particles.

Bibliography

Abbo, L., Antonucci, E., Mikic, Z., Riley, P., Dodero, M. A., Giordano, 2003, Acceleration region of the slow solar wind in corona, Memorie della Societa Astronomica Italiana, 74, 733

Amari, T., Luciani, J. F., Mikic, Z., Linker, J., 2000, A Twisted Flux Rope Model for Coronal Mass Ejections and Two-Ribbon Flares, ApJ, 529, L49–L52

Antiochos, S. K., DeVore, C. R., Klimchuk, J. A., 1999, A Model for Solar Coronal Mass Ejections, ApJ, 510, 485–493

Asai, A., Yokoyama, T., Shimojo, M., Masuda, S., Kurokawa, H., Shibata, K., 2004, Flare Ribbon Expansion and Energy Release Rate, ApJ, 611, 557–567

Aschwanden,M. J., 2004, Physics of the Solar Corona - An Introduction, UK: Springer-Praxis

Benevolenskaya, E. E., Kosovichev, A. G., Lemen, J. R., Scherrer, P. H., Slater, G. L., 2002, Large-Scale Solar Coronal Structures in Soft X-Rays and Their Relationship to the Magnetic Flux, ApJ, 571, L181–L185

Bilenko, I. A., 2002, Coronal holes and the solar polar field reversal, A&A, 396, 657–666

Bird, M. K., Edenhofer, P., 1990, Remote Sensing Observations of the Solar Corona, in Physics of the Inner Heliosphere I, Germany: Springer

Bothmer, V., Schwenn, R., 1995, The interplanetary and solar causes of major magnetic storms, J. Geomag. Geoelectr., 47, 1127

Bothmer, V., Schwenn, R., 1998, The structure and origin of magnetic clouds in the solar wind, Ann. Geophys., 16, 1–24

Bothmer, V., 1999, Solar Corona, SolarWind Structure and Solar Particle Events, in Proc. of ESA Workshop on Space Weather Nov. 1998, ESA WPP-155, ISSN 1022-6656, 117-126, 117–126

Bothmer, V., 2003, Sources of magnetic helicity over the solar cycle, in ESA SP-535: Solar Variability as an Input to the Earth's Environment, 419–428

Brueckner, G. E., Howard, R. A., Koomen, M. J., Korendyke, C. M., Michels, D. J., Moses, J. D., Socker, D. G., Dere, K. P., Lamy, P. L., Llebaria, A., Bout, M. V., Schwenn, R., Simnett, G. M., Bedford, D. K., Eyles, C. J., 1995, The Large Angle Spectroscopic Coronagraph (LASCO), Sol. Phys., 162, 357–402

Burkepile, J. T., St. Cyr, O. C., 1993, A revised and expanded catalogue of mass ejections observed by the Solar Maximum Mission coronagraph, NASA STI/Recon Technical Report N, 93, 26 556

Burkepile, J. T., Hundhausen, A. J., Stanger, A. L., St. Cyr, O. C., Seiden, J. A., 2004, Role of projection effects on solar coronal mass ejection properties: 1. A study of CMEs associated with limb activity, J. Geophys. Res, 3103

Canfield, R. C., Hudson, H. S., McKenzie, D. E., 1999, Sigmoidal morphology and eruptive solar activity, Geophys. Res. Lett, 26, 627–630

Chen, J., 1989, Effects of toroidal forces in current loops embedded in a background plasma, ApJ, 338, 453–470

Chen, J., Howard, R. A., Brueckner, G. E., Santoro, R., Krall, J., Paswaters, S. E., St. Cyr, O. C., Schwenn, R., Lamy, P., Simnett, G. M., 1997, Evidence of an Erupting Magnetic Flux Rope: LASCO Coronal Mass Ejection of 1997 April 13, ApJ, 490, L191

Claridge, G. C., 1937, Coronium, JRASC, 31, 337

Cremades, H., Bothmer, V., 2004, On the three-dimensional configuration of coronal mass ejections, A&A, 422, 307–322

Cremades, H., Bothmer, V., 2005, Geometrical properties of coronal mass ejections, in Proc. IAU Symp. 226 on Coronal and Stellar Mass Ejections, eds. Dere, K. P., Wang, J., and Yan, Y., 48–54

Cremades, H., Bothmer, V., Tripathi, D., 2005, Properties of structured coronal mass ejections in solar cycle 23, Adv. Space Res., in press

Crifo, F., Picat, J. P., Cailloux, M., 1983, Coronal transients - Loop or bubble, Sol. Phys., 83, 143–152

Daglis, I. A., Thorne, R. M., Baumjohann, W., Orsini, S., 1999, The Terrestrial Ring Current: Origin, Formation and Decay, Reviews of Geophysics, AGU, 37, 407–438

Dal Lago, A., Schwenn, R., Gonzalez, W. D., 2003, Relation between the radial speed and the expansion speed of coronal mass ejections, Adv. Space Res., 32, 2637–2640

Delaboudiniere, J.-P., Artzner, G. E., Brunaud, J., Gabriel, A. H., Hochedez, J. F., Millier, F., Song, X. Y., Au, B., Dere, K. P., Howard, R. A., Kreplin, R., Michels, D. J., Moses, J. D., Defise, J. M., Jamar, C., Rochus, P., Chauvineau, J. P., Marioge, J. P., Catura, R. C., Lemen, J. R., Shing, L., Stern, R. A., Gurman, J. B., Neupert,W. M., Maucherat, A., Clette, F., Cugnon, P., van Dessel, E. L., 1995, EIT: Extreme-Ultraviolet Imaging Telescope for the SOHO Mission, Sol. Phys., 162, 291–312

Dere, K. P., Brueckner, G. E., Howard, R. A., Michels, D. J., Delaboudiniere, J. P., 1999, LASCO and EIT Observations of Helical Structure in Coronal Mass Ejections, ApJ, 516, 465–474

Domingo, V., Fleck, B., Poland, A. I., 1995, The SOHO Mission: an Overview, Sol. Phys., 162, 1–37

Dryer, M., 1982, Coronal transient phenomena, Space Sci. Rev., 33, 233–275

Dyer, C., 2002, Radiation effects on spacecraft and aircraft, in ESA SP-477: Solspa 2001, Proceedings of the Second Solar Cycle and SpaceWeather Euroconference, 505–512

Edlén, B., Swings, P., 1942, Term Analysis of the Third Spectrum of Iron (Fe III)., ApJ, 95, 532

Evershed, J., 1909, Radial movement in sun-spots, The Observatory, 32, 291–292

Feynman, J., Hundhausen, A. J., 1994, Coronal mass ejections and major solar flares: The great active center of March 1989, J. Geophys. Res., 99, 8451–8464

Fisher, R. R., Munro, R. H., 1984, Coronal transient geometry. I - The flare-associated event of 1981 March 25, ApJ, 280, 428–439

Fleck, B., Domingo, V., Poland, A., 1995, The SOHO mission, Dordrecht: Kluwer, edited by Fleck, B.; Domingo, V.; Poland, A.

Foukal, P., 1975, The temperature structure and pressure balance of magnetic loops in active regions, Sol. Phys., 43, 327–336

Gibson, S. E., Low, B. C., 1998, A Time-Dependent Three-Dimensional Magnetohydrodynamic Model of the Coronal Mass Ejection, ApJ, 493, 460

Gibson, S. E., Low, B. C., 2000, Three-dimensional and twisted: An MHD interpretation of on-disk observational characteristics of coronal mass ejections, J. Geophys. Res., 105, 18187–18202

Gibson, S. E., Fan, Y., Mandrini, C., Fisher, G., Demoulin, P., 2004, Observational Consequences of a Magnetic Flux Rope Emerging into the Corona, ApJ, 617, 600–613

Golub, L., Krieger, A. S., Silk, J. K., Timothy, A. F., Vaiana, G. S., 1974, Solar X-Ray Bright Points, ApJ, 189, L93

Gonzalez, W. D., Tsurutani, B. T., 1987, Criteria of interplanetary parameters causing intense magnetic storms (D_{st} < -100 nT), Planet. Space Sci., 35, 1101–1109

Gopalswamy, N., Lara, A., Yashiro, S., Nunes, S., Howard, R. A., 2003, Coronal mass ejection activity during solar cycle 23, in ESA SP-535: Solar Variability as an Input to the Earth's Environment, 403–414

Gosling, J. T., Hildner, E., MacQueen, R. M., Munro, R. H., Poland, A. I., Ross, C. L., 1974, Mass ejections from the sun - A view from SKYLAB, J. Geophys. Res., 79, 4581–4587

Gosling, J. T., 1993, The solar flare myth, J. Geophys. Res., 98, 18937–18950

Hale, G. E., Ellerman, F., Nicholson, S. B., Joy, A. H., 1919, The Magnetic Polarity of Sun-Spots, ApJ, 49, 153

Harra, L. K., Mason, K. O., 2004, Space Science, UK: Imperial College Press

Harvey, K. L., Recely, F., 2002, Polar Coronal Holes During Cycles 22 and 23, Sol. Phys., 211, 31–52

Heyvaerts, J., 1974, Coronal electric currents produced by photospheric motions, Sol. Phys., 38, 419–437

Hildner, E., Gosling, J. T., MacQueen, R. M., Munro, R. H., Poland, A. I., Ross, C. L., 1976, Frequency of coronal transients and solar activity, Sol. Phys., 48, 127–135

Howard, R. A., et al., 1997, Observations of CMEs from SOHO/LASCO, 10, in Coronal Mass Ejections, Geophysical Monograph 99

Howard, R. A., Michels, D. J., Sheeley, N. R., Koomen, M. J., 1982, The observation of a coronal transient directed at earth, ApJ, 263, L101–L104

Howard, R. A., Sheeley, N. R., Michels, D. J., Koomen, M. J., 1985, Coronal mass ejections - 1979-1981, J. Geophys. Res., 90, 8173–8191

Howard, R. A., Sheeley, N. R., Michels, D. J., Koomen, M. J., 1986, The solar cycle dependence of coronal mass ejections, in ASSL Vol. 123: The Sun and the Heliosphere in Three Dimensions, 107–111

Hudson, H., Haisch, B., Strong, K. T., 1995, Comment on 'The solar flare myth' by J. T. Gosling, J. Geophys. Res., 100, 3473–3477

Hudson, H. S., Lemen, J. R., St. Cyr, O. C., Sterling, A. C., Webb, D. F., 1998, X-ray coronal changes during halo CMEs, Geophys. Res. Lett., 25, 2481–2484

Hundhausen, A. J., Sawyer, C. B., House, L., Illing, R. M. E., Wagner, W. J., 1984, Coronal mass ejections observed during the solar maximum mission - Latitude distribution and rate of occurrence, J. Geophys. Res., 89, 2639–2646

Hundhausen, A. J., 1993, Sizes and locations of coronal mass ejections - SMM observations from 1980 and 1984-1989, J. Geophys. Res., 98, 13 177

Hundhausen, A. J., Burkepile, J. T., St. Cyr, O. C., 1994, Speeds of coronal mass ejections: SMM observations from 1980 and 1984-1989, J. Geophys. Res., 99, 6543–6552

Hundhausen, A., 1999, Coronal Mass Ejections, in The many faces of the sun: a summary of the results from NASA's Solar Maximum Mission., 143

Illing, R. M. E., Hundhausen, A. J., 1985, Observation of a coronal transient from 1.2 to 6 solar radii, J. Geophys. Res., 90, 275–282

Jones, H. P., Duvall, T. L., Harvey, J. W., Mahaffey, C. T., Schwitters, J. D., Simmons, J. E., 1992, The NASA/NSO spectromagnetograph, Sol. Phys., 139, 211–232

Koomen, M., Howard, R., Hansen, R., Hansen, S., 1974, The Coronal Transient of 16 June 1972, Sol. Phys., 34, 447

Kopp, R. A., Pneuman, G. W., 1976, Magnetic reconnection in the corona and the loop prominence phenomenon, Sol. Phys., 50, 85–98

Koutchmy, S., Livshits, M., 1992, Coronal Streamers, Space Sci. Rev., 61, 393

Lamy, P., et al., 1997, Characterisation of Polar Plumes from LASCO-C2 Images in Early 1996, in ESA SP-404: Fifth SOHO Workshop: The Corona and Solar Wind Near Minimum Activity, 487

Lang, K. R., 2001, The Cambridge Encyclopedia of the Sun, UK: Cambridge University Press

Linker, J. A., Miki´c, Z., Riley, P., Lionello, R., Odstrcil, D., 2003, Models of Coronal Mass Ejections: A Review with A Look to The Future, in AIP Conf. Proc. 679: Solar Wind Ten, 703–710

Low, B. C., 2001, Coronal mass ejections, magnetic flux ropes, and solar magnetism, J. Geophys. Res., 25 141–25 164

Low, B. C., Zhang, M., 2002, The Hydromagnetic Origin of the Two Dynamical Types of Solar Coronal Mass Ejections, ApJ, 564, L53–L56

Lyot, B., 1939, The study of the solar corona and prominences without eclipses (George Darwin Lecture, 1939), MNRAS, 99, 580

MacQueen, R. M., Csoeke-Poeckh, A., Hildner, E., House, L., Reynolds, R., Stanger, A., Tepoel, H., Wagner, W., 1980, The High Altitude Observatory Coronagraph/ Polarimeter on the Solar Maximum Mission, Sol. Phys., 65, 91–107

MacQueen, R. M., Fisher, R. R., 1983, The kinematics of solar inner coronal transients, Sol. Phys., 89, 89–102

MacQueen, R. M., 1993, The three-dimensional structure of 'loop-like' coronal mass ejections, Sol. Phys., 145, 169–188

Malinovsky-Arduini, M., Froehlich, C., 1984, The solar and heliospheric observatory, SOHO - A phase-A project of the European Space Agency, Adv. Space Res., 4, 383– 392

McComas, D. J., Elliott, H. A., Schwadron, N. A., Gosling, J. T., Skoug, R. M., Goldstein, B. E., 2003, The three-dimensional solar wind around solar maximum, Geophys. Res. Lett., 30, 24

McIntosh, P. S., 2003, Patterns and dynamics of solar magnetic fields and HeI coronal holes in cycle 23, in ESA SP-535: Solar Variability as an Input to the Earth's Environment, 807–818

Michalek, G., Gopalswamy, N., Yashiro, S., 2003, A New Method for Estimating Widths, Velocities, and Source Location of Halo Coronal Mass Ejections, ApJ, 584, 472–478

Moran, T. G., Davila, J. M., 2004, Three-Dimensional Polarimetric Imaging of Coronal Mass Ejections, Science, 305, 66–71

Moses, D., Clette, F., Delaboudiniere, J.-P., Artzner, G. E., Bougnet, M., Brunaud, J., Carabetian, C., Gabriel, A. H., Hochedez, J. F, Millier, F., Song, X. Y., Au, B., Dere, K. P., Howard, R. A., Kreplin, R., Michels, D. J., Defise, J. M., Jamar, C., Rochus, P., Chauvineau, J. P., Marioge, J. P., Catura, R. C., Lemen, J. R., Shing, L., Stern, R. A., Gurman, J. B., Neupert, W. M., Newmark, J., Thompson, B., Maucherat, A., Portier-Fozzani, F., Berghmans,

D., Cugnon, P., van Dessel, E. L., Gabryl, J. R., 1997, EIT Observations of the Extreme Ultraviolet Sun, Sol. Phys., 175, 571-599

Munro, R. H., Gosling, J. T., Hildner, E., MacQueen, R. M., Poland, A. I., Ross, C. L., 1979, The association of coronal mass ejection transients with other forms of solar activity, Sol. Phys., 61, 201–215

Parker, E. N., 1958, Dynamics of the Interplanetary Gas and Magnetic Fields, ApJ, 128, 664

Phillips, K. J. H., 1992, Guide to the Sun, UK: Cambridge University Press

Plunkett, S. P., Vourlidas, A., Simberová, S., Karlický, M., Kotrc, P., Heinzel, P., Kupryakov, Y. A., Guo,W. P.,Wu, S. T., 2000, Simultaneous SOHO and Ground-Based Observations of a Large Eruptive Prominence and Coronal Mass Ejection, Sol. Phys., 194, 371–391

Pneuman, G. W., 1969, Coronal Streamers. II: Open Streamer Configurations, Sol. Phys., 6, 255

Pojoga, S., Huang, T. S., 2003, On the sudden disappearances of solar filaments and their relationship with coronal mass ejections, Adv. Space Res., 32, 2641–2646

Reitz, G., 1999, Biological effects of space radiation, in ESA WPP-155: 1998, Proceedings of Workshop on Space Weather

Russell, C. T., McPherron, R. L., 1973, The Magnetotail and Substorms, Space Sci. Rev., 15, 205

Scherrer, P. H., Bogart, R. S., Bush, R. I., Hoeksema, J. T., Kosovichev, A. G., Schou, J., Rosenberg, W., Springer, L., Tarbell, T. D., Title, A., Wolfson, C. J., Zayer, I., MDI Engineering Team, 1995, The Solar Oscillations Investigation - Michelson Doppler Imager, Sol. Phys., 162, 129–188

Schwenn, R., 1986, Relationship of coronal transients to interplanetary shocks 3D aspects, Space Sci. Rev., 44, 139–168

Schwenn, R., 1990, Large-Scale Structure of the Interplanetary Medium, S. 99, in Physics of the Inner Heliosphere I, Germany: Springer

Schwenn, R., 1996, An Essay on Terminology, Myths and Known Facts: Solar Transient - Flare - CME - Driver Gas - Piston - BDE - Magnetic Cloud - Shock Wave – Geomagnetic Storm, Ap&SS, 243, 187

Schwenn, R., 2000, Coupling Between High and Low Latitudes as Observed with Lasco in the Solar Corona and in Interplanetary Space, Adv. Space Res., 26, 771–780

Schwenn, R., Dal Lago, A., Huttunen, E., Gonzalez, W. D., 2005, The association of coronal mass ejections with their effects near the Earth, Ann. Geophys., 23, 1033-1059

Sheeley, N. R., Michels, D. J., Howard, R. A., Koomen, M. J., 1980, Initial observations with the SOLWIND coronagraph, ApJ, 237, L99–L101

Sheeley, N. R., Howard, R. A., Koomen, M. J., Michels, D. J., 1986, SOLWIND observations of coronal mass ejections during 1979-1985, in Solar Flares and Coronal Physics Using P/OF as a Research Tool, 241–256

Sheeley, N. R.,Walters, J. H.,Wang, Y.-M., Howard, R. A., 1999, Continuous tracking of coronal outflows: Two kinds of coronal mass ejections, J. Geophys. Res., 104, 24 739–24 768

Shibata, K., Ishido, Y., Acton, L. W., Strong, K. T., Hirayama, T., Uchida, Y., McAllister, A. H., Matsumoto, R., Tsuneta, S., Shimizu, T., Hara, H., Sakurai, T., Ichimoto, K., Nishino, Y., Ogawara, Y., 1992, Observations of X-ray jets with the YOHKOH Soft X-ray Telescope, PASJ, 44, L173–L179

Srivastava, N., Schwenn, R., Inhester, B., Martin, S. F., Hanaoka, Y., 2000, Factors Related to the Origin of a Gradual Coronal Mass Ejection Associated with an Eruptive Prominence on 1998 June 21-22, ApJ, 534, 468–481

St. Cyr, O. C., Burkepile, J. T., Hundhausen, A. J., Lecinski, A. R., 1999, A comparison of ground-based and spacecraft observations of coronal mass ejections from 1980-1989, J. Geophys. Res., 104, 12493–12506

St. Cyr, O. C., Howard, R. A., Sheeley Jr., N. R., Plunkett, S. P., Michels, D. J., Paswaters, S. E., Koomen, M. J., Simnett, G. M., Thompson, B. J., Gurman, J. B., Schwenn, R., Webb, D. F., Hildner, E., Lamy, P. L., 2000, Properties of Coronal Mass Ejections: SOHO LASCO Observations from January 1996 to June 1998, J. Geophys. Res., 105, 18169-18185

Stenborg, G., Schwenn, R., Srivastava, N., Inhester, B., Podlipnik, B., Rovira, M., Francile, C., 1999, MICA: The Mirror Coronagraph for Argentina, Space Sci. Rev., 87, 307–310

Sterling, A. C., Hudson, H. S., Thompson, B. J., Zarro, D. M., 2000, Yohkoh SXT and SOHO EIT Observations of Sigmoid-to-Arcade Evolution of Structures Associated with Halo Coronal Mass Ejections, ApJ, 532, 628–647

Stix, M., 1989, The Sun – An Introduction, Germany: Springer Verlag

Subramanian, P., Dere, K. P., 2001, Source Regions of Coronal Mass Ejections, ApJ, 561, 372–395

Tandberg-Hanssen, E., Malville, J. M., 1974, Magnetic fields in flares and active prominences. II - The field configuration in some active prominences, Sol. Phys., 39, 107–119

Thompson, B. J., Plunkett, S. P., Gurman, J. B., Newmark, J. S., St. Cyr, O. C., Michels, D. J., 1998, SOHO/EIT observations of an Earth-directed coronal mass ejection on May 12, 1997, Geophys. Res. Lett., 25, 2465-2468

Tousey, R., Koomen, M. J., 1974, Transients Observed Through August During 1972 by the NRL White Light Coronagraph in OSO-7, in Flare-Produced Shock Waves in the Corona and in Interplanetary Space, 89

Treumann, R. A., Baumjohann, W., 1997, Advanced space plasma physics, London: Imperial College Press

Tripathi, D., Bothmer, V., Cremades, H., 2004, The basic characteristics of EUV posteruptive arcades and their role as tracers of coronal mass ejection source regions, A&A, 422, 337–349

Trottet, G., MacQueen, R. M., 1980, The orientation of pre-transient coronal magnetic fields, Sol. Phys., 68, 177–186

Tsurutani, B. T., Smith, E. J., Gonzalez, W. D., Tang, F., Akasofu, S. I., 1988, Origin of interplanetary southward magnetic fields responsible for major magnetic storms near solar maximum (1978-1979), J. Geophys. Res., 93, 8519–8531

Tsurutani, B. T., Lee, Y. T., Gonzalez, W. D., Tang, F., 1992, Great magnetic storms, Geophys. Res. Lett, 19, 73–76

Tsurutani, B. T., Judge, D. L., Guarnieri, F. L., Gangopadhyay, P., Jones, A. R., Nuttall, J., Zambon, G. A., Didkovsky, L., Mannucci, A. J., Iijima, B., Meier, R. R., Immel, T. J., Woods, T. N., Prasad, S., Floyd, L., Huba, J., Solomon, S. C., Straus, P., Viereck, R., 2005, The October 28, 2003 extreme EUV solar flare and resultant extreme ionospheric effects: Comparison to other Halloween events and the Bastille Day event, Geophys. Res. Lett, 32, 3

van Ballegooijen, A. A., Martens, P. C. H., 1989, Formation and eruption of solar prominences, ApJ, 343, 971–984

Vandenbussche, F. C., 1999, SOHOs Recovery: An Unprecedented Success Story, in ESA bulletin 97

Vourlidas, A., Buzasi, D., Howard, R. A., Esfandiari, E., 2002, Mass and energy properties of LASCO CMEs, in ESA SP-506: Solar Variability: From Core to Outer Frontiers, 91–94

Wang, Y., Shen, C., Wang, S., Ye, P., 2004, Deflection of coronal mass ejection in the interplanetary medium, Sol. Phys., 222, 329–343

Wang, Y.-M., Sheeley, N. R., 1989, Average properties of bipolar magnetic regions during sunspot cycle 21, Sol. Phys., 124, 81–100

Wang, Y.-M., 1994, Polar plumes and the solar wind, ApJ, 435, L153–L156

Wang, Y.-M., Sheeley, N. R., Socker, D. G., Howard, R. A., Rich, N. B., 2000, The dynamical nature of coronal streamers, J. Geophys. Res., 25133–25142

Wang, Y.-M., Sheeley, N. R., Andrews, M. D., 2002, Polarity reversal of the solar magnetic field during cycle 23, J. Geophys. Res., 107, DOI 10.1029/2002JA009463

Webb, D. F., Davis, J. M., McIntosh, P. S., 1984, Observations of the reappearance of polar coronal holes and the reversal of the polar magnetic field, Sol. Phys., 92, 109-132

Webb, D. F., Hundhausen, A. J., 1987, Activity associated with the solar origin of coronal mass ejections, Sol. Phys., 108, 383–401

Webb, D. F., 1988, Erupting prominences and the geometry of coronal mass ejections, J. Geophys. Res., 93, 1749–1758

Webb, D. F., Jackson, B. V., 1990, The identification and characteristics of solar mass ejections observed in the heliosphere by the HELIOS 2 photometers, J. Geophys. Res., 95, 20 641–20 661

Webb, D. F., Kahler, S. W., McIntosh, P. S., Klimchuck, J. A., 1997, Large-scale structures and multiple neutral lines associated with coronal mass ejections, J. Geophys. Res., 102, 24161–24174

Webb, D. F., 1998, CMEs and Prominences and Their Evolution over the Solar Cycle (Review), in Astronomical Society of the Pacific Conference Series, 463

Webb, D. F., 2002, CMEs and the solar cycle variation in their geoeffectiveness, in ESA SP-508: From Solar Min to Max: Half a Solar Cycle with SOHO, 409–419

Wilson, P. R., 1965, The Wilson Effect and Sunspot Structure., ApJ, 142, 773 Wolfson, J., Bruner, M., Jurcevich, B., Lemen, J., Schrijver, K., Shine, R., Strong, K., Tarbell, T., Title, A., Golub, L., Bookbinder, J., Deluca, E., Acton, L., Handy, B., Kankelborg, C., Fisher, R., 1997, The TRACE Mission, BAAS, 29, 887

Woch, J., Axford, W. I., Mall, U., Wilken, B., Livi, S.; Geiss, J., Gloeckler, G., Forsyth, R. J., 1997, SWICS/Ulysses observations: The three-dimensional structure of the heliosphere in the declining/minimum phase of the solar cycle, Geophys. Res. Lett., 24, 2885-2888

Wood, B. E., Karovska, M., Chen, J., Brueckner, G. E., Cook, J. W., Howard, R. A., 1999, Comparison of Two Coronal Mass Ejections Observed by EIT and LASCO with a Model of an Erupting Magnetic Flux Rope, ApJ, 512, 484–495

Wu, S. T., 1982, Numerical simulation of magnetohydrodynamic shock propagation in the corona, Space Sci. Rev., 32, 115–129

Yashiro, S., Gopalswamy, N., Michalek, G., Howard, R. A., 2003, Properties of narrow coronal mass ejections observed with LASCO, Adv. Space Res., 32, 2631–2635

Yashiro, S., Gopalswamy, N., Michalek, G., St. Cyr, O. C., Plunkett, S. P., Rich, N. B., Howard, R. A., 2004, A catalog of white light coronal mass ejections observed by the SOHO spacecraft, J. Geophys. Res., 7105

Yurchyshyn, V. B., Wang, H., Goode, P. R., Deng, Y., 2001, Orientation of the Magnetic Fields in Interplanetary Flux Ropes and Solar Filaments, ApJ, 563, 381–388

Zeeman, P., 1897, On the Influence of Magnetism on the Nature of the Light Emitted by a Substance, ApJ, 5, 332

Zhao, X. P., Plunkett, S. P., Liu, W., 2002, Determination of geometrical and kinematical properties of halo coronal mass ejections using the cone model, J. Geophys. Res., 107, 13

Zhukov, A. N., Auchère, F., 2004, On the nature of EIT waves, EUV dimmings and their link to CMEs, A&A, 427, 705–716

Acknowledgements

I am very grateful to everybody who has made this study possible, directly or indirectly.

In the first place I would like to thank my supervisor at MPS, Dr. Volker Bothmer for his guidance and determined assistance over these three years of work. His observations, comments and ideas have greatly helped to achieve my final goal. I have to thank him for giving me the chance to present my work at international conferences and meet the "celebrities" of the scientific community. I am thankful to my supervisor at the Technische Universität Braunschweig, Prof. Dr. Karl-Heinz Glaßmeier, for his assistance and concern regarding the acceptance process at the University. To pass the necessary exams would have been a much tougher task without his and Prof. Dr. Uwe Motschmann's help, who had the patience and skills required to understand our intricate and slow German.

I am grateful to the "International Max-Planck Research School on Physical Processes in the Solar System and Beyond" (IMPRS), for supporting and providing the necessary background, not only educational. Its coordinator, Dr. Dieter Schmitt, deserves special recognition for the devotion and effort with which he organizes the school. I acknowledge the support provided by the German "Bundesministerium für Bildung und Forschung" through the "Deutsche Zentrum für Luft- und Raumfahrt e.V." (DLR) under project number 50 OC 0005. I would like to thank the Max-Plank-Institut für Sonnensystemforschung and its scientific staff, for offering a great research atmosphere.

A special "Dankeschön" goes to Prof. Dr. Rainer Schwenn, who always had time to provide wise and clear answers to my numerous questions. I also don't forget the invitation to the school of solar physics in "El Leoncito", where my passion for this field of research grew stronger. I want to express my gratitude to Prof. Dr. Sami Solanki for valuable discussions and suggestions, although some of them still need efforts from my side. I truly appreciate the disinterested help provided by Dr. Bernd Inhester, Dr. Jaime Araneda, and Rajat Thomas, when I was drowning in a sea of equations. I am grateful to technical and administrative staff of the institute, especially to Andreas Propawa. I also thank Borut Podlipnik for his help in IDL and SolarSoft issues.

The enthusiasm for research and the support obtained from my professors Enrique and Carlos Puliafito have been decisive for my carrier. I want to express my deepest gratitude to them. I am also thankful to Gerd Hartmann, for the many coffees and interesting conversations.

The friends I made at the institute made my stay in Lindau not only possible, but amusing! I thank especially Marilena, Denise, Regina, Ana, Laura and Lupe for their unquestioning friendship, support and encouragement. I am thankful to Guillermo for his suggestions and cheerful spirit, and to Durgesh for both serious and hilarious chats. I don't forget the conversations (mainly in Spanish) with Santo, Geronimo, Juan and Luca. The list has grown so large that I cannot mention everybody: you know I am grateful!

Agradezco a mi familia, a quien dedico esta tesis. Gracias papá por apoyarme siempre en mis decisiones, sabiendo que hacer lo que me gusta implica que yo esté tan lejos. Gracias mamá por

transmitirme tu increíble fortaleza en los momentos más difíciles de estos tres años. Gracias Martín por hacerme morir de la risa cada vez que te conectabas al messenger. A mis amigas del alma: Flavia, Carina y Diana, gracias por apoyarme y comprenderme. Gracias Gaby por tu amistad. Luciano, ser el último te hace el más importante: no sé cómo describir con palabras mi profundo agradecimiento por haberme acompañado y ayudado a crecer en los últimos años.

This work is part of the scientific investigations of the project Stereo/Corona, in context of the International Max Planck Research School, supported by the German "Bundesministerium für Bildung und Forschung" through the "Deutsche Zentrum für Luft- und Raumfahrt e.V." (DLR, German Space Agency) under project number 50 OC 0005. Stereo/Corona is a science and hardware contribution to the optical imaging package SECCHI, currently being developed for the NASA STEREO mission to be launched in 2005. Further information can be found at *http://stp.gsfc.nasa.gov/missions/stereo/stereo.htm*. I thank all the members of the SOHO/LASCO/EIT/MDI consortium who built the instruments and provided the data used in this study. LASCO, EIT and MDI images are courtesy of SOHO consortium. SOHO is a project of international cooperation between ESA and NASA. The CME Catalogue is generated and maintained by NASA and The Catholic University of America in cooperation with the Naval Research Laboratory. I acknowledge the use of Hα data from the Observatory of Meudon and Big Bear Solar Observatory. NSO/Kitt Peak data used here are produced cooperatively by NSF/NO AO, NASA/GSFC and NOAA/SEL.